
Vibration Analysis for Performance Improvement of Structural Sports Equipment

João Miguel Vilaça dos Santos Costa

Dissertation submitted to
Faculdade de Engenharia da Universidade do Porto
for the degree of:

Master's Degree in Mechanical Engineering

Advisor:
João Pereira Amorim

Co-Advisor:
José Dias Rodrigues

Laboratório de Vibrações de Sistemas Mecânicos
Departamento de Engenharia Mecânica
Faculdade de Engenharia da Universidade do Porto

Porto, 2022

The work presented in this dissertation was performed at the
Laboratory of Vibrations of Mechanical Systems
Department of Mechanical Engineering
Faculty of Engineering
University of Porto
Porto, Portugal.

João Miguel Vilaça dos Santos Costa
E-mail: up201704393@up.pt

Faculdade de Engenharia da Universidade do Porto
Departamento de Engenharia Mecânica
Laboratório de Vibrações de Sistemas Mecânicos
Rua Dr. Roberto Frias s/n, Sala M206
4200-465 Porto
Portugal

Abstract

The objective of this thesis was to develop a mountain bike's handlebar that provides more comfort to the cyclist. Furthermore, this solution must have a lower environmental impact. Flax fiber composites are proposed to be part of that handlebar because they would make it more comfortable due to the excellent damping properties of this material and also more eco-friendly using natural fibers. One of the main concerns was if flax fibers alone could handle the static requirements needed for a mountain bike's handlebar. Still, it is also crucial to not forget performance. This means that the handlebar must not be too heavy because it will result in performance losses. This way, an equilibrium between those three parameters is ideal. It is also important to have the cost of the handlebar into consideration.

Therefore, one commercial aluminum handlebar and two commercial carbon fiber composite handlebars were used as a benchmark to have some data to compare with the developed handlebar. Simulations were performed in the commercial software Ansys for a reference aluminum cylinder and an aluminum handlebar. This way, the geometry and model used in the software for the next simulations could be validated. The main material under study was flax fiber composites. Besides, hybrid composite handlebars with carbon and flax fiber composites were tested. In addition, dynamic tests were performed to compare the commercial handlebars and to study their dynamic behavior.

It was concluded that a mountain bike handlebar made only of flax fiber composites was not possible because the static requirements were not accomplished. However, it is possible to develop a city bike handlebar only with flax fiber composites. Besides, it is possible to propose a solution including carbon and flax fiber composites that could handle the necessary static requirements. This solution is heavier than traditional carbon fiber handlebars and has a similar weight compared to the aluminum handlebar. Predictably, vibration damping is better in this handlebar due to the use of flax fibers in the interior plies. Interior plies are the plies that have a major impact on damping, so it is convenient to have flax fiber plies placed there. Beyond that, this handlebar has a lower environmental impact than traditional ones.

Keywords: Handlebars, Composite, Flax Fiber Composite, Carbon Fiber Composite, Comfort, Vibrations, FEM

Resumo

O objetivo desta dissertação é o desenvolvimento de um guiador de bicicleta de montanha que seja mais confortável para o ciclista. Para além disso, esta solução deve também ter um impacto ambiental menor do que os guiadores tradicionais disponíveis no mercado. O material ideal para fazer parte deste guiador são os compósitos reforçados com fibras de linho. Deste modo, o guiador será mais confortável, devido às excelentes propriedades de amortecimento das fibras de linho, mas também mais ecológico, uma vez que se trata de fibras naturais. No entanto, a *performance* não pode ser esquecida e deve ser garantida. Isto significa que o guiador não pode ser muito pesado, pois implicaria perda de *performance*. Deve portanto haver um equilíbrio entre estes 3 importantes parâmetros. O custo do guiador é também um fator importante a ter em conta ao longo do trabalho.

Para isso foi estudado um guiador de alumínio presente no mercado e dois guiadores de compósitos reforçados com fibras de carbono também presentes no mercado para ser possível ter vários dados para comparar durante o desenvolvimento desta nova solução. Depois disso, foram realizadas simulações no *software* comercial *Ansys* de um guiador de alumínio semelhante ao estudado anteriormente bem como um tubo cilíndrico de alumínio. Estas simulações tiveram como objetivo validar a geometria e também o modelo criado no *software*. Posteriormente, foram realizadas simulações com a mesma geometria usando-se os compósitos reforçados com fibras de linho como material do guiador. Também se analisaram simulações com a mesma geometria usando um compósito híbrido constituído por fibras de linho e fibras de carbono. Para além disso, foram realizados ensaios dinâmicos nos guiadores utilizados como comparação e no tubo cilíndrico com diferentes tamanhos, de modo a estudar o comportamento dinâmico de cada geometria.

Chegou-se à conclusão de que é impossível ter um guiador de uma bicicleta de montanha com a geometria proposta utilizando apenas os compósitos reforçados com fibras de linho, uma vez que os requisitos estruturais não são atingidos. No entanto, é possível desenvolver um guiador de bicicleta de passeio com a mesma geometria e dimensões, feito em compósitos reforçados com fibras de linho, uma vez que os requisitos estruturais para um guiador deste tipo são inferiores. Foi possível desenvolver um guiador de bicicleta de montanha feito de compósitos reforçados com fibras de carbono e linho que cumpriu os requisitos estruturais pretendidos. Esta solução é mais pesada que os tradicionais guiadores de fibras de carbono e tem um peso semelhante ao guiador de alumínio. É previsível que este guiador seja mais confortável, uma vez que as fibras de linho foram colocadas nas camadas interiores, visto que são as camadas com maior influência no amortecimento das vibrações. É importante salientar que esta solução tem um menor impacto ambiental do que os outros guiadores.

Palavras-chave: Guiadores, Bicicletas, Compósitos, Compósitos reforçados com fibra de linho, Compósitos reforçados com fibra de carbono, Conforto, Vibrações, FEM

To my family.

‘In order to succeed, your desire for success should be greater than your fear of failure.’

Bill Cosby

Acknowledgements

The present master thesis would not have been possible without the efforts of many people, to whom I am extremely grateful:

- To my advisor João Amorim for all his shared knowledge, for his patience and readiness for any doubt clarification for all these months;
- To Pedro Camacho for all the help and availability;
- To the R&D team of the Swiss company Bcomp for providing information about their flax fiber composites;
- To all my friends for all the experiences and for making these five years much more easy;
- To all my family, especially my parents, my brother, and my grandparents for all the unconditional love, support, and patience that you always had throughout my life.

Contents

Abstract	i
Resumo	iii
Acknowledgements	ix
1 Introduction	1
1.1 Introduction	1
1.2 Handlebars	2
1.3 Bike Frame and Handlebar Materials	4
1.3.1 Steel	4
1.3.2 Titanium	4
1.3.3 Aluminum	5
1.3.4 Carbon Fiber Composites	5
1.3.5 Natural Fiber Composites	6
1.3.6 Comparison Of The Materials Used In Bicycles	6
1.4 Manufacturing Process of an Handlebar	8
1.4.1 Aluminum Handlebar	8
1.4.2 Composite Materials Handlebar	8
1.5 Composite Materials	8
1.5.1 Reinforcement	9
1.5.2 Matrix	9
1.5.3 Thermosets vs Thermoplastics	10
1.5.4 Composites Failure Criteria	11
1.6 Hybrid Composites	14
1.7 Carbon Fibers	15
1.7.1 History of Carbon Fibers	15
1.7.2 Structure and Chemical Composition	15
1.7.3 Characteristics of Carbon Fibers	15
1.8 Flax Fibers	16
1.8.1 History of Flax Fibers	16
1.8.2 Structure and Chemical Composition	17
1.8.3 Flax Fibers Characteristics	19
1.8.4 Damping Capability of Flax Fiber Composites	20
1.9 Motivation	22
1.10 Objectives	23
1.11 Layout	23

2	Background Theory	25
2.1	Lateral Bending Test (ISO 4210-5:2014)	25
2.2	Fatigue Test (ISO 4210-5:2014)	26
2.3	Mechanical Vibrations	26
2.3.1	Free Response of a Single Degree-Of-Freedom System	27
2.3.2	Harmonic Regime and Complex Exponential	29
2.3.3	Frequency Response Function	31
2.3.4	Circular Curve Fitting	33
2.4	Human Comfort in a Bicycle	35
2.4.1	Human Vibration Thresholds	36
2.4.2	Whole Body/Hand Vibration Method	36
2.4.3	Absorbed Power Vibration Method	36
2.5	Experimental Methods in Bicycles	36
2.5.1	Experimental Modal Analysis (EMA)	36
2.5.2	Operational Modal Analysis (OMA)	38
3	Experimental Tests	41
3.1	Stiffness Tests	41
3.1.1	Cylindrical Aluminum Tube	41
3.1.2	Renthal's Handlebar	44
3.1.3	OneUp's Handlebar	49
3.1.4	EC90 Handlebar	55
3.2	Experimental Modal Analysis	60
3.2.1	Experimental Setup	60
3.2.2	Cylindrical Aluminum Tube (400mm)	63
3.2.3	Cylindrical Aluminum Tube (775mm)	68
3.2.4	Renthal's Handlebar	72
3.2.5	OneUp's Handlebar	77
3.2.6	EC90 Handlebar	82
3.2.7	Comparison Between Geometries	87
4	Numerical Results	91
4.1	Numerical Model	91
4.1.1	Introduction	91
4.1.2	Finite Element	92
4.1.3	Mesh Convergence - Static Tests	93
4.1.4	Mesh Convergence - Modal Analysis	97
4.2	Materials	100
4.2.1	Aluminum 7050 T-7651	100
4.2.2	Titanium 3AL-2.5 V	100
4.2.3	Bcomp TDS - Prepreg - ampliTex 150 gsm UD 44% RW - Generic	101
4.2.4	Bcomp TDS - Prepreg - ampliTex 500 gsm twill 4-4 44% RW - Generic	102
4.2.5	XC110 210g 2x2 Twill 3k Prepreg Carbon Fiber	103
4.3	Comparison of the Model with Different Materials	104
4.4	Variable Thickness Model using Aluminum 7050 T-7651	109
4.5	Model Validation	111
4.6	Flax Fibers in FEM	117
4.7	Carbon and Flax Fiber Hybrid Composite Handlebar	120
4.8	Comparison of Results for Experimental Tests and FEM Model	126
4.8.1	Cylindrical Aluminum Tube (400 mm)	126

4.8.2	Cylindrical Aluminum Tube (775 mm)	128
4.8.3	Renthal's Handlebar	132
4.9	Dynamic Tests - FEM	134
4.9.1	Carbon Fiber Composite Handlebar	134
4.9.2	Flax and Carbon Fiber Composite Handlebar	136
4.9.3	Flax Fiber Composite Handlebar	139
5	Conclusion	141
5.1	Conclusions	141
5.2	Future Work	142
	References	143
A	Experimental Equipment List	149
B	XC110 210g 2x2 Twill 3k Prepreg Carbon Fibre - Catalog	151

List of Figures

1.1	Types of handlebars [Engineering Learn, 2022]	2
1.2	Main dimensions of mountain bike's handlebars [Alltricks, 2022]	3
1.3	Types of matrices for composite materials	10
1.4	Failure envelopes from the maximum stress/strain criteria [Li, 2020]	13
1.5	Use percentage of the four failure criteria [Camanho, 2002]	14
1.6	McLaren's Formula 1 car seat made of flax fibers [Bcomp, 2022]	17
1.7	McLaren's Formula 1 car seat made of flax fibers [Bcomp, 2022]	17
1.8	Classification of natural fibers [Petinakis et al., 2013]	18
1.9	Structure of a flax fiber [Güven et al., 2016]	18
2.1	Representation of the Lateral Bending Test of the handlebar [for Standard- ization]	25
2.2	Representation of the Fatigue Test of the handlebar [for Standardization]	26
2.3	Representation of a single degree-of-freedom system [Rodrigues, 2020]	27
2.4	Free response of the undamped system [Rodrigues, 2020]	28
2.5	Free response of the underdamped system [Rodrigues, 2020]	28
2.6	Free response of the critically damped system [Rodrigues, 2020]	28
2.7	Free response of the overdamped system [Rodrigues, 2020]	29
2.8	Free response of the system for different damping ratios [Rodrigues, 2020]	29
2.9	Representation of a single degree-of-freedom system subjected to a harmonic load [Rodrigues, 2020]	30
2.10	Nyquist's Diagram of a mobility function [Rodrigues, 2015]	33
2.11	Nyquist's Diagram of a mobility function using 2 points [Rodrigues, 2015]	34
2.12	Estimation and validation of damping ratios [Rodrigues, 2015]	35
2.13	Setup for SIMO and MIMO analysis [Champoux et al., 2007]	37
2.14	Representation of the impact hammer technique [Türkeş and Neşeli, 2014]	38
3.1	Setup for the stiffness test of the cylindrical tube	42
3.2	Representation of the setup for the stiffness test of the cylindrical tube	43
3.3	Flexural stiffness plot for the cylindrical tube	44
3.4	Setup of the stiffness tests for all handlebars	45
3.5	Renthal's handlebar - Position 1	46
3.6	Renthal's handlebar - Position 2	47
3.7	Renthal's handlebar - Position 3	48
3.8	Flexural stiffness plot for the Renthal's handlebar	49
3.9	OneUp's handlebar - Position 1	51
3.10	OneUp's handlebar - Position 2	52
3.11	OneUp's handlebar - Position 3	53
3.12	Flexural stiffness plot of OneUp's handlebar	54

LIST OF FIGURES

3.13	EC90's handlebar - Position 1	56
3.14	EC90's handlebar - Position 2	57
3.15	EC90's handlebar - Position 3	58
3.16	Flexural stiffness plot of EC90's handlebar	59
3.17	Flexural stiffness plot for all geometries	60
3.18	Impact hammer - DYTRAN Instruments 5800SL	61
3.19	Experimental modal analysis setup	61
3.20	Portable data acquisition system - Bruel and Kjaer, 2827-002	62
3.21	Diagram of the Impact Hammer Technique	62
3.22	Cylindrical Tube (400mm) - Measuring and impact points for the EMA . .	63
3.23	Point and transfer FRFs of the cylindrical tube (400 mm)	64
3.24	Coherence of the point and transfer FRFs of the cylindrical tube (400 mm)	65
3.25	Mode shapes of the cylindrical tube (400 mm)	66
3.26	Time response for the measuring points of the point FRF _{10,10} of the cylindrical tube (400 mm)	67
3.27	Transfer FRF _{7,10} of the cylindrical tube (400 mm)	67
3.28	Coherence of the transfer FRF _{7,10} of the cylindrical tube (400 mm)	68
3.29	Cylindrical Tube (775mm) - Measuring and impact points for the EMA . .	68
3.30	Point and transfer FRFs of the cylindrical tube (775 mm)	69
3.31	Coherence of the point and transfer FRFs of the cylindrical tube (775 mm)	70
3.32	Mode shapes of the cylindrical tube (775 mm)	71
3.33	Time response for the measuring points of the point FRF _{9,9} of the cylindrical tube (775 mm)	72
3.34	Measuring and impact points for the experimental modal analysis	73
3.35	Point and transfer FRFs of Renthal's handlebar	74
3.36	Coherence of the point and transfer FRFs of Renthal's handlebar	75
3.37	Mode shapes of the Renthal's handlebar	76
3.38	Time response for the measuring points of the point FRF _{10,10} of the Renthal's handlebar	77
3.39	Measuring and impact points for the experimental modal analysis	78
3.40	Point and transfer FRFs of OneUp's handlebar	79
3.41	Coherence of the point and transfer FRFs of OneUp's handlebar	80
3.42	Mode shapes of the OneUp's handlebar	81
3.43	Time response for the measuring points of the point FRF _{10,10} of the OneUp's handlebar	82
3.44	Measuring and impact points for the experimental modal analysis	83
3.45	Point and transfer FRFs of EC90's handlebar	84
3.46	Coherence of the point and transfer FRFs of EC90's handlebar	85
3.47	Mode shapes of the EC90's handlebar	86
3.48	Time response for the measuring points of the point FRF _{9,9} of the EC90's handlebar	87
4.1	31.8 mm diameter bar clamp handlebar split geometry - Ansys	91
4.2	Path to follow when choosing the adequate finite element for a given model	92
4.3	Boundary conditions of the model	93
4.4	The point where the stress is computed	94
4.5	The edge where the displacement is computed	94
4.6	Discontinuities in the stress analysis in the 31.8 mm diameter split geometry	95
4.7	Boundary conditions of the problem	112
4.8	First step of solving the problem by Castigliano's theorem	112

4.9	Calculation of the bending moment for the first section	113
4.10	Calculation of the bending moment for the second section	113
4.11	Stiffness plot from real cylinder, FEM model and theoretical cylinder	115
4.12	Plot of stiffness of the Renthall handlebar and the FEM model	116
4.13	Geometry of the 35 mm diameter cylindrical tube	117
4.14	Split geometry of the 35 mm diameter handlebar	118
4.15	The division of the handlebar into four sections	119
4.16	The division of the handlebar into three sections	122
4.17	FEM analysis of the flexural stiffness for the flax and carbon fiber composite handlebar	124
4.18	Flexural stiffness plot for the flax and carbon fiber composite handlebar with a woven carbon fiber in the first ply in FEM analysis	125
4.19	Point FRF _{10,10} of the cylindrical tube (400 mm) and its FEM model	126
4.20	Mode shapes of the cylindrical tube (400 mm) and its FEM model	128
4.21	Point FRF _{9,9} of the cylindrical tube (775 mm) and its FEM model	129
4.22	Mode shapes of the cylindrical tube (775 mm) and in its FEM model . . .	131
4.23	Mode shapes of the cylindrical tube (775 mm) and in its FEM model . . .	132
4.24	Point FRF _{10,10} of the Renthall's handlebar and of its FEM model	132
4.25	Mode shapes of the Renthall's handlebar and its FEM model	134
4.26	Point FRF of the carbon fiber composite handlebar in FEM	135
4.27	Mode shapes obtained in FEM for the carbon fiber composite handlebar . .	136
4.28	Point FRF for the flax and carbon fiber composite handlebar in FEM . . .	137
4.29	Mode shapes obtained in FEM for the flax and carbon fiber composite handlebar	138
4.30	Mode shapes obtained in FEM for the flax fiber composite handlebar	140
B.1	Page 2 of the catalog of the woven carbon fiber used	152

List of Tables

1.1	Comparison between bike frame and handlebar materials	7
1.2	Different types of reinforcements used in composites [Vilhena, 2020].	9
1.3	Different chemical compositions (%) of flax fibers [Rahman, 2021].	19
2.1	Lateral bending test load for different bicycles [for Standardization]	25
2.2	Fatigue test loads for different bicycles [for Standardization]	26
3.1	Displacement recording of the cylindrical aluminum tube	43
3.2	Displacement recording for Renthal's handlebar at different positions	49
3.3	Displacement recording for OneUp's handlebar at different positions	54
3.4	Displacement recording for EC90's handlebar at different positions	59
3.5	Sensitivity of the transducers	62
3.6	Natural frequencies and modal damping ratios of the cylindrical tube (400 mm)	68
3.7	Natural frequencies and modal damping ratios of the cylindrical tube (775 mm)	72
3.8	Natural frequencies and modal damping ratios of the Renthal's handlebar	77
3.9	Natural frequencies and modal damping ratios of the OneUp's handlebar	82
3.10	Natural frequencies and modal damping ratios of the EC90's handlebar	87
3.11	Identified natural frequencies (Hz) of all geometries	88
3.12	Damping ratios (%) for each mode of different geometries	88
4.1	Mesh convergence for the 31.8 mm diameter geometry	94
4.2	Mesh convergence for 31.8 mm diameter split geometry	95
4.3	Mesh convergence for 35 mm diameter geometry	96
4.4	Mesh convergence for 35 mm diameter split geometry	97
4.5	Mesh convergence (modal analysis) for 31.8 mm diameter geometry	98
4.6	Mesh convergence (modal analysis) for 31.8 mm diameter split geometry	99
4.7	Mesh convergence (modal analysis) for 35 mm diameter geometry	99
4.8	Mesh convergence (modal analysis) for 35 mm diameter split geometry	100
4.9	Properties of Aluminum 7050 T-7651 used in the FEM analysis	100
4.10	Properties of Titanium 3AL-2.5 V used in the FEM analysis	101
4.11	Properties of Bcomp TDS - Prepreg - ampliTex 150 gsm UD 44% RW - Generic used in the FEM analysis	101
4.12	Properties of Bcomp TDS - Prepreg - ampliTex 500 gsm twill 4-4 44% RW - Generic used in the FEM analysis	103
4.13	Properties of XC110 210g 2x2 Twill 3k Prepreg Carbon Fibre used in the FEM analysis	104
4.14	Stress and displacement of the different geometries using two materials	105
4.15	Natural frequencies of the 31.8 mm diameter geometries using aluminum	106

LIST OF TABLES

4.16	Natural frequencies of the 35 mm diameter geometries using aluminum . . .	107
4.17	Natural frequencies of the 31.8 mm diameter geometries using titanium . .	108
4.18	Natural frequencies of the 35 mm diameter geometries using titanium . . .	109
4.19	Results of 31.8 mm diameter split geometry for constant thickness	110
4.20	Results of 31.8 mm diameter split geometry for variable thickness	110
4.21	Results of 35 mm diameter split geometry for variable thickness	111
4.22	Displacements of the 35 mm cylindrical aluminum tube for different loads .	114
4.23	Displacements of the Renthal's handlebar	116
4.24	Results for a cylindrical tube with a 35 mm diameter made of flax fibers . .	118
4.25	Results of a 35 mm diameter handlebar made of flax fibers and with the same number of plies all over the handlebar	119
4.26	Results of a 35 mm diameter handlebar made of flax fibers and with different number of plies	119
4.27	Results for a 35 mm diameter handlebar made of flax fibers and with dif- ferent number of plies for a city bike	120
4.28	Results of the handlebar with woven carbon fiber composite	121
4.29	Results of the handlebar with woven carbon and flax fiber composites . . .	121
4.30	Results of the handlebar with woven carbon and flax fiber composites - increasing use of flax UD's	122
4.31	Results of the handlebar with woven carbon and flax fiber composites . . .	122
4.32	Results of the best solution for the handlebar with carbon and flax fiber composites	123
4.33	Flexural stiffness test in FEM for the flax and carbon fiber composite han- dlebar	123
4.34	Results of the best solution for the handlebar with of carbon and flax fiber with a woven carbon ply at the top	124
4.35	Flexural stiffness test in FEM for the flax and carbon fiber handlebar with woven carbon fiber in the first ply	125
4.36	Natural frequencies (Hz) of the cylindrical tube (400 mm) and its FEM model	127
4.37	Relative difference between the natural frequencies of the cylindrical tube (400 mm and FEM model	127
4.38	Natural frequencies (Hz) of the cylindrical tube (775 mm) and its FEM model	129
4.39	Relative difference between natural frequencies of cylindrical tube (775 mm) and its FEM model	130
4.40	Natural frequencies (Hz) of the Renthal's handlebar and the FEM model .	133
4.41	Relative difference between natural frequencies of Renthal's handlebar and FEM model	133
4.42	Natural frequencies (Hz) obtained in Ansys for the carbon fiber composite handlebar and obtained experimentally for the OneUp's handlebar	135
4.43	Natural frequencies (Hz) obtained in Ansys for a flax and carbon composite fiber handlebar	137
4.44	Natural frequencies (Hz) obtained in Ansys for a flax fiber composite han- dlebar	139

Introduction

1.1 Introduction

In the last years, bicycle design has evolved significantly. The main focus of bicycle manufacturers has been maximizing the stiffness-to-weight ratio of bicycles, so it is crucial to have an equilibrium between stiffness and weight of the bike. It is important to have a bicycle with low weight because this results in performance gains, being the cyclist faster. However, the bicycle must also be stiff enough to handle all the loads and stresses to which it is submitted. The introduction of carbon fiber composites in bicycles was a crucial step in maximizing the stiffness-to-weight ratio because the bikes are light but also very stiff, improving the performance.

Another aspect that is becoming more important is the rider's comfort. The rider's comfort is a broad concept once is determined by a combination of physical and psychological factors. Pineau [1982] defines comfort as a state of well-being under optimal conditions. Slater [1985] defines comfort as a state of harmony between humans and the environment in three dimensions: "physiological, psychological and physical". Pineau [1982] also referred that comfort differs from person to person depending on the situation. Therefore, the rider's comfort depends on multiple factors like weather conditions, temperature, clothes, fitness level, duration of the ride, the distance of the ride, vibrations felt by the rider, road surface, and many others. According to Dorey and Guastavino [2011], another important factor is the rider's motivation. Therefore, if a cyclist is interested in speed and performance, his need for comfort will be lower.

As can be seen, comfort is a broad concept, but as engineers is important to quantify the rider's comfort and increase it without compromising performance and cost. There are two types of comfort in a bicycle: static and dynamic comfort. The static comfort is related to the rider's position on his bicycle. The dynamic comfort is related to the vibrations felt in the contact points between the rider and the bicycle. The three most important components of the bike at this level are the handlebar, the saddle, and the pedals because those are the ones that have direct contact with the human body. The higher the vibration amplitude, the lower the comfort because vibrations cause fatigue in the rider. Therefore, it is important to decrease the vibrations felt by the rider. The main goal of this work is to study the dynamic comfort of the rider in the specific case of the handlebar. A possible way to have lower vibration amplitudes is to improve the damping of the handlebar, and the study of new materials with improved damping characteristics was essential. Using natural and carbon fiber composites in the handlebar could be an appropriate solution. This composite material is a hybrid fiber composite. A hybrid fiber composite is used when the designer wants to take the main advantages of each material.

In this case of a hybrid fiber composite (natural and carbon fiber), the designer wants to take advantage of the lightweight and high stiffness of the carbon fiber but also wants to take advantage of the damping capacity of the natural fibers. This way, it will be possible to have a handlebar with low weight, high stiffness, and much better damping properties that lead to fewer vibrations felt by the rider and consequently higher comfort. According to the literature, one of the best natural fibers to achieve this goal is flax fiber due to its good damping properties and reliable performance in terms of stiffness and strength. Besides, as a natural fiber, flax has a low environmental impact. Nowadays, the idea of sustainability is growing, so it is always important to have this in sight. To summarize, in this work, it will be necessary to have an equilibrium between performance, comfort, and sustainability to build the best possible handlebar considering all these requirements.

1.2 Handlebars

The handlebar of a bicycle is the component responsible for the steering. It is also responsible for supporting some of the weight of the rider. The handlebar has two handgrips where the rider puts both hands to control the steering. Besides, it provides a mounting place for controls such as brake, horns, or light switches if needed. The handlebar is one of the most critical components of a bicycle in terms of vibration once it is one of the three components that contact the human body of the rider (handlebar, saddle, and pedals). This means that handlebars are very important for comfort due to the fact that lower the amplitude of vibrations more comfort for the rider. There are many types of handlebars for different types of bikes. Figure 1.1 shows some types of handlebars.



Figure 1.1: Types of handlebars [Engineering Learn, 2022]

For mountain bikes, the most common handlebars are the flat and riser handlebars. Mountain bike's handlebars have some important dimensions that can vary or not. In Figure 1.2, it is possible to see the main dimensions of a mountain bike's handlebar.

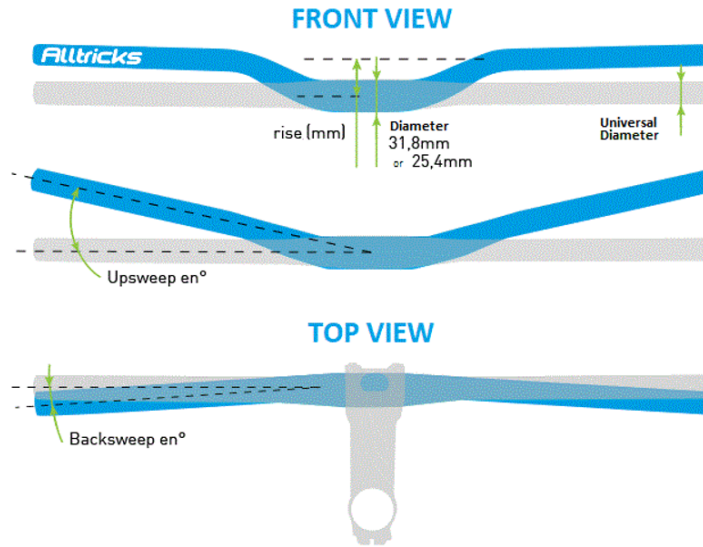


Figure 1.2: Main dimensions of mountain bike's handlebars [Alltricks, 2022]

The rise is the length from the center of the tubular section in the clamp zone to the center of the tubular section on both ends of the handlebar. Nowadays, the rise on mountain bike handlebars varies between 0 mm and 40 mm. A bicycle with a smaller rise is a flat handlebar, and a bicycle with a higher rise is a riser handlebar. The difference between these two types of handlebars is that riser handlebars are for downhill bikes or other types of bicycles that are made more for descents (gravity-oriented setups). The reason is that with a higher rise, the rider has more control over the bicycle because his head and torso are in a higher position. Due to safety issues and performance, more control over the bike in descent is crucial.

Other worth mentioning dimensions of the handlebars are the backsweep and the upsweep. These dimensions are angles, as can be seen in Figure 1.2. Usually, these angles vary between 4° and 6° for upsweep and 7° and 9° for backsweep. Both dimensions are crucial for the comfort of the rider. For example, a rider with longer arms will use a handlebar with a lower backsweep than a rider with smaller arms. Nowadays, the standard diameter of the bar clamp for mountain bikes can have only two values, 31.8 mm and 35 mm. A higher diameter will make the handlebar stiffer. The diameter of both ends of the handlebar is universal - 22.2 mm. The other dimension of the handlebar is the width. The width can vary because of two aspects, the rider's comfort and the stiffness of the handlebar. A handlebar with a higher width will be less stiff and more flexible than a handlebar with a smaller width using the same material. Usually, handlebars with a smaller diameter on the stem region can have also a smaller width to avoid the stiffness being too low. Handlebars with a higher width are easier to steer because of the higher moment and also helps the rider to breathe better on climbs. Usually, the handlebar's width varies between 740-800 mm. The values presented here were obtained after a market analysis of the most known bike companies like Focus, Scott, Santa Cruz, Specialized and many more.

1.3 Bike Frame and Handlebar Materials

In the past, steel dominated in terms of materials used in a bike's frame and handlebar [Norman, 2022]. Nowadays, the most common materials are carbon fiber composites or aluminum, although steel and titanium are still used. Each material has its pros and cons, depending on the priorities of the rider, namely weight, budget, longevity, and performance. It is also important to have the same quality standard in every single part of the bike because it doesn't make sense to spend a lot of money on a carbon fiber composite frame/handlebar and have cheap components in the remaining parts of the bike. Therefore, if someone wants a carbon fiber composite frame/handlebar, it will spend a lot of money on the frame/handlebar, but also on the other components of the bike so those components can be as good as the remaining components of top aluminum bicycles.

1.3.1 Steel

As mentioned before, steel was the first material used to build the frame and handlebar of bicycles. Until the mid-1990s, steel was used even at a professional level. Steel has some pros and cons that will be discussed now.

Advantages of Steel:

- Strong, durable and has high fatigue resistance [Whe, 2022; Norman, 2022];
- Easy to repair [Whe, 2022; Norman, 2022];
- Comfortable ride [Whe, 2022; Norman, 2022];
- More affordable than titanium and carbon fiber [Whe, 2022; Norman, 2022].

Disadvantages of Steel:

- Heavy [Whe, 2022; Norman, 2022];
- More expensive than aluminum because is hand made and require more time [Whe, 2022; Norman, 2022].

1.3.2 Titanium

Titanium is a material that is not as common and is often seen as a luxury option due to its ride quality and cost. Titanium bikes are known as “bikes for life”. Titanium is much more resilient than other metals. Therefore good designers can make lighter bikes without risk of failure.

Advantages of Titanium:

- Strong, durable and has high fatigue resistance [Norman, 2022];
- Lighter than steel [Norman, 2022];
- Excellent ride quality [Norman, 2022];
- Raw finish looks great. Can also be painted [Norman, 2022].

Disadvantages of Titanium:

- Hard to work with. Only good manufacturers can make these bikes;
- Not as light as carbon fiber composites or aluminum;
- Expensive.

1.3.3 Aluminum

Aluminum is the most common material in bicycles nowadays. In the past, one of the main reasons for starting to use aluminum in bikes was that aluminum has a lower density than steel and a higher stiffness-to-weight ratio. Therefore is possible to have a lighter bike with high stiffness.

Advantages of Aluminum:

- High stiffness-to-weight ratio [Norman, 2022], [Whe, 2022];
- Affordable [Norman, 2022], [Whe, 2022];
- More durable than carbon and also its failure is predictable and smooth [Norman, 2022], [Whe, 2022];
- Better to mass manufacture [Norman, 2022], [Whe, 2022];
- Look more modern than steel [Whe, 2022].

Disadvantages of Aluminum:

- High stiffness of the structure can result in a harsh ride quality due to lack of damping shocks or vibrations. This stiffness is not from the material but the stiffness of the structure [Norman, 2022], [Whe, 2022];
- Aluminum fatigues more over time than other materials [Norman, 2022], [Whe, 2022];
- Difficult to repair [Norman, 2022], [Whe, 2022];
- May be more dangerous due to catastrophic failure without warning [Whe, 2022].

As mentioned before, nowadays, aluminum is the most used material in bicycle frames and handlebars. Of all these pros, the most important is the high stiffness-to-weight ratio and the fact that it is cheaper than the other materials. So aluminum is the best material when the cyclist wants a low-weight and high-stiffness bike at a low cost.

1.3.4 Carbon Fiber Composites

Carbon fiber composites started to emerge in the last decades. The fact that carbon fiber composites have a higher stiffness-to-weight ratio than all the other materials makes carbon fiber bikes lighter and with the same or more stiffness than the other bikes. At a professional level, it is the most used material right now. Nevertheless, it is not so common in bikes of regular riders due to the high cost of this material.

Advantages of Carbon Fiber Composites:

- Higher stiffness-to-weight ratio than the other materials [Norman, 2022];
- Highly adaptable [Norman, 2022];
- Can be molded into aerodynamic tube shapes [Norman, 2022].

Disadvantages of Carbon Fiber Composites:

- Very expensive [Norman, 2022];
- Prone to wear and crash damage [Norman, 2022].

1.3.5 Natural Fiber Composites

Nowadays, the idea of sustainability is growing more and more. Therefore, bike designers have started to consider this, and natural fibers have become more popular.

Advantages of Natural Fiber Composites:

- High vibration damping capability results in more comfort to the user;
- Low environmental impact.

Disadvantages of Natural Fiber Composites:

- Natural fibers may not be able to be used alone as they may not meet the necessary structural requirements. Also, their stiffness is not as great as the other materials.

1.3.6 Comparison Of The Materials Used In Bicycles

After discussing the pros and cons of each material, it is important to compare the materials with each other. For that, we can see some properties of these materials summarized in Table 1.1 that were obtained in software CES Edupack.

Table 1.1: Comparison between bike frame and handlebar materials

Property	Steel	Titanium	Aluminum	Carbon Fiber
Density(kg/m ³)	7800	4420 - 4430	2810 - 2840	1550 - 1580
Young's Modulus (GPa)	201 - 216	111 - 119	71 - 74.6	49.7 - 60.1
Yield Strength (MPa)	1240 - 1520	1020 - 1080	393 - 462	603 - 728
Fatigue Strength at 10 ⁷ cycles (MPa)	526 - 608	613 - 638	130 - 150	137 - 231
Fracture Toughness (MPa.m ^{0.5})	30 - 55	82 - 100	23.1 - 42.9	12.1 - 19.8
Specific Stiffness (MN.m/kg)	25.6 - 27.5	25.1 - 26.9	25.1 - 26.5	31.7 - 38.4
Price(EUR/kg) from April, 2022	0.67 - 0.752	20.1 - 22.3	3.4 - 3.83	31.9 - 35.4

As previously mentioned, a carbon fiber composite is the lighter material, and steel is the heaviest. Aluminum has a low density compared with titanium and steel. It is important to point out that this is one of the most important characteristics because the lighter the bike, the better the user's performance. In terms of strength, steel and titanium are the strongest materials. This, along with a high fatigue strength, results in stronger and more durable bicycles that don't fatigue over time. Regarding impact toughness, steel and titanium are also the best materials. Due to all these characteristics, titanium bicycles are known as "bikes for life". In terms of stiffness, as mentioned before, a carbon fiber composite has better specific stiffness. In some specialized magazines on this matter, it is referred that aluminum frames in the past had a harsh ride quality due to stiffness [Norman, 2022]. Probably, they want to mention the stiffness of the structure of the frame and not the stiffness of the material because the specific stiffness of aluminum, steel, and titanium are very similar nowadays. This makes even more sense when some publications refer that new building techniques of frames and handlebars allowed aluminum bicycles to improve their ride quality. In terms of price, it is also known that a carbon fiber composite is the more expensive material of all. This cost in handlebars and frames can be higher because, most of the time, they are handmade. Titanium is also very expensive and sometimes can be more expensive than carbon fiber composites. Steel (raw material) is cheaper than aluminum, as can be seen in the Table 1.1. Although when making the frame and the handlebar, steel requires more time to produce because steel bikes are handmade, resulting in more expensive bikes.

However, analyzing all the materials, excluding the natural fibers, aluminum is probably the best material to choose if the rider wants an equilibrium between performance, low cost, and comfort. If the rider is an enthusiast and is willing to spend more money to have a better performance, carbon fiber composites will probably be the best material. It is also important to realize that an aluminum bike and a carbon fiber bike with the same price means that the other components of the aluminum bike have high quality, and the ones in the carbon fiber bike are not as good. So to have a good carbon fiber bike, much more money is needed. It is due to this that aluminum and carbon fiber composites have been the two most used materials for bicycle frames and handlebars.

1.4 Manufacturing Process of an Handlebar

1.4.1 Aluminum Handlebar

The process starts with an aluminum cylinder tube with a certain thickness. The diameter of this tube is 31.8 mm or 35 mm, depending on the diameter of the clamp region. First, the tube is subjected to an annealing process, spending 6 to 7 hours in the oven at temperatures above 400°C. This process softens the piece to allow further budding and shaping processes. This annealing process is repeated after every budding or shaping process. Before starting the budding and shaping process, the wall thickness and hardness of the cylinder are inspected for quality control. Budding creates varying wall thicknesses throughout the handlebar's length using mandrels. This is important to strengthen specific handlebar areas and to improve the stiffness-weight ratio. The number of times this process is repeated is also the number of thickness variations that the handlebar has throughout its length. These variations in wall thickness must be long and gradual because, if not, there will be a stress concentration in those zones. At this stage, the handlebar's geometry takes shape, although it is just a flat bar for now. After, it must be bent to correct backsweep and upsweep angles. This bending process of the handlebar can be done manually using different fixtures and mandrels. However, it can also be performed using a 3D CNC bending machine to bend the handlebar to its final shape. Thus, the number of errors in tolerances is much lower than if the process is handmade. After that, the handlebars pass for tests and measurements to see if they are as expected to be [Pinkbike, 2022]. After that the finishing processes are done.

1.4.2 Composite Materials Handlebar

The process of producing a composite material handlebar is quite different from aluminum ones. In this case, a metallic mold is needed. The composite plies are laminated in the molds, usually by hand, and pressed into their correct position. Once both molds are laminated, they are brought together with a silicone bladder in between. After that, the mold goes to an induction heat press. In the induction heat press the mold is in an vacuum environment. It is very important to control the vacuum pressure. In this machine, the silicone bladder is inflated with air, and the bar mold stays there for 1/2 hours or more at about 125°C (carbon fiber handlebar). The resin, usually an epoxy, cures during this process. Now the handlebar is ready for finishing processes and graphic applications [Hopetech, 2022]. Just as in the aluminum handlebars, it is also important to check dimensions and other measurements for quality control.

1.5 Composite Materials

A composite is defined as non-homogenous material which is composed of at least two different materials [Vilhena, 2020], [Torres, 2016], [Vanvalleghem, 2009], [Gautam, 2001]. Usually, it consists of a reinforcement material such as fibers or particles supported by a matrix. As the name suggests, the reinforcement material is responsible for reinforcing the composite due to its higher stiffness and strength. The matrix has the function of ensuring efficient transmission and distribution of the stresses applied for the reinforcement. If the bonding between the reinforcement and the matrix is good, the stiffness and strength of the material will benefit due to the better distribution of stresses. However, bonding can also affect the damping properties, as will be discussed. The goal of combining the two materials is to improve performance [Gautam, 2001] or at least reach a similar performance,

reducing the costs or the environmental impact of the product in nature. Nevertheless, the introduction of a composite is always to improve something.

1.5.1 Reinforcement

The reinforcements can be of very different types. Table 1.2 shows the different types of reinforcements used in composites.

Table 1.2: Different types of reinforcements used in composites [Vilhena, 2020].

Reinforcement	Description	Type
Particle	Almost all dimensions are the same	Discontinuous
Whisker	Aspect ratios between 20 to 100	Discontinuous
Short fiber	The length is much higher than their cross-sectional dimensions	Discontinuous
Continuous fiber	The lengths of the continuous fibers are greater than their cross-sectional dimensions	Continuous
Woven	Interlocking fibers that have orientations slightly or fully in an orientation orthogonal to the primary structural plane	Continuous

The most used fibers in composites are carbon fibers, glass fibers, aramid fibers known by the tradename Kevlar, and natural fibers like hemp or flax. As mentioned before, the reinforcement is the part of the composite responsible for the stiffness and strength.

1.5.2 Matrix

There are three types of matrices: metal matrix, ceramic matrix, and organic matrix. The organic matrices can be divided into polymer matrices and carbon matrices. In this study, the type of matrix that will be used is the polymer matrix. Polymers can be divided into thermosets or thermoplastic [Torres, 2016; Vilhena, 2020]. The differences between those two matrices will be discussed in the next section. In Figure 1.3, it is possible to see all types of matrices that are usually used in composites.

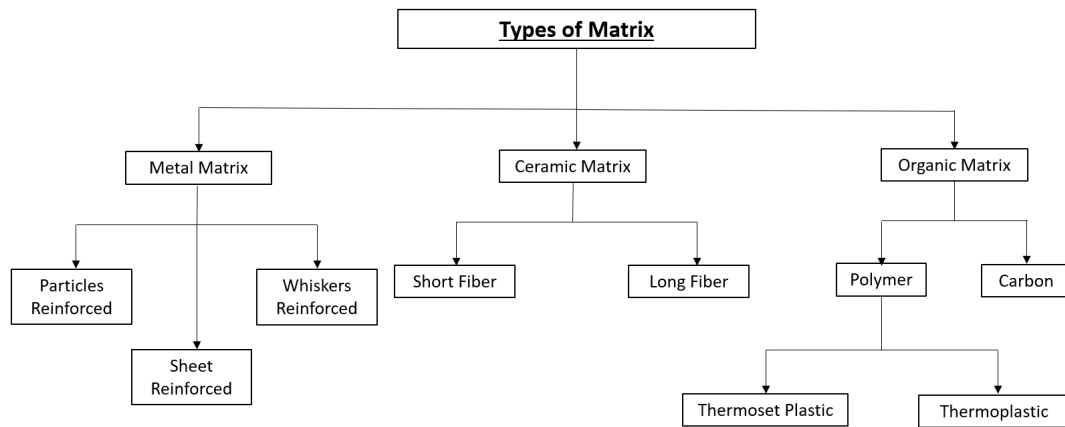


Figure 1.3: Types of matrices for composite materials

1.5.3 Thermosets vs Thermoplastics

As mentioned before, there are three types of matrices. This section will focus on the discussion of an organic matrix, the polymer matrix. Polymer matrices can be divided into two types of polymers: thermosets and thermoplastics. The principal difference between these two types of polymers is that thermoset set their physical and chemical properties after initial heat treatment and are no longer affected by additional heat exposure. This is ideal for applications requiring tight tolerances and an excellent strength-to-weight ratio while being exposed to high temperatures.

Advantages of Thermosets:

- High strength-to-weight ratio and high performance;
- Resistance to corrosion effects and water;
- Lower tooling/set-up costs;
- Reduced production costs over fabrication using metals;
- Their properties are not affected by high temperatures.

Disadvantages of Thermosets:

- Cannot be recycled;
- The stiffness of the material can result in product failure in high vibration applications;
- Cannot be remolded or reshaped.

Nowadays, flax fiber composites are used predominantly with an epoxy matrix [Duc et al., 2014]. Epoxy is a thermoset. Nevertheless, as environmental impact is becoming increasingly more important in the development of new materials, thermoplastic matrices are also becoming more common because thermoplastics are more environmentally friendly than thermosets. The fact that thermoplastics can be recycled justifies the lower environmental impact.

Advantages of Thermoplastics:

- High recyclable;
- Can be remolded and reshaped;
- Excellent corrosion resistance;
- Flexibility and elongation of the coating film;
- Superb impact resistance;
- Slip enhancement. This can cause a major friction between the fibers and matrix resulting in better damping on thermoplastics.

Disadvantages of Thermoplastics:

- May soften when reheated;
- Lower adhesion that can result in lower stiffness;
- More expensive than thermoset plastics.

As mentioned before, thermoplastics can have better damping capacities than thermosets [Duc et al., 2014]. Nowadays, thermoplastics are increasingly being used due to the better damping and lower environmental impact. Of all thermoplastics, polypropylene is the most used for matrices with natural fibers [Duc et al., 2014]. Recently, polylactide has also become more used with various natural fibers. According to [Duc et al., 2014] a composite with polypropylene matrix and flax fiber has a lower stiffness and a lower tensile strength than a composite with polylactide. Duc et al. [2014] also reported that polylactide matrix and flax fiber as reinforcement had the best compromise between stiffness/strength and damping vibration capacity compared with glass fibers/epoxy composite, carbon fibers/epoxy composite, flax fibers/epoxy composite, and flax fibers/polypropylene composite. In addition, as already discussed, thermoplastics have a lower environmental impact than thermoset plastics, which can be nowadays a crucial characteristic even if it means spending a little more money. This may indicate that a thermoplastic can be used in the handlebar as a matrix because it can achieve the best trade-off for the handlebar in terms of damping, stiffness/strength, and sustainability. A good example of that is the Yeti 160E bike, which has a handlebar of 35 mm diameter bar clamp and 800 mm of length made of carbon fibers with a thermoplastic [Bike, 2022]. The environmental impact of this handlebar is lower than the traditional carbon fiber bikes that use epoxy as resin.

1.5.4 Composites Failure Criteria

In this section, the composite failure criteria used in this work in the numeric simulations are presented. There are more criteria for composites failure, although only the ones used will be discussed.

Maximum Stress Criterium

Let us consider a transversely isotropic material where the principal axes are 1, 2, and 3. Axis 1 is usually the one that is along the fiber's direction. Axis 2 and 3 are perpendicular to Axis 1 and perpendicular to each other. Usually, when the material is used in a planar form, Axis 2 is chosen as the one in the plane. Assuming that the stress state is expressed by $[\sigma_1, \sigma_2, \sigma_3, \tau_{23}, \tau_{13}, \tau_{12}]$, tensile and compressive stress along the direction of the fibers as σ_{Lt} and σ_{Lc} , tensile and compressive stress in the transverse direction of fibers direction as σ_{Tt} and σ_{Tc} and shear strengths along the fiber direction and in the transverse direction τ_L and τ_T , respectively, the maximum stress criterium can be expressed by the following equations.

$$\frac{\sigma_1}{\sigma_{Lt}} \leq 1 \text{ if } \sigma_1 \geq 0 \text{ or } \frac{|\sigma_1|}{\sigma_{Lc}} \leq 1 \text{ if } \sigma_1 < 0 \quad (1.1)$$

$$\frac{\sigma_2}{\sigma_{Tt}} \leq 1 \text{ if } \sigma_2 \geq 0 \text{ or } \frac{|\sigma_2|}{\sigma_{Tc}} \leq 1 \text{ if } \sigma_2 < 0 \quad (1.2)$$

$$\frac{\sigma_3}{\sigma_{Tt}} \leq 1 \text{ if } \sigma_3 \geq 0 \text{ or } \frac{|\sigma_3|}{\sigma_{Tc}} \leq 1 \text{ if } \sigma_3 < 0 \quad (1.3)$$

$$\frac{|\tau_{23}|}{\tau_T} \leq 1 \quad (1.4)$$

$$\frac{|\tau_{13}|}{\tau_L} \leq 1 \quad (1.5)$$

$$\frac{|\tau_{12}|}{\tau_L} \leq 1 \quad (1.6)$$

If some of these stress ratios exceed 1, failure is predicted [Li, 2020].

Maximum Strain Criterium

The previous criterium was related to the stresses that the composite is submitted. This one is related to the material strain. Assuming the strain state in the material's principal axes as $[\varepsilon_1, \varepsilon_2, \varepsilon_3, \gamma_{23}, \gamma_{13}, \gamma_{12}]$, tensile and compressive strains along the direction of the fibers as ε_{Lt} and ε_{Lc} , tensile and compressive strains in the transverse direction of fibers direction as ε_{Tt} and ε_{Tc} and shear failure strains along the fiber direction and in the transverse direction as γ_L and γ_T , respectively, the maximum strain criterium can be expressed by the following equations.

$$\frac{\varepsilon_1}{\varepsilon_{Lt}} \leq 1 \text{ if } \varepsilon_1 \geq 0 \text{ or } \frac{|\varepsilon_1|}{\varepsilon_{Lc}} \leq 1 \text{ if } \varepsilon_1 < 0 \quad (1.7)$$

$$\frac{\varepsilon_2}{\varepsilon_{Tt}} \leq 1 \text{ if } \varepsilon_2 \geq 0 \text{ or } \frac{|\varepsilon_2|}{\varepsilon_{Tc}} \leq 1 \text{ if } \varepsilon_2 < 0 \quad (1.8)$$

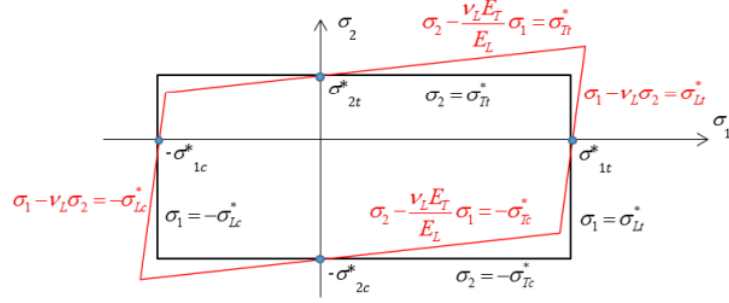
$$\frac{\varepsilon_3}{\varepsilon_{Tt}} \leq 1 \text{ if } \varepsilon_3 \geq 0 \text{ or } \frac{|\varepsilon_3|}{\varepsilon_{Tc}} \leq 1 \text{ if } \varepsilon_3 < 0 \quad (1.9)$$

$$\frac{|\gamma_{23}|}{\gamma_T} \leq 1 \quad (1.10)$$

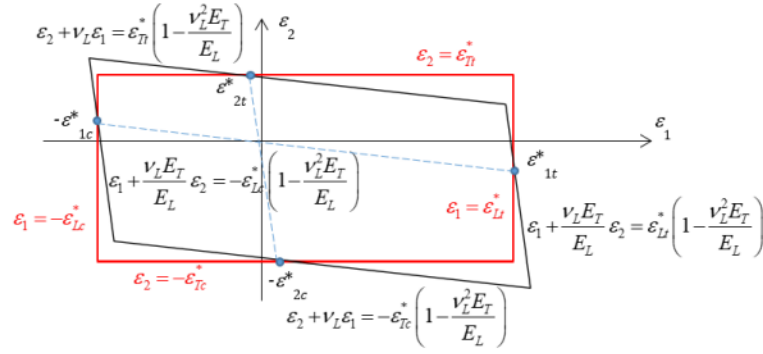
$$\frac{|\gamma_{13}|}{\gamma_L} \leq 1 \quad (1.11)$$

$$\frac{|\gamma_{12}|}{\gamma_L} \leq 1 \quad (1.12)$$

As in the maximum stress criterion, if any of the strain ratios exceed 1, the failure will occur [Li, 2020]. Figure 1.4 shows the failure envelopes of both criteria for the stress and strain plane.



(a) Stress plane



(b) Strain plane

Figure 1.4: Failure envelopes from the maximum stress/strain criteria [Li, 2020]

As can be seen in Figure 1.4, one criterion is more conservative than the other in some regions. So depending on the case, the more or less conservative criterion of both can change. These two criteria are very popular due to their simplicity and are used by designers where a rough but quick estimate has to be made [Li, 2020].

Tsai-Hill Criterion

The Tsai-Hill criterion is also widely used to study the failure in composites. Assuming the stress in each layer as σ_x , σ_y and τ_{xy} and also the ultimate strength of the material as σ_{xr} , σ_{yr} and τ_{xyr} , the Tsai-Hill criterion can be expressed by the following equation.

$$\alpha^2 = \left(\frac{\sigma_x}{\sigma_{xr}} \right)^2 + \left(\frac{\sigma_y}{\sigma_{yr}} \right)^2 - \frac{\sigma_x \sigma_y}{\sigma_{xr}^2} + \left(\frac{\tau_{xy}}{\tau_{xyr}} \right)^2 \quad (1.13)$$

The failure doesn't occur if $\alpha < 1$.

Tsai-Wu Criterium

Assuming a biaxial tensile stress state, $\sigma_{11} = \sigma$, $\sigma_{22} = \alpha\sigma$ and $\sigma_{12} = 0$, with α , and $\sigma > 0$, the Tsai-Wu criterium is expressed by the following equation.

$$f = \frac{\sigma^2}{X_t X_c} + \frac{\alpha^2 \sigma^2}{Y_t Y_c} + \left(\frac{1}{X_t} - \frac{1}{X_c} \right) \sigma + \left(\frac{1}{Y_t} - \frac{1}{Y_c} \right) \alpha \sigma + 2F_{12} \alpha \sigma^2 \quad (1.14)$$

where X_t and X_c represent the tensile and compressive strengths, respectively, in fiber direction. Y_t and Y_c represent tensile and compressive strengths, respectively, in transverse direction being perpendicular to the fibers orientation. As in the previous criterium the failure occurs when $f > 1$. Figure 1.5 shows a plot that represents the percentage of use of this four addressed criterium.

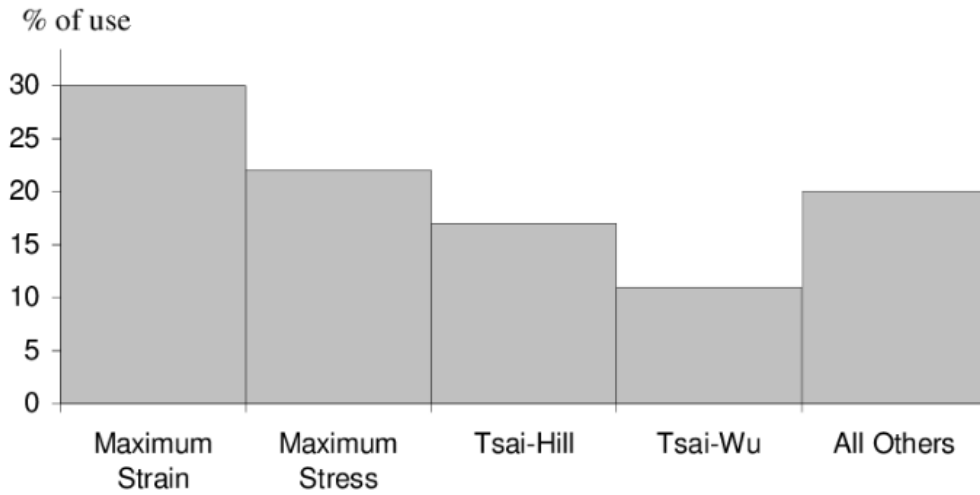


Figure 1.5: Use percentage of the four failure criteria [Camanho, 2002]

As can be seen, the maximum strain and maximum stress criteria are the ones used the most. However, using the FEM package Ansys, always presenting the worst-case scenario, all four criteria are considered in this work. There are many other criteria, although they will not be used nor discussed.

1.6 Hybrid Composites

Hybrid composites might be the answer to the problem of having better damping capability without compromising stiffness and strength. Hybrid composites are made of different fibers in a single matrix [Hay, 2015]. The main goal of this type of material is to take advantage of the strengths of each material. Therefore, it is easier to have a unique material that can respect all the needed requirements [Fiore et al., 2012; Hay, 2015]. In this study, the hybrid composite is composed of two different fibers and a common matrix. One of the fibers is a synthetic fiber (carbon fiber), and the other is a natural fiber (flax fiber). This hybrid composite can take advantage of the excellent stiffness-to-weight ratio and higher strength of the carbon fiber with the damping capability of the natural fibers. This is the so-called hybrid effect. Consequently, the structural requirements are accomplished, and the damping capacity of the material is higher, leading to higher comfort for the cyclist.

1.7 Carbon Fibers

1.7.1 History of Carbon Fibers

In recent years, carbon fibers have been increasingly important in various applications. Carbon fibers were used for the first time in the XIX century by Thomas Edison in 1879. He used carbon fiber filaments in his early experiments with light bulbs, which used electricity to heat a filament or a narrow strip of material until it lit up. In 1880, Thomas Edison discovered carbon fibers as filament materials and patented their use in his electric lamp. Those carbon fibers were manufactured using natural fibers like bamboo or cotton threads resistant to fire, an excellent property to be used in the incandescent filaments of his lamp [Park, 2018].

However, it was just in the 1960s that carbon fibers started to be used as a reinforcement material because they contributed significantly to higher strength and stiffness [Innovative Composite Engineering, 2022; Park, 2018]. Nowadays, carbon fibers are widely used in many applications where a strong, stiff, and lightweight material is needed. More common places to use carbon fibers are in applications like aerospace, motorsport, aircraft, military applications, and bike frames, where sometimes performance is more important than the price [Innovative Composite Engineering, 2022].

1.7.2 Structure and Chemical Composition

It is relevant to distinguish carbon fibers, the ones heat-treated at a temperature between 1000-1500°C and those heat-treated at a temperature above 2000°C. The first ones are called carbon fibers, and the others are called graphite fibers. The proportion of graphite in the carbon fibers can go from 0 to 100%. However, when this proportion is above 99%, the fibers are called graphite fibers. Usually, carbon fibers have at least 92 and up to 100 wt% (weight percentage). Carbon fibers are polycrystalline and are usually in a nongraphic stage. Their planar hexagonal networks have a two-dimensional long-range order of carbon atoms, but the third crystallographic direction (the z-direction) lacks any discernible order besides roughly parallel stacking. The atomic structure is very similar to the graphite one. The difference between them is the way the sheets are linked. Graphite's soft and brittle characteristics are caused by substantially weaker intermolecular forces (Van Der Waals) between each sheet [Park, 2018].

1.7.3 Characteristics of Carbon Fibers

As mentioned before, carbon fiber composites are widely used nowadays in applications where is needed a strong, stiff, and lightweight material. It is possible to have a lighter object and, at the same time, a strong material that achieves all the structural requirements. It also has a high chemical resistance and is temperature tolerant to excessive heat. However, it is not the perfect material. For example, carbon fiber composites are not recyclable. The other considerable disadvantage is that carbon fiber composites are expensive compared with materials usually used for the same applications. This way, we must decide when to use this material, for example, if performance and weight are above price in importance. If the answer is yes, then carbon fiber composites should be used. In summary, the advantages and disadvantages of carbon fiber composites are presented in the following topics.

Advantages of Carbon Fiber Composites:

- Lightweight material [Composites Construction UK, 2022; Innovative Composite Engineering, 2022];
- High stiffness [Composites Construction UK, 2022; Innovative Composite Engineering, 2022];
- High chemical resistance [Innovative Composite Engineering, 2022];
- High tolerance to excessive heat [Innovative Composite Engineering, 2022];
- High performance material.

Disadvantages of Carbon Fiber Composites:

- Not recyclable [Composites Construction UK, 2022];
- Very expensive [Composites Construction UK, 2022];
- Prone to wear and impact damage in bicycles [Norman, 2022].

1.8 Flax Fibers

1.8.1 History of Flax Fibers

Although it is often referred to as a new material, flax fiber composites are not new. Baley et al. [2021] said that Norman De Bruyne was one of the pioneers in the area of plant fiber composites used in structural applications. They also mentioned that many authors consider that his work was the start of the use of composites for structural applications.

Fiore et al. [2012] referred that flax and hemp fibers were used for the bodywork of a Henry Ford car, which claimed to have an impact strength ten times greater than steel. As can be seen, flax fiber composites are not a new material once they were already used in the past. Fiore et al. [2012] also mentioned that flax fiber composites are the most widespread natural fiber used in the European automotive industry nowadays, representing 71% of the natural fibers consumed in the year 2000. According to Rahman [2021], flax fibers are becoming widely used nowadays not only on load-bearing structures but also in applications to reduce audible noise and vibrations in transports (car, boats and planes) and in sport and leisure (tennis rackets, bicycles and skis) as a consequence of their good damping properties. The seat of McLaren's Formula 1 car is a prominent example of the use of flax fibers nowadays. The first race that McLaren used this flax fibers seat made by a partnership of the Swiss company Bcomp and McLaren Racing Team was in Lando Norris's car at the 2021 British Grand-Prix. In that race he piloted the seat to an amazing 4th place. The mechanical qualities of flax make it an appealing renewable raw material for high-performance composites, despite the obvious environmental advantages. Flax fibers' tubular structure, which has low density and high stiffness, allows for weight reduction while also enhancing vibration damping and resistance to breaking, torsion, and compression. A sustainability analysis by the team has showed that this natural fibers allow the team to reduce the emissions of CO₂ in 85% on Lando's seat. In the Figures 1.6, and 1.7, it is possible to see the seat.



Figure 1.6: McLaren's Formula 1 car seat made of flax fibers [Bcomp, 2022]



Figure 1.7: McLaren's Formula 1 car seat made of flax fibers [Bcomp, 2022]

In addition to the seat, McLaren Racing Team found out that if flax fibers were used to make timing stands and engineers' islands that would lead to a significant reduction of 3450 kg in travelling freight. Considering that team's equipment has to be moved all over the world at least 23 times a year this weight reductions have a big impact.

1.8.2 Structure and Chemical Composition

Before analyzing the structure and chemical composition of the flax fiber, it is important to know the natural fibers classifications and where the flax fibers fit in this classification. Natural fibers can come from a variety of sources, as can be seen in Figure 1.8.

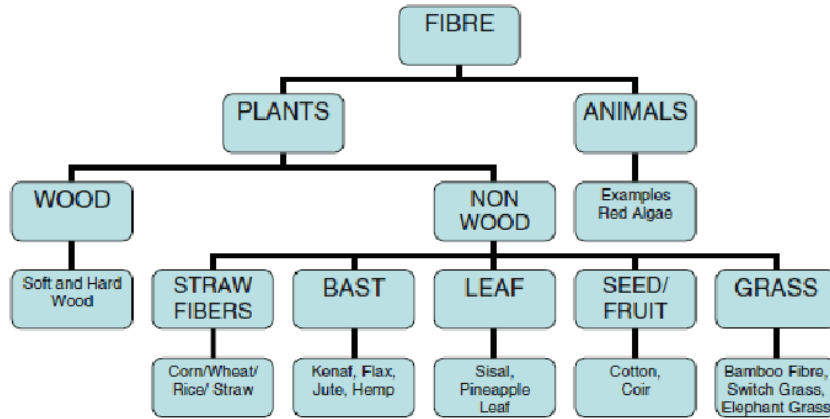


Figure 1.8: Classification of natural fibers [Petinakis et al., 2013]

Flax fibers are non-wood plant fibers. Inside the non-wood plant fibers, they are called bast fibers and are similar to kenaf, jute, and hemp fibers once they share a similar structure. In the Figure 1.9 it is possible to see the structure of flax fiber.

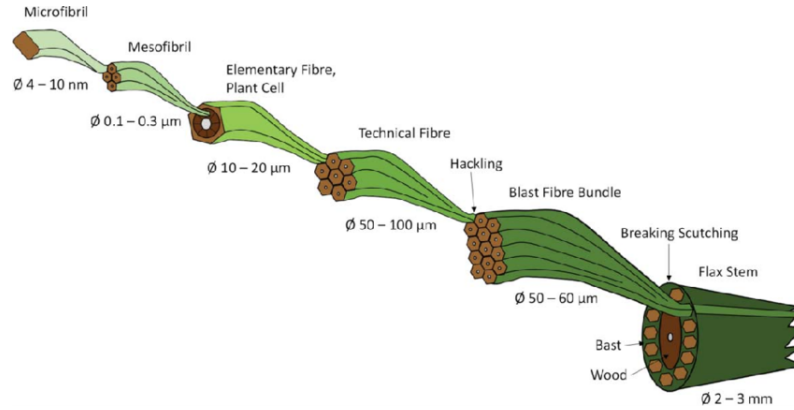


Figure 1.9: Structure of a flax fiber [Güven et al., 2016]

Flax fibers are produced in the stems of the flax bast plant. Flax fiber is a cellulose polymer like cotton that has a more crystalline structure, making this fiber much stronger, crisper and stiffer [Yan et al., 2014]. The flax fibers used in composites vary from fiber bundles to elementary fibers. Between these forms, mechanical properties can be different [Güven et al., 2016]. Technical fibers have approximately one meter long and are isolated from the flax plant to be used in the textile industry. These fibers have lengths normally between 2-5 cm and diameters of 10-25 μm . Elementary fiber are bonded together by a pectin interface. This fibers are not circular but a polyhedron with 5 to 7 sides. This increases the packing in the technical fibers [Vanwalleghem, 2009]. The bond between this elementary fibers is poor and decreases the strength of the fibers.

Flax fibers are composed of cellulose, hemicellulose, wax, lignin, and pectin in different quantities, as shown in Table 1.3.

Table 1.3: Different chemical compositions (%) of flax fibers [Rahman, 2021].

Cellulose	Hemicellulose	Pectin	Lignin	Wax	Moisture Content
71-75	18.6-20.6	2.2	2.2	1.7	10
62-72	18.6-20.7	2.3	2-5	1.5-1.7	8-12
64.1	16.7	1.8	2	1.5	10
73.8	13.7	-	2.9	-	7.9
71-78	18.6-20.6	2.3	2.2	1.7	7

The different compositions in the constituents are due to environmental factors like soil quality, rain, and temperature, but also due to plant maturity and the retting process. As will be discussed later in this work, this can cause variations in the mechanical properties of the flax fibers. The main constituent of the flax fiber is cellulose, as can be seen in Table 1.3. This constituent gives flax fibers the required stiffness to be used on structural composites. However, this constituent makes the flax fiber more hydrophilic. This means that the adhesion between the fiber and the matrix (hydrophobic) will be weak, resulting in poor resistance to moisture [Rahman, 2021].

1.8.3 Flax Fibers Characteristics

In this section, some advantages and disadvantages of the flax fibers are presented.

Advantages of Flax Fiber Composites:

- Low density that results in high specific stiffness [Rahman, 2021], [Duc et al., 2014], [Pil et al., 2016];
- Low environmental impact, biodegradable and renewable [Rahman, 2021], [Duc et al., 2014], [Pil et al., 2016], [Baley et al., 2021];
- Lightweight [Rahman, 2021], [Duc et al., 2014], [Pil et al., 2016], [Fiore et al., 2012], [Baley et al., 2021];
- Cheaper than conventional synthetic fibres [Rahman, 2021], [Pil et al., 2016], [Fiore et al., 2012];
- High vibration damping capability [Rahman, 2021], [Duc et al., 2014], [Pil et al., 2016].

Disadvantages of Flax Fiber Composites:

- Low impact strength [Hay, 2015];
- Hydrophilic plant fibres that leads to poor resistance to moisture [Rahman, 2021], [Fiore et al., 2012] ;
- Poor hydrophilic fiber/hydrophobic matrix adhesion [Rahman, 2021], [Fiore et al., 2012] ;
- Lower durability [Rahman, 2021];
- High variability of properties depending on growing and processing conditions [Rahman, 2021], [Fiore et al., 2012] ;

- Susceptibility to microbial attack and rotting [Güven et al., 2016], [Hay, 2015];
- Restricted processing temperature due to low decomposition temperature of chemical components [Güven et al., 2016], [Hay, 2015].

Analyzing all these properties, it is easy to understand why these "new" materials are becoming more widely studied and essential in the industry. Compared with conventional syntectic fibers like glass, the stiffness of flax fibers is lower. However, as flax fiber composites have a lower density, their specific stiffness is higher, which is excellent [Rahman, 2021]. The fact that these fibers have a lower environmental impact is an amazing advantage regarding sustainability. The main advantage in the context of this work is the higher vibration damping properties compared with glass and carbon fibers [Duc et al., 2014]. This capability is important if used in a handlebar because it decreases the vibrations felt by the cyclist, consequently increasing comfort. The main disadvantages are the low impact strength and the lower stiffness than carbon fiber composites. The high variability of the properties occurring due to different processing and growing conditions of the flax fibers, is also a downside. The other disadvantages are worth mentioning but not so important in the context of this work. Sometimes, the use of hybrid composites is worth exploring for applications where stiffness, strength, and also high vibration damping capability are required, which is the case here.

1.8.4 Damping Capability of Flax Fiber Composites

As mentioned before, one of the best characteristics of flax fibers composites is their high vibration damping capability. In recent years, this material has been used more and more in the industry due to this capability, but also to high specific stiffness and low environmental impact. Therefore these materials are excellent candidates for applications in sports goods where the comfort of the user is crucial for good performance [Pil et al., 2016]. As previously mentioned, the lower the vibration amplitude, the more comfort for the user. The dynamic characteristics of a given structure are determined by damping, along with mass and stiffness. While stiffness is associated with the storage of elastic energy and mass is associated with kinetic energy, damping relates to energy dissipation. This energy dissipation is the conversion of mechanical energy into other forms, such as heat, which occurs within materials due to imposed deformations. Free and transient vibrations dissipate faster as vibration damping in a system is increased, while vibration amplitudes of structures at resonances and self-excited vibration amplitudes are reduced [Rahman, 2021]. Composite materials have some unique mechanisms to achieve damping due to being anisotropic. Damping in flax fiber composites is slightly different from conventional materials such as polymers, metals, and alloys. So the excellent damping properties of flax fibers composites are due to:

- Viscoelastic nature of the matrix and/or fiber material. In composites with a polymer matrix, this effect is significant. [Chandra et al., 1999; Hou et al., 2016; Rahman, 2021];
- Damping due to the interface between the reinforcement and the matrix. When a fiber is embedded into a bulk matrix, the interface is the region next to the fiber surface along the fiber's length. The nature of this interface affects the mechanical and damping properties of the material. Therefore, the interface has a big influence on the damping properties. It is also important to notice that sometimes an improvement in the adhesion between the reinforcement and the matrix can decrease

the damping capacity [Chandra et al., 1999; Hay, 2015; Rahman, 2021]. However, an improvement in bonding between fiber and matrix results in better mechanical behavior due to the better transmission of stresses along the material;

- Damping due to damage or crack propagation [Hay, 2015; Rahman, 2021];
- Damping may also be promoted by voids [Hay, 2015; Rahman, 2021];
- Viscoplastic damping at high stress and strain shows non-linear damping at the high amplitude of vibrations. The contribution of plasticity to damping is greater than the other dissipation sources due to the high amplitude of vibration [Daoud et al., 2017; Rahman, 2021];
- Damping can also occur due to the cyclic heat flow from a region of compression to a region of tension as a function of the load, frequency, thickness of laminate, and number of cycles [Hay, 2015].

Also, the unique architecture of flax fibers has inherent additional damping mechanisms. The fact that the fibers are hollow can decrease the bulk density and act as an acoustic insulator. Natural fibers are composite materials. Thereby, the intrinsic damping can be increased because of the energy dissipation in each cell wall and between cells [Hay, 2015]. The fiber yarn architecture with the inter/intra yarn friction increase also the energy dissipation. However, it is important to realize that by increasing the damping capability, stiffness and strength of the material decrease. This means that a trade-off between stiffness, strength, and damping is needed to reach a better performance of the material.

Fiber Aspect Ratio

The fiber aspect ratio is the relation between length and diameter of the fiber (l/d). Fibers with smaller diameters produce better damping than fibers with larger diameter fibers [Gibson et al., 1982; Suarez et al., 1986]. This is because, for smaller fiber diameters, there is a more extensive interface area. Therefore the energy dissipation is higher. Also, shorter fibers create more interfaces between fibers and the matrix, which results in more energy dissipation [Etaati et al., 2014]. So, as discussed, the fiber aspect ratio influences the vibration damping capability. However, the fiber orientation has much more influence on damping than the fiber aspect ratio [Rahman, 2021].

Fiber Orientation

The damping of the composites depends on the fiber orientation. Rahman et al. [2017] tested beam samples of flax/PP with different fibers orientation (0° , 30° , 45° , 60° , and 90°). The maximum damping occurred at the sample with a fiber orientation of 45° . Hadi and Ashton [1996] tested beams samples of unidirectional E-glass/epoxy using different fibers orientations (0° , 30° , 45° , 60° , and 90°). They found that the maximum damping occurs at a fiber orientation of 30° . The maximum damping occurs for that angle because there is maximum strain energy at that orientation. This means that the damping depends on the fiber orientation but also depends of the materials. Gao et al. [2011] used beams samples of carbon fiber/epoxy with fibers orientations from 0° to 90° with increments of 15° . The highest damping occurred at a fiber orientation of 45° . They also reported that natural frequencies decrease with the increase of fiber orientation.

Interface Between Fibers and Matrix

As previously mentioned, a better interface bonding between the fiber and matrix can result in a decrease in damping. This happens due to the fact that the mobility of molecular chains at the interface is reduced. Seng Chua [1987] reported that UD glass fiber/polyester composite samples with poor interface bonding tend to dissipate more energy than the samples that have a good bonding between fibers and matrix.

Effect of Frequency

[Rahman, 2021] says that the damping of flax/PP composites increases with increasing frequency. Regardless of the volume fraction or fiber orientation, the increase is about 25- 60% over the frequency range of 1000 Hz. [Mahmoudi et al., 2019] also reported the relation between damping and frequency. It said that the increase of damping with frequency results from interactions between fibers and between fibers and matrix.

Effect of Bending and Twisting

The twisting mode of flax/PP composite beams promotes an increase in damping of about 153% compared to the damping in the bending mode. This is due to the twisting deformation of the composite beam as well as the fact that, in comparison to the bending response peaks, the twisting response displays wider resonance peaks [Rahman, 2021].

Effect of Temperature and Moisture

Damping increases with the increase in temperature [Rahman, 2021]. The increase in temperature results in a softening of the matrix, allowing higher mobility of the molecular chains, which consequently increases damping capability. Softening the matrix will decrease the natural frequencies. Cheour et al. [2016] found out that the water immersion of flax fibers increases the loss factors. This means an increase in damping. It is also important to highlight that water immersion results in a decrease in other mechanical properties. After drying, damping can return to the same. However, other mechanical properties are not reversible. This way, water immersion affects those mechanical properties permanently.

1.9 Motivation

The motivation for this work is to improve the comfort of mountain bike's handlebars. The comfort of an handlebar can be analyzed using two approaches: the static comfort, related to the cyclist's position while holding it, and the dynamic comfort, related to the vibrations felt by the cyclist when holding the handlebar. Dynamic comfort is the main motivation for this work. The comfort of cyclists is an important topic because they spend a lot of time riding, and if the comfort is higher, it will be easier for them to achieve better performances. For people that ride bike for fun, the ride will be more pleasant. Therefore, the objective is to develop a handlebar more comfortable than those already available in the market. As seen previously, flax fiber composites have excellent damping properties compared with traditional materials used in handlebars. Therefore, it was decided to study a handlebar incorporating flax fiber composites. In addition to the damping capability, flax fibers, as natural fibers, have a lower environmental cost. As mentioned before, the main concern is that flax fiber composites could not handle all the static requirements. Consequently, carbon fiber composites could be used with flax fibers composites. This

way, the handlebar will be more comfortable, will have the necessary static requirements, and, finally, will have a lower environmental impact than the traditional handlebars.

1.10 Objectives

The main objective of the present work is to develop a bicycle handlebar that is more comfortable than commercial handlebars with a lower environmental impact. However, the performance cannot be forgotten. So the solution has to achieve an equilibrium between three parameters: comfort, sustainability, and performance. As already mentioned, flax fiber composites are one of the materials that can make it happen. To do this is important to:

- Benchmark of commercial handlebars at static and also dynamic level;
- Recognize whether a flax fiber handlebar can meet the essential static requirements without being heavy;
- Investigate the impact of different types of flax fiber composites;
- If the second objective is not accomplished, develop a solution made of flax and carbon fiber composites providing more stiffness and strength to the handlebar;
- Study the best combination of flax and carbon fiber composite plies;
- Study the best position for flax fiber plies to increase the damping capacity of the handlebar.

1.11 Layout

This master thesis is divided into five chapters, and it is organized as follows:

- **Chapter 1** - “Introduction”: This chapter addresses the relevance and motivation for this work. In addition, it contains a contextualization of bicycles and the materials traditionally used to manufacture them. Besides, the materials used in this work are extensively reviewed.
- **Chapter 2** - “Background Theory”: In this chapter, the ISO standard for bicycle safety requirements is presented. An introduction to mechanical vibrations and how they influence the cyclist’s comfort are also presented in this chapter. The experimental methods used to study the dynamic behavior of handlebars are discussed.
- **Chapter 3** - “Experimental Tests”: In this chapter, the results from the stiffness tests for a cylinder tube used for reference and validation and selected commercial handlebars are presented and discussed. The results of the dynamic tests of the cylinder tube and the commercial handlebars are also shown and discussed.
- **Chapter 4** - “FEM”: The subject of this chapter is all related to the simulations made in the commercial Ansys using the Finite Element Method. It is probably the most important chapter because it is the one where the process of developing the handlebar is described.

- **Chapter 5** - “Conclusion”: Finally, the last chapter is the one where all the conclusions discussed in this work are presented. Besides, this chapter proposes suggestions for future work on this subject, aiming to optimize and improve the results reported in this thesis.

Background Theory

Nowadays, safety is critical. Everything is becoming standardized to reduce the number of failures and accidents. Bicycles also have their standards, and all bicycle designers must follow those rules and pass all the tests to have their products on the market. Standards are also important to help people all over the world once some components have equal dimensions, and this way is better in all aspects.

2.1 Lateral Bending Test (ISO 4210-5:2014)

In the Standard “Cycles Safety requirements for bicycles Part 5: Steering test methods (ISO 4210-5:2014)”, it is possible to analyze the lateral bending test to apply to handlebars [for Standardization]. Usually, the handlebar is clamped at the center by the stem. In this work, the stem is not used to attach the handlebar but a fixed support that has the same effect. It is applied a load at a distance of 50 mm from the end of the handlebar. In this work, the vertical displacement was measured at a distance of 15 mm from the end of the handlebar. Figure 2.1 shows a representation of this test.

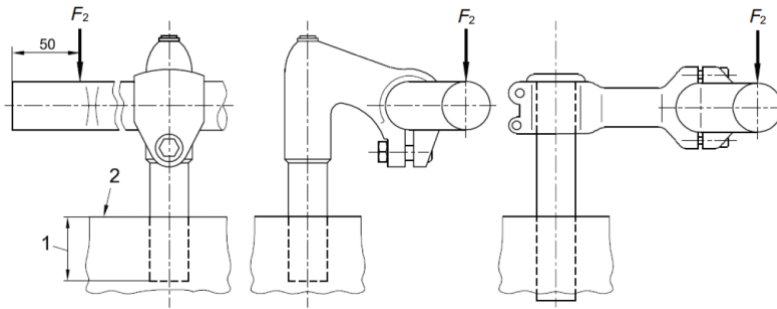


Figure 2.1: Representation of the Lateral Bending Test of the handlebar [for Standardization]

Table 2.1 shows the Lateral Bending Test Load for different bicycles. The load considered in this work was 1000 N because the handlebar was for a mountain bike.

Table 2.1: Lateral bending test load for different bicycles [for Standardization]

Bicycle	City Bikes	Young Adult Bikes	Mountain Bikes	Road Bikes
Force F_2 (N)	600	600	1000	1000

2.2 Fatigue Test (ISO 4210-5:2014)

Beyond the Lateral Bending Test, the Fatigue Test is also an important test to which the handlebar must be submitted. The main goal of this test is to check if the handlebar can handle the loads submitted for a long time. The setup for this test is the same as in the Lateral Bending Test, being the handlebar clamped by the stem. The loads to which the handlebar is submitted can be in phase or out of phase. Figure 2.2 shows a representation of this test.

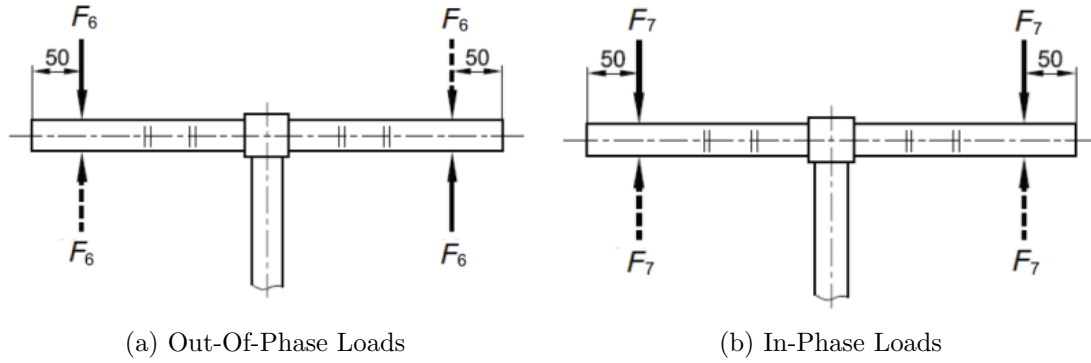


Figure 2.2: Representation of the Fatigue Test of the handlebar [for Standardization]

Table 2.2 shows the loads that should be applied in the Fatigue Test using each method for various types of bicycles. The forces must be applied during 100000 cycles not exceeding the maximum frequency of 10 Hz.

Table 2.2: Fatigue test loads for different bicycles [for Standardization]

Bicycle	City Bikes	Young Adult Bikes	Mountain Bikes	Road Bikes
Out-Of-Phase - F6 (N)	200	200	270	280
In-Phase - F7 (N)	250	250	450	400

2.3 Mechanical Vibrations

Many human activities have different types of vibratory phenomena. Vibration is part of our life, and everyone has a notion of vibration. Vibration is not always a bad thing. For example, the sound of a guitar is only possible due to the vibration of the strings. However, in mechanical engineering, vibrations are generally undesirable because they can disturb the proper functioning of machines and objects. Mechanical vibrations are the system response when a perturbation is applied. In a project of a machine or structure subjected to dynamical solicitations, if engineers do not have a dynamic analysis into consideration, they can reach frequencies that can cause huge deformations that can lead to rupture. In addition, vibrations in machines or structures can cause problems in other types of equipment and also cause discomfort in nearby people or people using the equipment. Thereby, it is important to study vibrations and always try to decrease them to a minimum.

2.3.1 Free Response of a Single Degree-Of-Freedom System

In this section, it will be presented the single degree-of-freedom system with a spring and a damper. In Figure 2.3, it is possible to see the representation of the system.

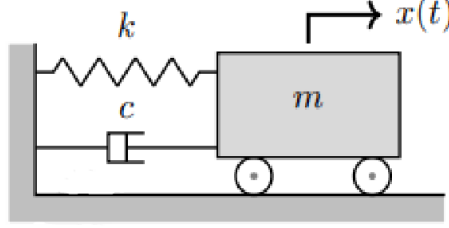


Figure 2.3: Representation of a single degree-of-freedom system [Rodrigues, 2020]

The equation of motion of this system can be written as:

$$m\ddot{x}(t) + c\dot{x}(t) + kx = 0 \quad (2.1)$$

In equation 2.1, m is the mass of the system, c represents the damper constant, and k represents the constant of the spring. Solving the characteristic equation, its roots can be written as:

$$s_{1,2} = -\zeta\omega_n \pm \omega_n\sqrt{\zeta^2 - 1} \quad (2.2)$$

where ζ is the damping ratio of the system and ω_n is the natural frequency of the system, being expressed by the following equations:

$$\omega_n = \sqrt{\frac{k}{m}} \quad (2.3)$$

$$\zeta = \frac{c}{2m\omega_n} \quad (2.4)$$

Analyzing Equation 2.2, it is possible to conclude that the value of the damping ratio determines if a system has real or complex roots. Therefore there are four types of systems:

- Undamped ($\zeta=0$);
- Underdamped ($0<\zeta<1$);
- Critically damped ($\zeta=1$);
- Overdamped ($\zeta>1$).

The graphic representation of these four types of damping can be seen in Figures 2.4, 2.5, 2.6, and 2.7.

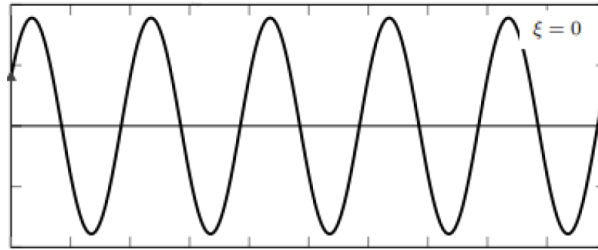


Figure 2.4: Free response of the undamped system [Rodrigues, 2020]

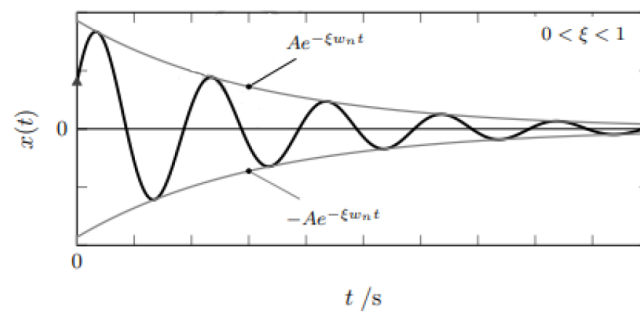


Figure 2.5: Free response of the underdamped system [Rodrigues, 2020]

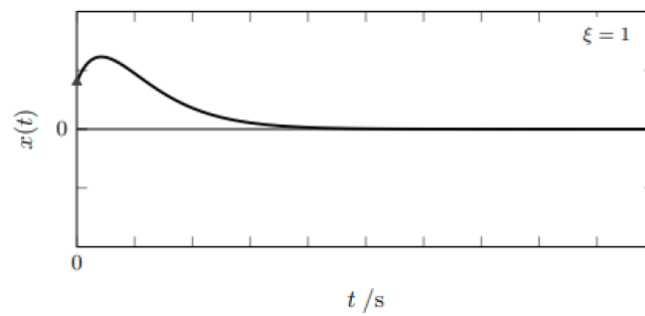


Figure 2.6: Free response of the critically damped system [Rodrigues, 2020]

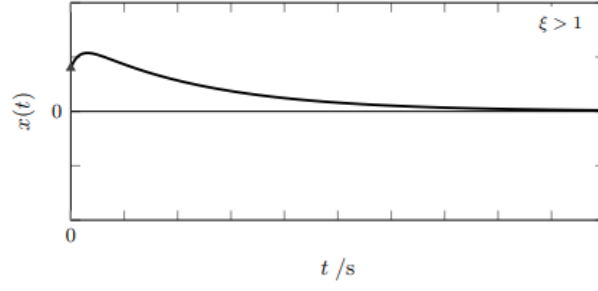


Figure 2.7: Free response of the overdamped system [Rodrigues, 2020]

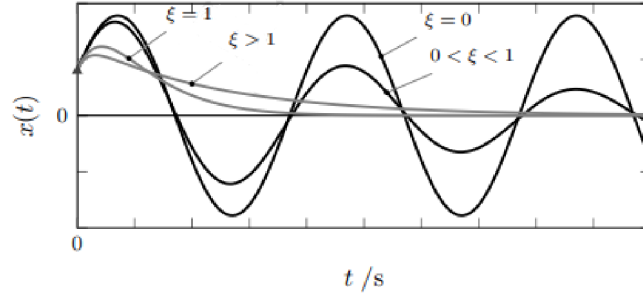


Figure 2.8: Free response of the system for different damping ratios [Rodrigues, 2020]

The sooner the frame reaches the static equilibrium position, the less vibration will occur, and the damping response will be better. Drawing the parallel for the handlebars, the greater the damping, the better the vibration response, and the greater the rider's comfort.

2.3.2 Harmonic Regime and Complex Exponential

Consider a system subjected to an external harmonic load of amplitude F and frequency ω . Using the complex exponential, the harmonic load has the following form:

$$f(t) = F e^{j\omega t} \quad (2.5)$$

F represents the amplitude of the harmonic excitation load and ω represents the frequency. The differential equation of motion for the single degree-of-freedom system in Figure 2.9 is given by:

$$m\ddot{x}(t) + c\dot{x}(t) + kx = F e^{j\omega t} \quad (2.6)$$

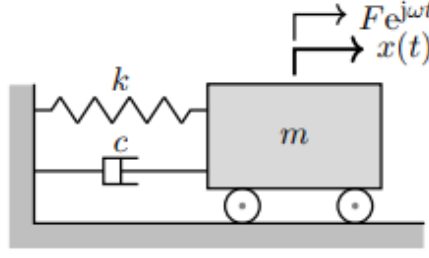


Figure 2.9: Representation of a single degree-of-freedom system subjected to a harmonic load [Rodrigues, 2020]

The particular solution $x(t)$ of the differential equation of motion represents permanent or stationary vibration due to external excitation.

$$x(t) = \bar{X}(j\omega)e^{j\omega t} \quad (2.7)$$

$\bar{X}(j\omega)$ is a complex quantity called phasor. Velocity and acceleration are given by the following equations:

$$\dot{x}(t) = j\omega \bar{X}(j\omega)e^{j\omega t} \quad (2.8)$$

$$\ddot{x}(t) = -\omega^2 \bar{X}(j\omega)e^{j\omega t} \quad (2.9)$$

Replacing 2.7, 2.8 and 2.9 in the differential equation of motion, the following equation can be written:

$$\bar{X}(j\omega) = F \frac{1}{(k - \omega^2 m) + j\omega c} \quad (2.10)$$

The stationary response can be written in the following way:

$$x(t) = F \frac{1}{(k - \omega^2 m) + j\omega c} e^{j\omega t} \quad (2.11)$$

The phasor $\bar{X}(j\omega)$ contains information about the amplitude of the response given by its modulus. It also has information concerning the lag between the response and the excitation. The phasor $\bar{X}(j\omega)$ can be written in the following way:

$$\bar{X}(j\omega) = |\bar{X}(j\omega)|e^{-j\phi} = X(\omega)e^{-j\phi} \quad (2.12)$$

where $X(\omega)$ represents the amplitude of the stationary motion and ϕ represents its phase. These values are given by the following equations:

$$X(\omega) = |\bar{X}(j\omega)| = F \frac{1}{((k - \omega^2 m)^2 + (\omega c)^2)^{\frac{1}{2}}} \quad (2.13)$$

$$\phi = \tan^{-1} \left(\frac{\omega c}{k - \omega^2 m} \right) \quad (2.14)$$

The stationary response can also be written by the following equation:

$$x(t) = X(\omega)e^{j(\omega t - \phi)} \quad (2.15)$$

2.3.3 Frequency Response Function

Receptance

Let us consider the stationary response $x(t) = X(j\omega)e^{j\omega t}$ to the excitation $f(t) = Fe^{j\omega t}$, where $X(j\omega)$ is given by 2.13. The frequency response function from the receptance type is defined by the relationship between the phasor $X(j\omega)$ and the force amplitude F .

$$\alpha(j\omega) = \frac{\bar{X}(j\omega)}{F} = \frac{1}{(k - \omega^2 m) + j\omega c} \quad (2.16)$$

It is important to refer that FRF is a complex function of independent variable ω and depends only on the system properties like m , c , and k (mass, damping, and stiffness parameters, respectively). So, it is a unique characteristic of the system used to describe the vibrational behavior of the system directly from the frequency domain. FRF $\alpha(\omega)$ has information about the amplitude of the response given by its module and the lag between the response and the excitation. The receptance can be written by the following equation:

$$\alpha(j\omega) = |\alpha(j\omega)|e^{-j\phi} \quad (2.17)$$

$|\alpha(j\omega)|$ represents the amplitude and ϕ the phase. Therefore, the stationary response can be given by:

$$x(t) = \bar{X}(j\omega)e^{j\omega t} = F\alpha(j\omega)e^{j\omega t} \quad (2.18)$$

or

$$x(t) = F|\alpha(j\omega)|e^{j(\omega t - \phi)} \quad (2.19)$$

The receptance can also be expressed by its real and imaginary parts. In the following equation are presented those components.

$$\text{Re}[\alpha(j\omega)] = \frac{k - \omega^2 m}{(k - \omega^2 m)^2 + (\omega c)^2} \quad (2.20)$$

$$\text{Im}[\alpha(j\omega)] = \frac{\omega c}{(k - \omega^2 m)^2 + (\omega c)^2} \quad (2.21)$$

In the following, equations for receptance amplitude and its phase are presented.

$$|\alpha(j\omega)| = \frac{1}{((k - \omega^2 m)^2 + (\omega c)^2)^{\frac{1}{2}}} \quad (2.22)$$

$$\phi = \tan^{-1} \left(\frac{\omega c}{k - \omega^2 m} \right) \quad (2.23)$$

Mobility

FRFs can also be defined in terms of velocity response, represented by $Y(j\omega)$, and given by the relationship between the velocity phasor $\bar{V}(j\omega)$ and the force amplitude F .

$$Y(j\omega) = \frac{\bar{V}(\omega)}{F} = \frac{\omega \bar{X}(\omega)}{F} = \omega \alpha(\omega) \quad (2.24)$$

Therefore, mobility is given by the following equation:

$$Y(j\omega) = j\omega \frac{1}{(k - \omega^2 m) + j\omega c} \quad (2.25)$$

where the real and imaginary parts are given by:

$$\text{Re}[Y(j\omega)] = \frac{\omega^2 c}{(k - \omega^2 m)^2 + (\omega c)^2} \quad (2.26)$$

$$\text{Im}[Y(j\omega)] = \frac{\omega(k - \omega^2 m)}{(k - \omega^2 m)^2 + (\omega c)^2} \quad (2.27)$$

and the magnitude and phase given by:

$$|Y(j\omega)| = \frac{\omega}{((k - \omega^2 m)^2 + (\omega c)^2)^{\frac{1}{2}}} \quad (2.28)$$

$$\phi = \tan^{-1} \left(\frac{k - \omega^2 m}{\omega c} \right) \quad (2.29)$$

Accelerance

Besides receptance and mobility, FRFs can also be defined in terms of acceleration. This FRF type is called accelerance. Accelerance is defined by the relationship between the acceleration phasor $\bar{A}(j\omega)$ and the force amplitude F .

$$A(j\omega) = \frac{\bar{A}(j\omega)}{F} = \frac{j\omega \bar{V}(j\omega)}{F} = j\omega Y(j\omega) = \frac{-\omega^2 \bar{X}(j\omega)}{F} = -\omega^2 \alpha(j\omega) \quad (2.30)$$

This gives origin to the following equation.

$$A(j\omega) = -\frac{\omega^2}{(k - \omega^2 m) + j\omega c} \quad (2.31)$$

The real and imaginary components are given by:

$$\text{Re}[A(j\omega)] = -\frac{\omega^2(k - \omega^2 m)}{(k - \omega^2 m)^2 + (\omega c)^2} \quad (2.32)$$

$$\text{Im}[A(j\omega)] = \frac{\omega^2 \omega c}{(k - \omega^2 m)^2 + (\omega c)^2} \quad (2.33)$$

and the magnitude and phase are given by:

$$|A(j\omega)| = \frac{\omega^2}{((k - \omega^2 m)^2 + (\omega c)^2)^{\frac{1}{2}}} \quad (2.34)$$

$$\phi = \tan^{-1} \left(\frac{\omega c}{k - \omega^2 m} \right) \quad (2.35)$$

2.3.4 Circular Curve Fitting

The Circular Curve Fitting is a method to calculate the damping factors from the FRF plot. This method uses Nyquist's Diagram to determine the damping. Nyquist's Diagram from FRF is a detailed graphic representation of the frequency band around resonance. As previously discussed, the accelerance is given by equation 2.31.

Separating the real and imaginary parts, it is obtained:

$$\text{Re}[A(w)] = -\frac{1}{k} \frac{\omega^2 \left(1 - \left(\frac{\omega}{\omega_n}\right)^2\right)}{\left(1 - \left(\frac{\omega}{\omega_n}\right)^2\right)^2 + 4\xi^2 \left(\frac{\omega}{\omega_n}\right)^2} \quad (2.36)$$

$$\text{Im}[A(w)] = \frac{1}{k} \frac{2\xi \frac{\omega^3}{\omega_n}}{\left(1 - \left(\frac{\omega}{\omega_n}\right)^2\right)^2 + 4\xi^2 \left(\frac{\omega}{\omega_n}\right)^2} \quad (2.37)$$

Figure 2.10 shows Nyquist's Diagram of a mobility function. The same applies to Nyquist's Diagram of the accelerance function.

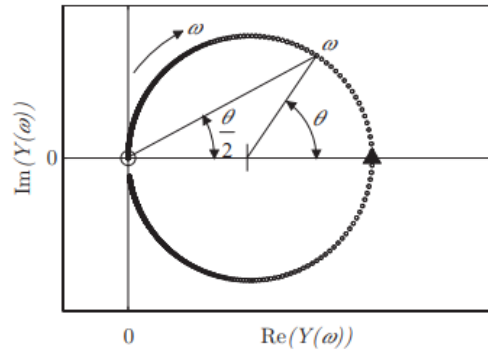


Figure 2.10: Nyquist's Diagram of a mobility function [Rodrigues, 2015]

The following relation is obtained from equations 2.36 and 2.37 for a given point with a given frequency and angle:

$$\tan\left(\frac{\theta}{2}\right) = -\frac{\text{Im}(A(\omega))}{\text{Re}(A(\omega))} = \frac{\frac{2\xi\omega}{\omega_n}}{1 - \left(\frac{\omega}{\omega_n}\right)^2} \quad (2.38)$$

The damping ratio can be determined by the following equation:

$$\xi = \frac{\omega_n^2 - \omega^2}{2\omega_n\omega} \frac{1}{\tan\left(\frac{\theta}{2}\right)} \quad (2.39)$$

Another way to calculate the damping ratio is to use 2 points. In Figure 2.11, it is possible to see Nyquist's Diagram for two points.

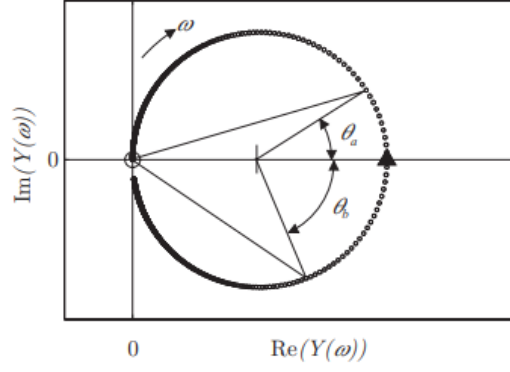


Figure 2.11: Nyquist's Diagram of a mobility function using 2 points [Rodrigues, 2015]

In this case, using equation 2.38, the following equations can be reached:

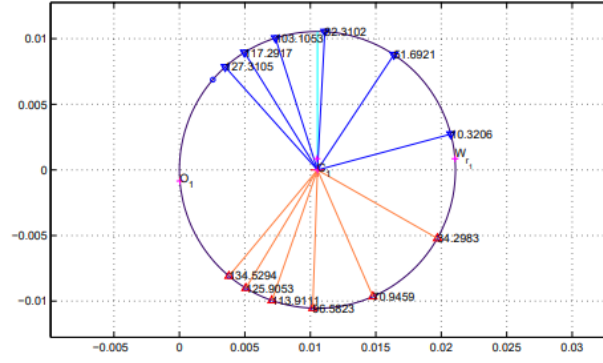
$$\tan\left(\frac{\theta_a}{2}\right) = \frac{\frac{2\xi\omega_a}{\omega_n}}{1 - \left(\frac{\omega_a}{\omega_n}\right)^2} \quad (2.40)$$

$$\tan\left(\frac{\theta_b}{2}\right) = \frac{\frac{2\xi\omega_b}{\omega_n}}{1 - \left(\frac{\omega_b}{\omega_n}\right)^2} \quad (2.41)$$

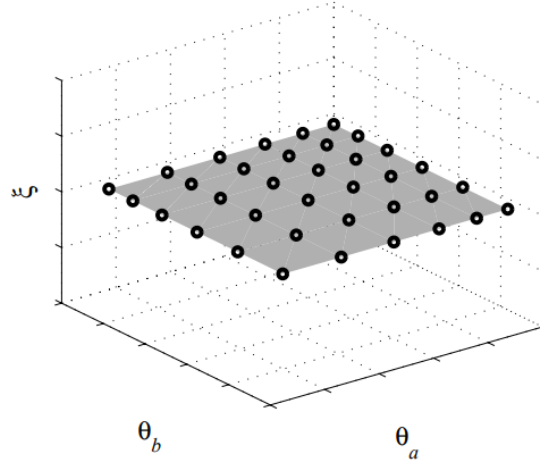
The damping ratio can be estimated by the following equation:

$$\xi = \frac{(\omega_b^2 - \omega_a^2)}{2\omega_n \left(\omega_a \tan\left(\frac{\theta_a}{2}\right) + \omega_b \tan\left(\frac{\theta_b}{2}\right) \right)} \quad (2.42)$$

A valid damping estimation should lead to a set of estimates that must define a flat and level surface. Figure 2.12 shows an example of a valid estimation.



(a) Nyquist's diagram



(b) Damping estimates for different points

Figure 2.12: Estimation and validation of damping ratios [Rodrigues, 2015]

2.4 Human Comfort in a Bicycle

As previously discussed, the comfort of riding a bicycle is a broad concept. This work focuses on dynamic comfort, and dynamical comfort is the comfort relative to the vibrations felt by the rider. In simple terms, disregarding the excitation frequencies, the higher the vibration amplitude, the lower the comfort. Obviously, if the rider isn't as comfortable as he should be, his performance will be worse. Also, for cyclists new to mountain biking, if they are not too comfortable, they will not enjoy the ride, and it will be easier for them to give up. Nevertheless, it is always important to emphasize that the designers have to focus on a trade-off between comfort and performance because it is not good to have excellent damping and poor performance. As mentioned before, the vibrations felt by the rider are transferred from the bicycle to the rider at three different contact points. These three contact points are the pedals, the saddle, and the handlebar. It is believed that most discomfort comes from the handlebar and the seat [Vanwalleghem et al., 2012]. The human body works as a mass-damper-spring system because it can absorb vibrations. It is this capacity of absorbing vibrations that causes fatigue and discomfort in the rider. To assess the interaction between the bicycle and the rider current studies generally employ three different methods: the whole body/hand vibration method as specified by ISO 2631 and ISO 5349, respectively, and the absorbed power method [Vanwalleghem et al., 2012],

[Vanwalleghem, 2009], [Hay, 2015].

2.4.1 Human Vibration Thresholds

2.4.2 Whole Body/Hand Vibration Method

The whole body vibration method and the hand vibration method are two standardized methods used to measure vibrations on the human body. These two methods have some limitations. Despite of this they are still used nowadays to measure vibrations and study bicycle behaviour. Both methods measure the acceleration obtained at the contact points between the rider and bicycle. The relation between acceleration and discomfort is that higher the acceleration higher is the discomfort. For this is used a weighted scale average that takes into consideration the acceleration direction. This is due to the fact that the human body is more sensitive to vertical vibrations than vibrations at any other directions [Hay, 2015], [Vanwalleghem, 2009], [Vanwalleghem et al., 2012]. The limitation of these two methods is that acceleration is not the best way to measure the discomfort of the rider. This can be explained by the fact that if a cyclist lifts himself out of the saddle or apply a minor force on the handlebar on a cobblestone road, the acceleration will be high. Although higher acceleration, in this case, doesn't increase discomfort because it is something that cyclists usually try to do to be more comfortable on these types of roads.

2.4.3 Absorbed Power Vibration Method

Unlike the other two methods, the absorbed power vibration method focuses on the force level transmitted to the hands. The absorbed power is a scalar value that results from the multiplication of the average power of the force and velocity of the signal throughout the time period at the point of contact, as can be seen in the following equation:

$$P_{abs} = F(t) \cdot v(t) \quad (2.43)$$

The lower the power loss, the better the rider's comfort. This is a better parameter to measure discomfort because the contact force seems to be more representative of human discomfort. This way, if the rider is not touching the saddle or handlebar, no vibration is transferred to him and consequently, he will be more comfortable. The whole body and hand vibration methods do not indicate this. Because of this, the absorbed power vibration method is much more accurate. Nevertheless, this method has also a limitation because it is a scalar value and cannot evaluate human sensitivity to directional components of acceleration. Despite this, the absorbed power seems to be more accurate to measure the level of discomfort compared with the whole body/hand vibration methods.

2.5 Experimental Methods in Bicycles

2.5.1 Experimental Modal Analysis (EMA)

Experimental Modal Analysis (EMA) can be used to examine a bicycle's dynamic behavior. It can be used on the road and in a lab, with or without a cyclist. Natural frequencies, modal damping, and modal shapes can all be identified through EMA.

Vibration Shaker Method

The vibration Shaker Method can be divided into different concepts: SIMO and MIMO. Single input and multiple output (SIMO) is when there is only one input and multiple

outputs. This input is a single shaker that can be connected to the front wheel axle exciting the bicycle with forces in-plane and out-of-plane directions. Multiple input and multiple output (MIMO) is a similar configuration [Champoux et al., 2007]. The major difference is that additional shakers can be connected to the handlebars, as can be seen in Figure 2.13.



Figure 2.13: Setup for SIMO and MIMO analysis [Champoux et al., 2007]

In both techniques, there are multiple measuring points along the bike. As mentioned before, these methods can be done with or without a cyclist. Champoux et al. [2007] report that the results for SIMO with or without a cyclist are completely different. The main difference between results with and without a cyclist is that the damping will be higher with a cyclist because the hands of the cyclist have a drastic effect on the bicycle's behavior due to energy transfer to the hands resulting in discomfort for him along the course. The results of natural frequencies of SIMO and MIMO with a cyclist are very similar. The damping ratios are a bit different depending on the technique. In the case of studying the handlebar alone, as in this work, a shaker and accelerometers on the handlebar can also be done to perform a dynamical analysis.

Impact Hammer Technique

This method can also be used to measure the dynamic behavior of the handlebar alone. In this case, the input is an impulse generated by an impact hammer. The vibration response is measured by accelerometers. The results that can be obtained by this method are natural frequencies and also the mode shapes that can be identified from the frequency response functions (FRFs) [Hay, 2015]. Besides, the damping factors can be identified using this

technique. In Figure 2.14 can be seen a graphic representation of this method. This is the method used in the dynamic tests of the handlebars performed in this work.

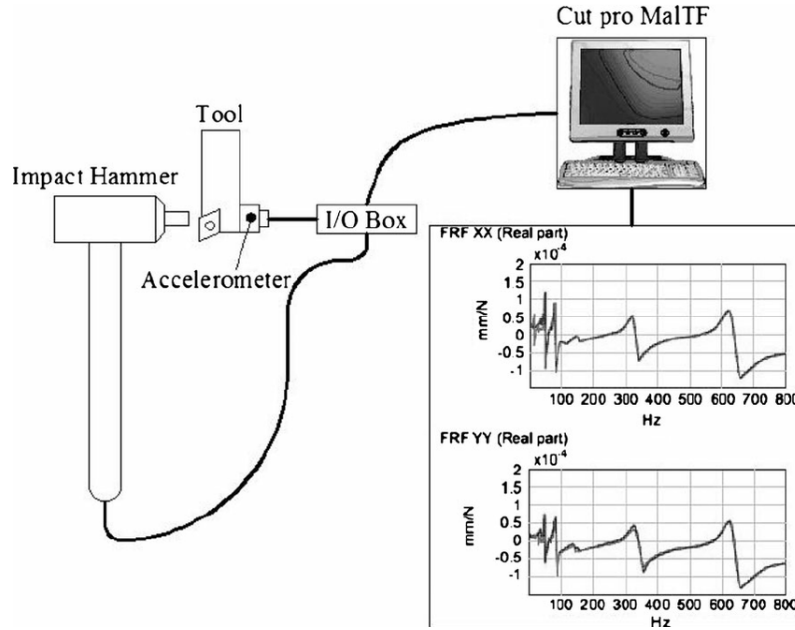


Figure 2.14: Representation of the impact hammer technique [Türkeş and Neşeli, 2014]

Impulse Excitation Technique - Microphone and Laser

The impulse excitation technique is another method that can be used to measure the dynamic behavior of the handlebar. In this method, the input is an impulse generated by a small tapping hammer. This tool is used in the same relative locations as in the impact hammer technique. The response from the handlebar can be measured by a microphone and a laser or both together. The microphone measures the noise and converts it into an electrical signal. The laser is responsible for measuring the displacement of the handlebar at a certain point. This method provides results about natural frequencies and the damping factors from Fast Fourier Transform (FFT) [Hay, 2015].

2.5.2 Operational Modal Analysis (OMA)

Operational modal analysis (OMA) is a method that, unlike the previous ones, can easily be performed outside the lab. Comparing the results from the lab and using OMA, it is possible to conclude if the results from the lab are close to real-life road conditions. The main difference between both is that there are no moving parts in the lab, including the wheels. The instrumentation used is just accelerometers that will measure the bicycle's behavior. Besides, it is needed a portable data acquisition system. This device can be carried in a backpack. During the test, all signals are transferred in real-time to a laptop on the side of the road with a long-range and high-speed wireless connection, for example. OMA can be divided into frequency-domain decomposition (FDD) and enhanced FDD (EFDD). The FDD technique estimates the mode shapes using a singular value decomposition (SVD) of the spectral density matrices. This decomposition corresponds to a single degree-of-freedom identification of the system for each value. FDD can be used to obtain natural frequencies and unscaled mode shapes. However, damping characteristics and more accurate resonant frequencies and mode shapes can be obtained using EFDD.

Champoux et al. [2007] demonstrated that MIMO gives more modes than OMA. This can be explained by the fact that there is not much energy in the road excitation to excite properly all these modes. [Champoux et al., 2007] concludes that there a good correlation between OMA and MIMO results. This way as testing in the lab is much more easier to conduct, MIMO is an excellent option to study the dynamic behaviour of a bike.

Experimental Tests

3.1 Stiffness Tests

Different stiffness tests performed for one aluminum cylinder and the three commercial handlebars are discussed in this section. The stiffness test consists in loading the structure with weights and registering the displacement of the structure according to the ISO 4210-5:2014 standard. The straight line's slope obtained by regression is the structure's flexural stiffness.

3.1.1 Cylindrical Aluminum Tube

The first test considered a 35 mm diameter aluminum cylindrical tube. The stiffness test was performed in this tube as a benchmark for the handlebars tested afterward. Besides, it also worked as setup and FEM model validation. Before presenting the obtained results, it is essential to show the geometric properties of the tube and discuss the setup for the stiffness tests.

Characteristics of the Cylindrical Tube:

- Material: Aluminum 6060
- Outside Diameter: 35 mm
- Inside Diameter: 32 mm
- Thickness: 1.5 mm
- Length: 0.4 m

The setup for the cylindrical tube considered an applied load at 50 mm from the end of the handlebar. The vertical displacement was measured with a dial indicator at 15 mm from the end of the handlebar, according to the ISO 4210-5:2014 standard, using a dial indicator with a resolution of 0.01 mm. Besides, the cylindrical tube was clamped by a clamping fixture. This way, the boundary conditions are in agreement with the ISO 4210-5:2014 - Lateral bending test of handlebars. Therefore, the results can be comparable to the handlebars. Figure 3.1 shows the setup of this stiffness test. The loads were applied with weights, as reported in Figure 3.1.



Figure 3.1: Setup for the stiffness test of the cylindrical tube

Figure 3.2 shows a representation of the setup where it is possible to notice the cylindrical tube in blue and the clamped region in green. All the experimental tests in this work were performed considering a tightening torque of 5 N.m for the bolts at the clamped region.

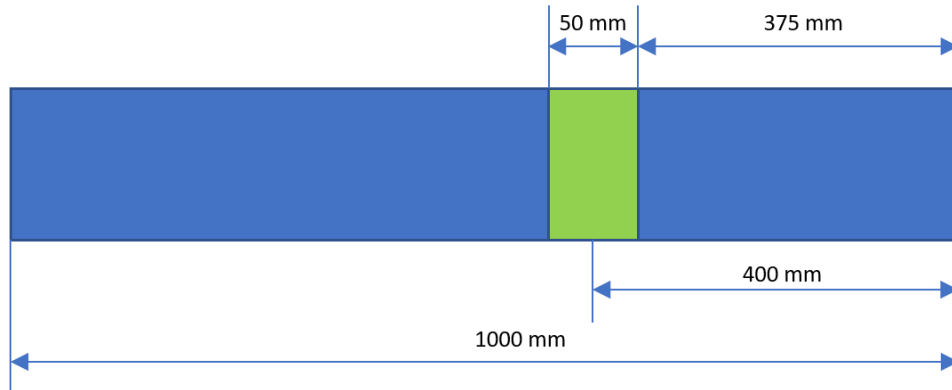


Figure 3.2: Representation of the setup for the stiffness test of the cylindrical tube

For the cylindrical tube the test was made only once. Table 3.1 presents the results of the stiffness test for the cylindrical tube.

Table 3.1: Displacement recording of the cylindrical aluminum tube

Load (N)	Displacement (mm)
0	0
20.39	0.16
40.28	0.38
60.25	0.61
79.92	0.85
99.80	1.10
120.79	1.35
140.60	1.61
160.46	1.85
178.23	2.06
195.76	2.30

It is possible with these values to do a stiffness plot. The higher the slope of the regression line, the higher the flexural stiffness. Figure 3.3 shows the flexural stiffness plot of the cylindrical tube. By linear regression, it is possible to estimate a flexural stiffness of 83.4 N/mm for the cylindrical tube.

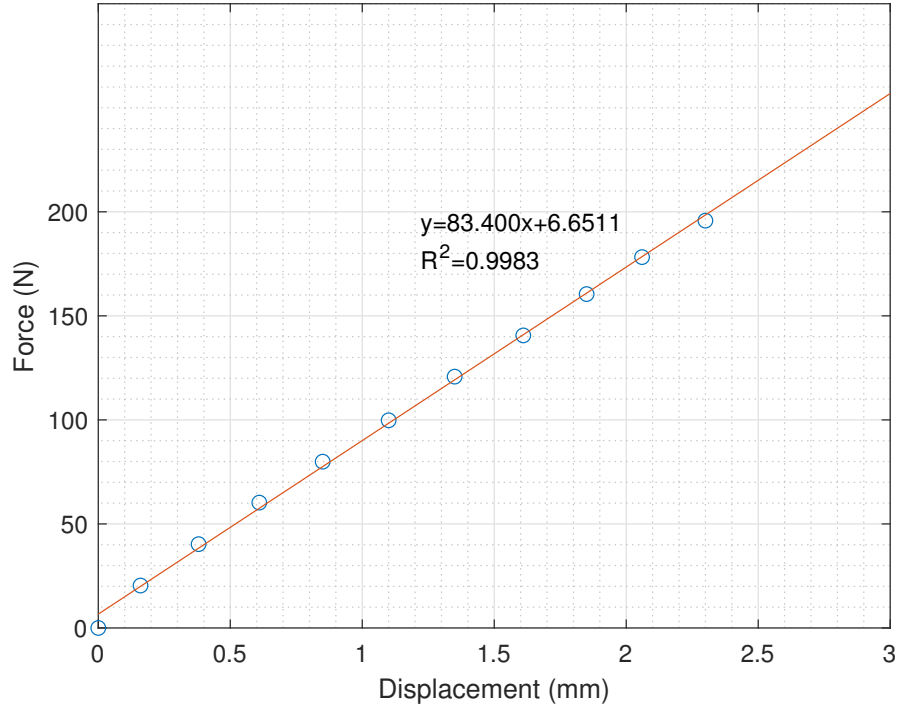


Figure 3.3: Flexural stiffness plot for the cylindrical tube

3.1.2 Renthal's Handlebar

An aluminum handlebar from the commercial brand Renthal was selected for the present work. The main characteristics of Renthal's handlebar are presented in the following.

Characteristics of the Renthal's Handlebar:

- Material: Aluminum 7050 T6 [Bike24, 2022]
- Clamp diameter: 31.8 mm [R2-bike, 2022]
- Width: 800 mm [R2-bike, 2022]
- Rise: 20 mm [R2-bike, 2022]
- Backsweep: 7° [R2-bike, 2022]
- Upsweep: 5° [R2-bike, 2022]
- Mass: 314 g [R2-bike, 2022]

Figure 3.4 shows the setup of the stiffness tests for all handlebars.

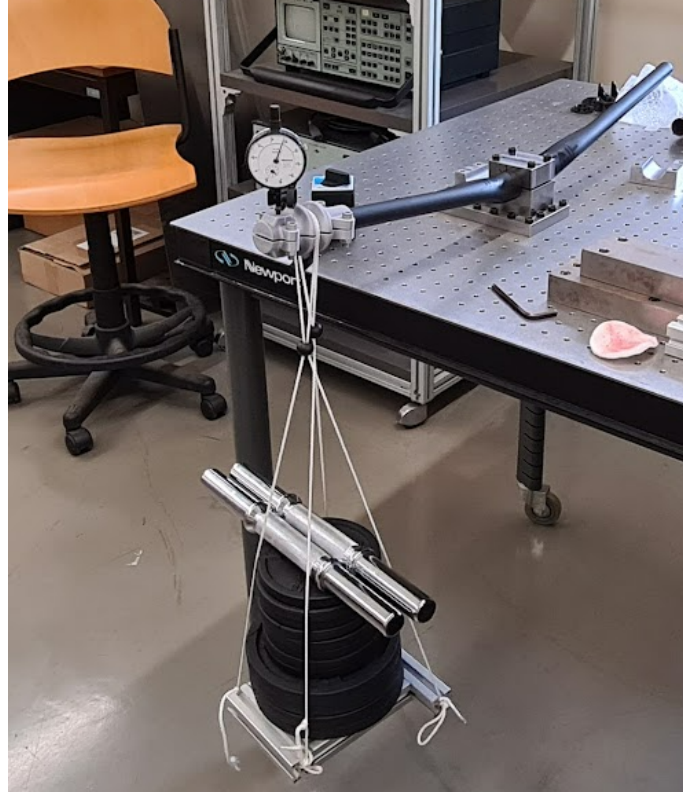
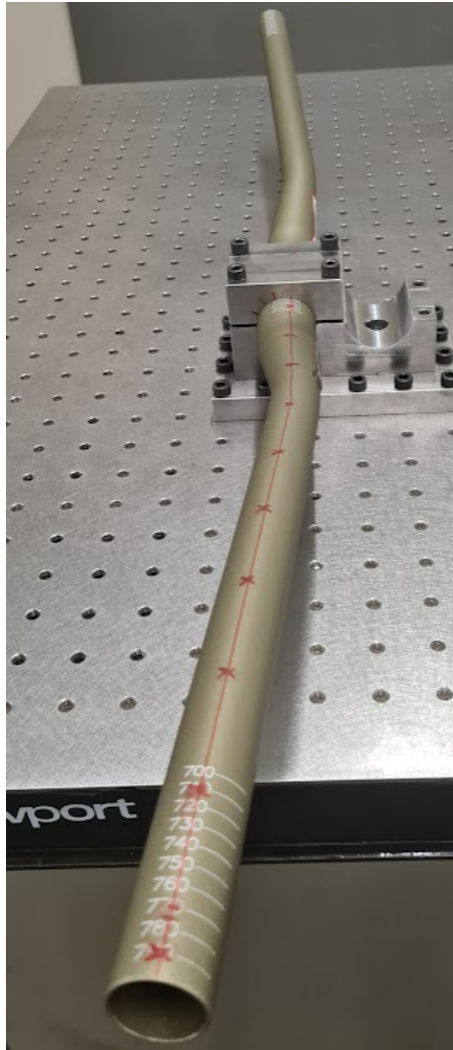
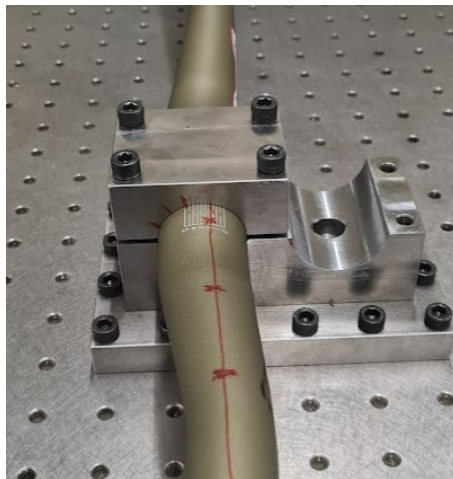


Figure 3.4: Setup of the stiffness tests for all handlebars

As can be seen in Figure 3.4, the handlebar was clamped in the middle. The vertical load was applied at 50 mm from the end of the handlebar according to the ISO 4210-5:2014 - Lateral bending test. The displacement was measured at 15 mm from the end of the handlebar with a dial indicator. This procedure was repeated for three different positions of the handlebars. In Figures 3.5, 3.6 and 3.7, it is possible to see the three riding positions of the Renthal's handlebar. Position 1 corresponds to the reference position of the handlebar, and Positions 2 and 3 correspond to rotated configurations for simulating different riding positions depending on the rider's static comfort.

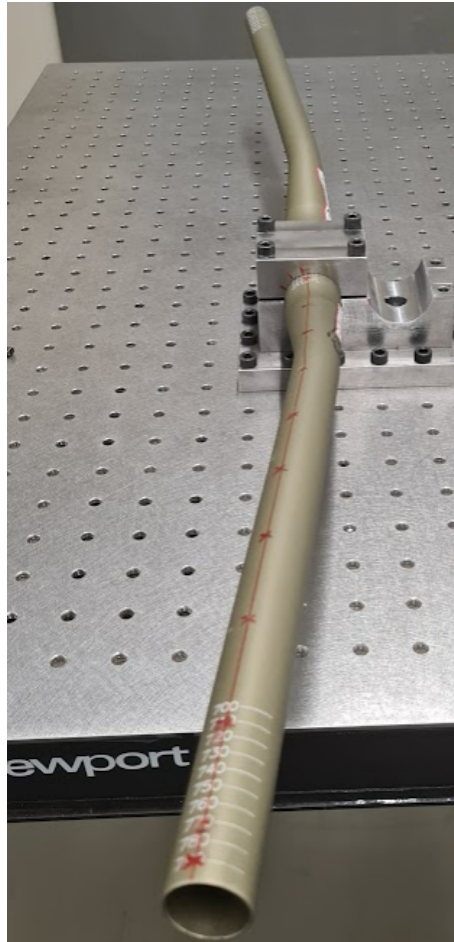


(a) Overview

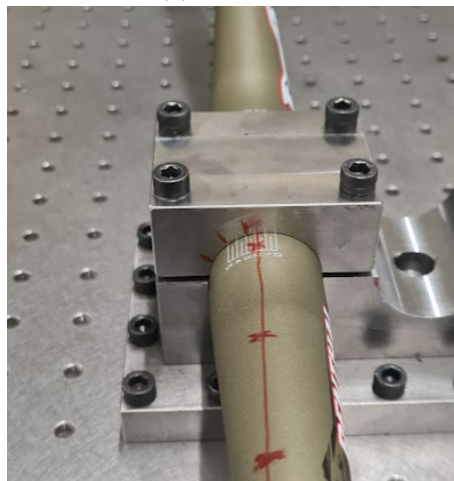


(b) Detailed view of the fixture support

Figure 3.5: Renthal's handlebar - Position 1



(a) Overview

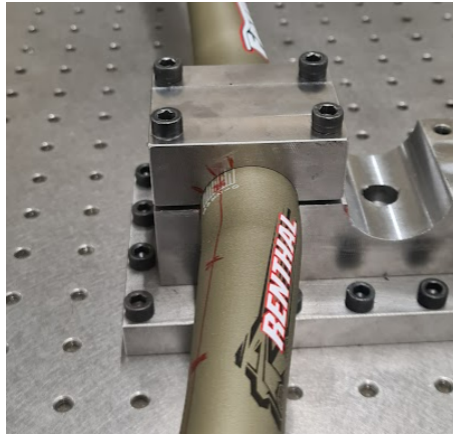


(b) Detailed view of the fixture support

Figure 3.6: Renthal's handlebar - Position 2



(a) Overview



(b) Detailed view of the fixture support

Figure 3.7: Renthal's handlebar - Position 3

Table 3.2 presents the displacements obtained for the different loading conditions. The weights were loaded in the same order to ease the comparison.

Table 3.2: Displacement recording for Renthal's handlebar at different positions

Load (N)	Displacement (mm)		
	Position 1	Position 2	Position 3
0	0	0	0
20.39	0.38	0.42	0.42
40.28	0.81	0.87	0.90
60.25	1.27	1.32	1.31
79.92	1.72	1.75	1.74
99.80	2.19	2.19	2.09
120.79	2.66	2.67	2.57
140.60	3.13	3.11	3.00
160.46	3.58	3.56	3.40
178.23	3.89	3.89	3.80
195.76	4.05	4.31	4.01

In Figure 3.8, it is possible to examine the flexural stiffness plot for all three positions of Renthal's handlebar.

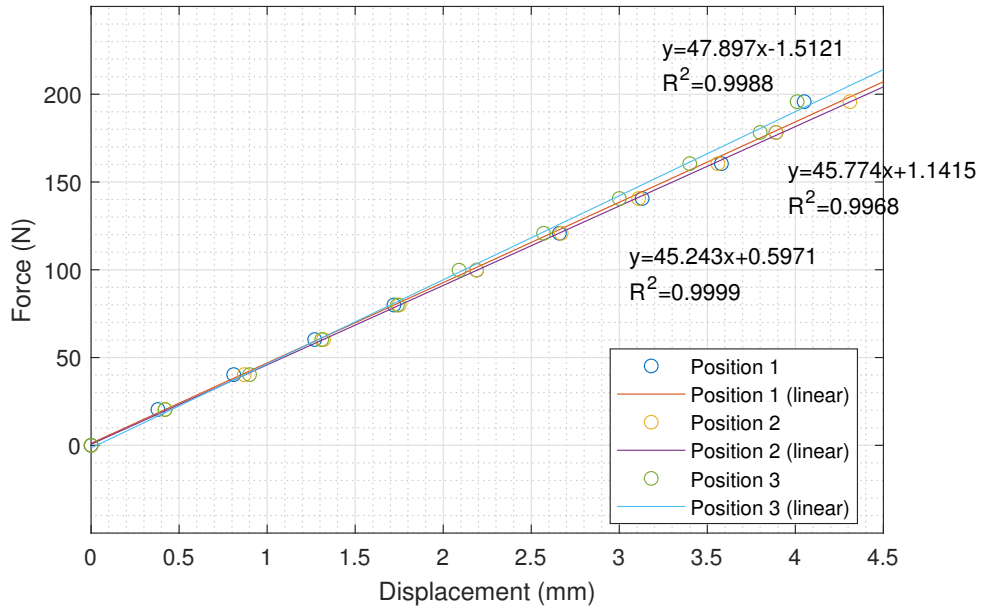


Figure 3.8: Flexural stiffness plot for the Renthal's handlebar

As can be seen, Position 3 is the one presenting higher flexural stiffness - 47.897 N/mm. The flexural stiffness of the handlebar is similar in Positions 1 and 2 - 45.773 N/mm and 45.243 N/mm, respectively. As expected, Renthal's handlebar has a lower flexural stiffness when compared to the cylindrical tube.

3.1.3 OneUp's Handlebar

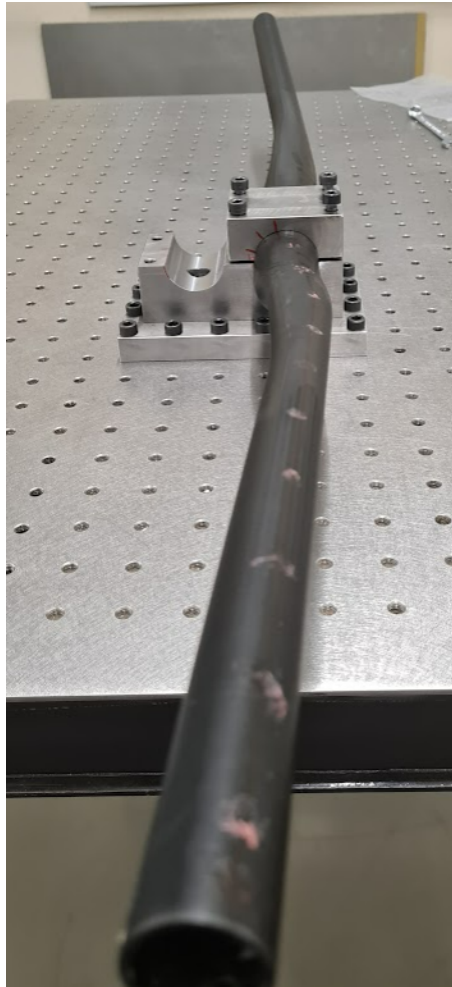
A carbon fiber composite handlebar from the commercial brand OneUp was selected for the present work. The main characteristics of OneUp's handlebar are presented in the

following.

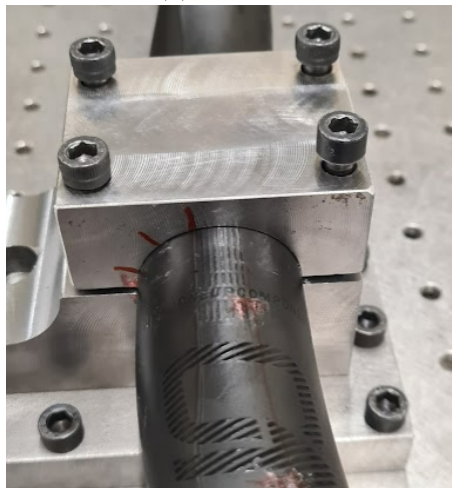
Characteristics of the OneUp's Handlebar:

- Material: Carbon Fiber Composite [Bike-Components, 2022]
- Clamp diameter: 35 mm [Bike-Components, 2022]
- Width: 800 mm [Bike-Components, 2022]
- Rise: 20 mm [Bike-Components, 2022]
- Backsweep: 8° [Bike-Components, 2022]
- Upsweep: 5° [Bike-Components, 2022]
- Mass: 220 g [Bike-Components, 2022]

The setup of this stiffness test was the same one considered for the previous test. The procedure was done three times again for three different positions. In Figures 3.9, 3.10 and 3.11, it is possible to see the three positions of the OneUp's handlebar.

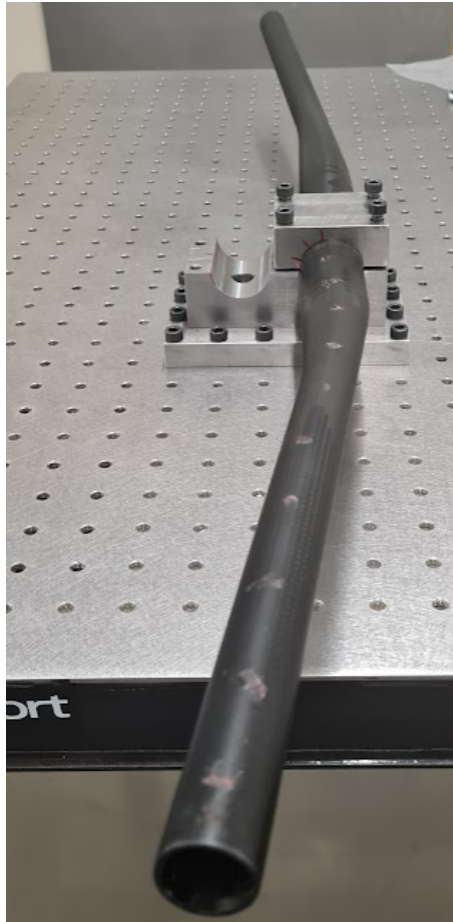


(a) Overview

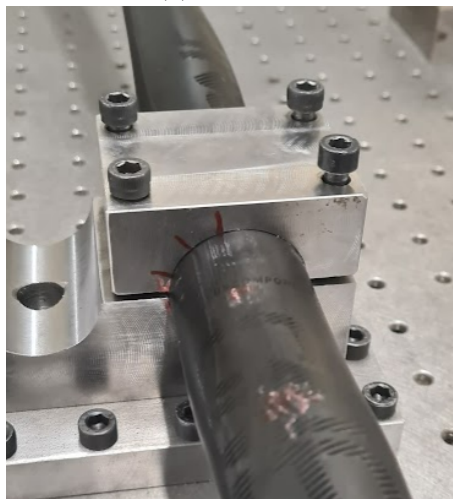


(b) Detailed view of the fixture support

Figure 3.9: OneUp's handlebar - Position 1



(a) Overview

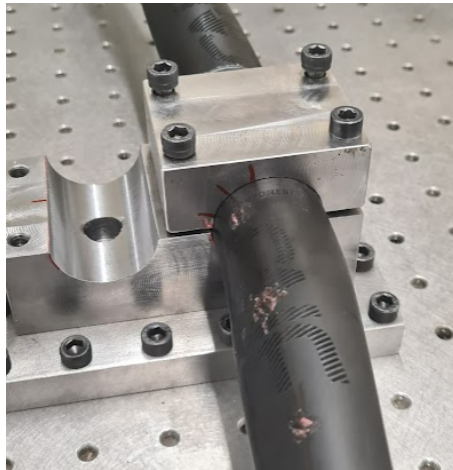


(b) Detailed view of the fixture support

Figure 3.10: OneUp's handlebar - Position 2



(a) Overview



(b) Detailed view of the fixture support

Figure 3.11: OneUp's handlebar - Position 3

Table 3.3 presents the displacements obtained for the different loading conditions. The weights were loaded in the same order to ease the comparison.

3. Experimental Tests

Table 3.3: Displacement recording for OneUp's handlebar at different positions

Load (N)	Displacement (mm)		
	Position 1	Position 2	Position 3
0	0	0	0
20.39	0.35	0.38	0.42
40.28	0.75	0.80	0.87
60.25	1.14	1.22	1.32
79.92	1.52	1.62	1.76
99.80	1.91	2.03	2.24
120.79	2.35	2.47	2.68
140.60	2.74	2.88	3.14
160.46	3.14	3.28	3.59
178.23	3.39	3.63	3.97
195.76	3.62	3.92	4.31

In Figure 3.12, it is possible to see the stiffness plot for all three positions of the OneUp's handlebar.

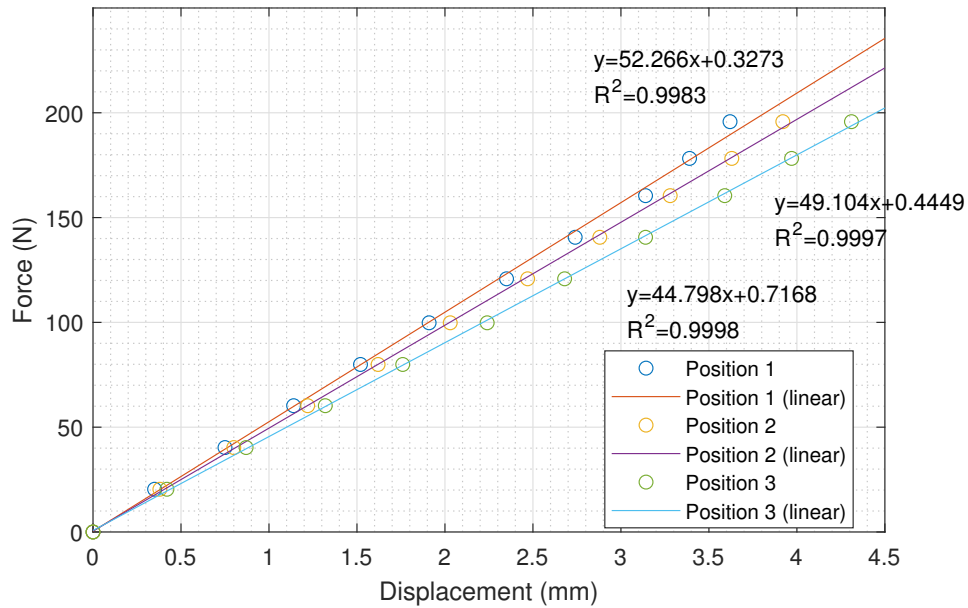


Figure 3.12: Flexural stiffness plot of OneUp's handlebar

As can be seen, Position 1 presents the highest flexural stiffness - 52.266 N/mm. In addition, the flexural stiffness of the handlebar in Position 2 is higher than in Position 3 - 49.104 N/mm and 44.798 N/mm, respectively. Comparing these results with the stiffness tests from Renthal's handlebar, the results follow the expected behavior. This handlebar is stiffer because it is made of a carbon fiber composite and has a clamp diameter of 35 mm, compared to the 31.8 from Renthal's handlebar. It is important to notice that with a lighter handlebar, it is possible to achieve higher stiffness due to the use of a carbon fiber composite and also the higher bar clamp diameter. Once again, this proves that carbon fiber composites have an excellent stiffness-to-weight ratio.

3.1.4 EC90 Handlebar

A carbon fiber composite handlebar with a clamp diameter of 31.8 mm from the commercial brand EC90 was selected for the present work. The main characteristics of the EC90's handlebar are presented in the following.

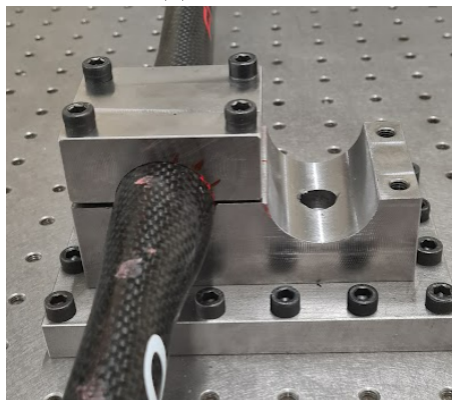
Characteristics of the EC90's Handlebar:

- Material: Carbon Fiber Composite [Amazon, 2022]
- Clamp diameter: 31.8 mm [Amazon, 2022]
- Width: 740 mm
- Rise: 0 mm (Flat bar)
- Backsweep: 0°
- Upsweep: 2.5°
- Mass: 131 g

The setup of this stiffness test was the same one considered for the previous tests. The procedure was done three times again for three different positions. In Figures 3.13, 3.14, and 3.15, it is possible to see the three positions of the EC90's handlebar.



(a) Overview



(b) Detailed view of the fixture support

Figure 3.13: EC90's handlebar - Position 1



(a) Overview



(b) Detailed view of the fixture support

Figure 3.14: EC90's handlebar - Position 2



(a) Overview



(b) Detailed view of the fixture support

Figure 3.15: EC90's handlebar - Position 3

Table 3.4 presents the displacements obtained for the different loading conditions. The weights were loaded in the same order to ease the comparison.

Table 3.4: Displacement recording for EC90's handlebar at different positions

Load (N)	Displacement (mm)		
	Position 1	Position 2	Position 3
0	0	0	0
20.39	0.45	0.41	0.44
40.28	0.90	0.88	0.92
60.25	1.34	1.32	1.38
79.92	1.79	1.79	1.84
99.80	2.30	2.29	2.35
120.79	2.76	2.76	2.80
140.60	3.23	3.23	3.31
160.46	3.72	3.75	3.77
178.23	4.14	4.14	4.20
195.76	4.56	4.56	4.43

Figure 3.16 shows the flexural stiffness plot for all three positions of the EC90 handlebar.

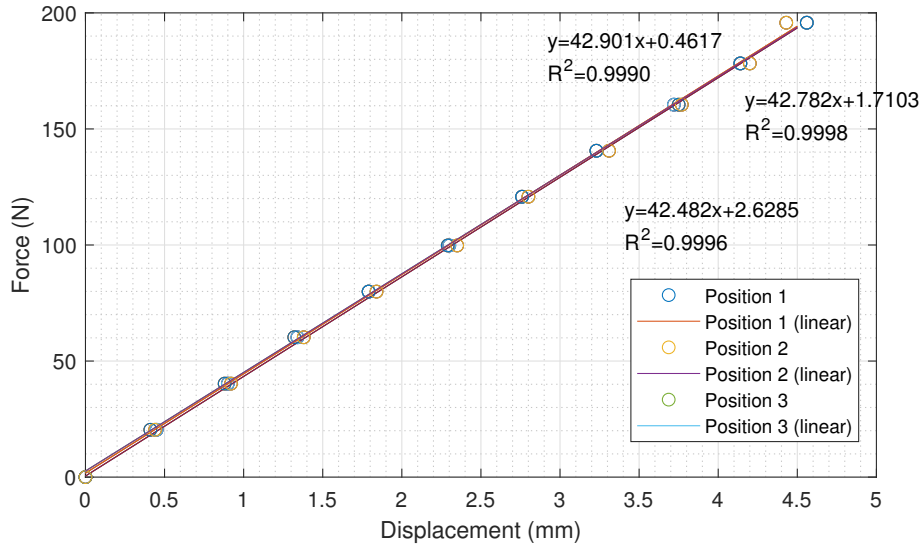


Figure 3.16: Flexural stiffness plot of EC90's handlebar

From Figure 3.16, it is possible to notice similar flexural stiffnesses for all positions - around 43 N/mm. This is because the handlebar is a flat handlebar, similar to a cylindrical tube. However, comparing these results with the tests from the Renthal and OneUp's handlebar, the flexural stiffness is much lower. Primarily, this can be explained due to the handlebar clamp diameter of 31,8 mm, although the length of the handlebar is also lower. So this shorter length increases stiffness, although it is not enough. Figure 3.17 presents a flexural stiffness plot of the four geometries to compare them easily.

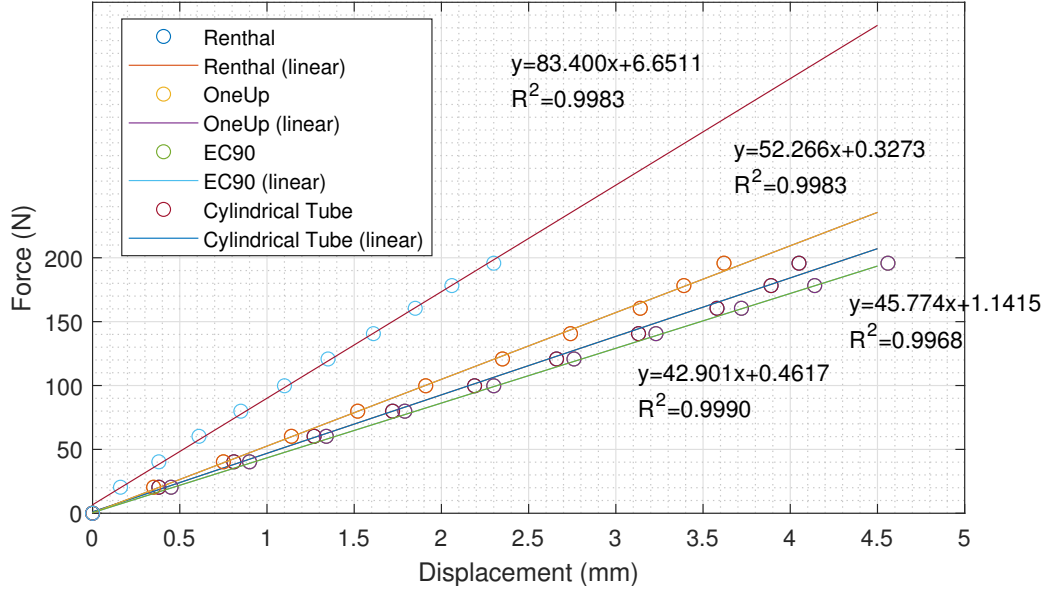


Figure 3.17: Flexural stiffness plot for all geometries

As expected, the cylindrical tube is much stiffer because of its 35 mm diameter along the length. After that, the OneUp's handlebar is the stiffer one due to its higher clamp diameter and carbon fiber composites. As mentioned before, between the Renthal's handlebar and EC90's handlebar, the Renthal's handlebar is also stiffer.

3.2 Experimental Modal Analysis

After the stiffness tests, the experimental modal analyses with the Impact Hammer Technique were performed for the cylindrical aluminum tube of 400 mm in length like in the stiffness test, for the cylindrical tube with double the length, and the three commercial handlebars. As presented before, this method consists of an impulse generated by an impact hammer as an input at a specific point and acceleration as an output at different measuring points. From the FRFs, it is possible to identify the natural frequencies, mode shapes, and damping ratios of the structure. It is important to notice that the frequency range used in all tests was from 0 to 3200 Hz. This way, it is possible to identify at least three modes for the handlebars and the smaller cylindrical tube. The resolution used was 0.5 Hz to obtain good results for dynamic tests, namely damping estimation.

3.2.1 Experimental Setup

The cylindrical tubes and commercial handlebars were clamped by a fixed support with a tightening torque of 5 N.m. The excitation force was given by an impact hammer (DYTRAN Instruments Model: 5800SL). Figure 3.18 shows the impact hammer used in the present work for the dynamic tests.



Figure 3.18: Impact hammer - DYTRAN Instruments 5800SL

An accelerometer (Endevco 27A11) was used to measure the acceleration response. For the FRF estimation, three samples were considered for every measuring point to have better and more consistent results. Figure 3.19 presents the setup for the tests.

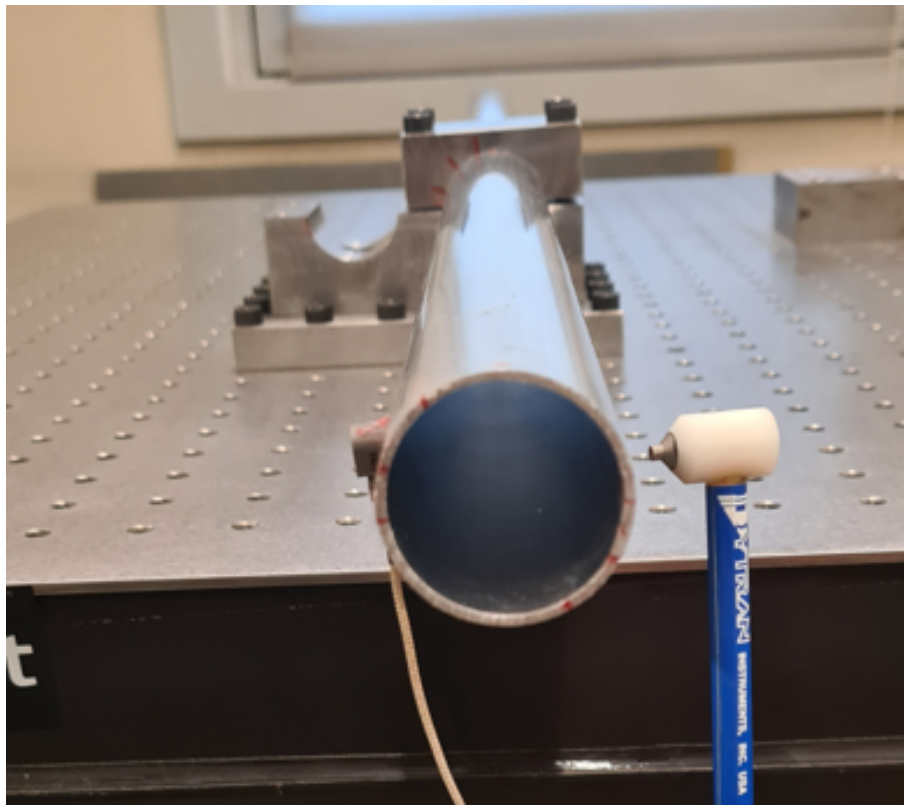


Figure 3.19: Experimental modal analysis setup

The impact point must be carefully selected. It is not the same in the different tests, and this will be addressed for each geometry. It must not be in a node or too near to it.

3. Experimental Tests

The chosen mesh in all structures was not regular, as it will be presented later for each test.

After the PULSE system detects the impact hammer hit, the portable data acquisition system (Brüel and Kjær, 2827-002) with a LAN interface connected to a PULSE software reads both force and acceleration signals, and the frequency response functions (FRFs) are generated. Figure 3.20 shows the portable data acquisition system.



Figure 3.20: Portable data acquisition system - Brüel and Kjær, 2827-002

A crucial piece of information concerning the transducers that must be correctly introduced in the software is their sensitivity. Table 3.5 presents the sensitivity of the impact hammer and accelerometer.

Table 3.5: Sensitivity of the transducers

Transducer	Sensitivity
Impact Hammer	23,7 mV/N
Accelerometer	9,859 mV/g

Figure 3.21 presents a diagram of the Impact Hammer Technique.

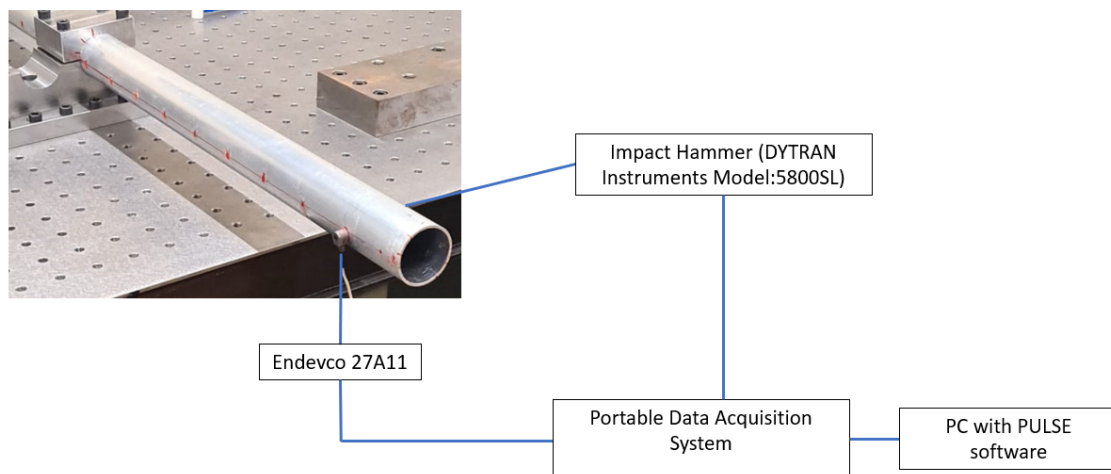
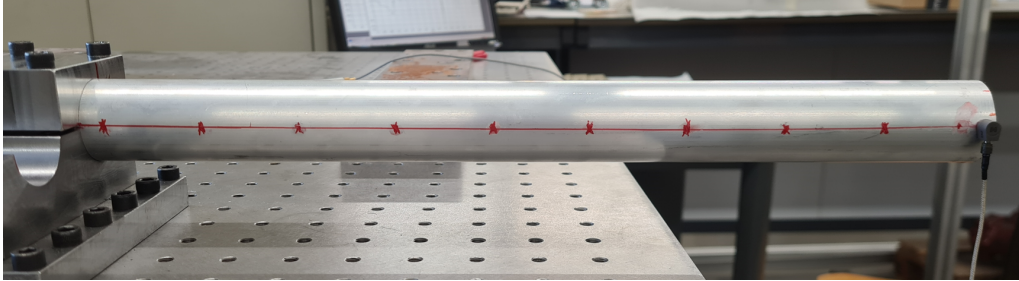


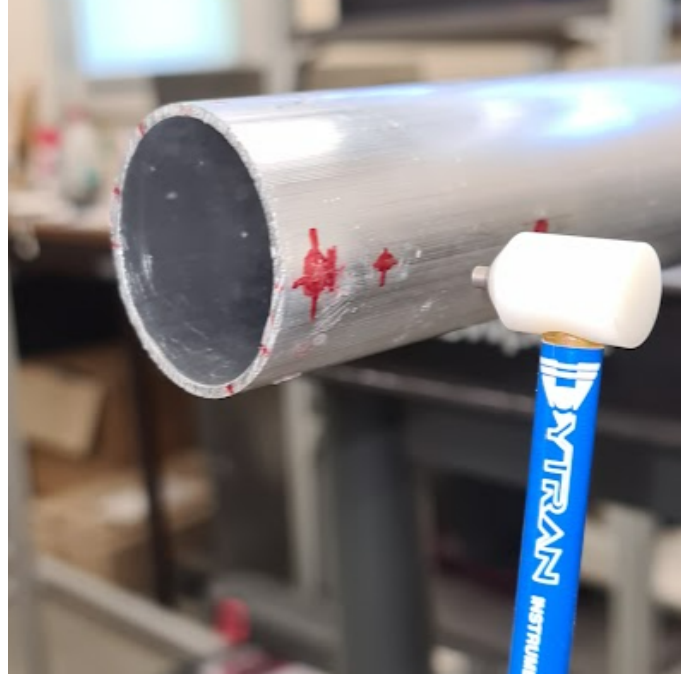
Figure 3.21: Diagram of the Impact Hammer Technique

3.2.2 Cylindrical Aluminum Tube (400mm)

The first experimental modal analysis was performed for the cylindrical tube for validation purposes. Figure 3.22 shows the ten measuring points and the impact point in the cylindrical tube considered for the experimental modal analysis.



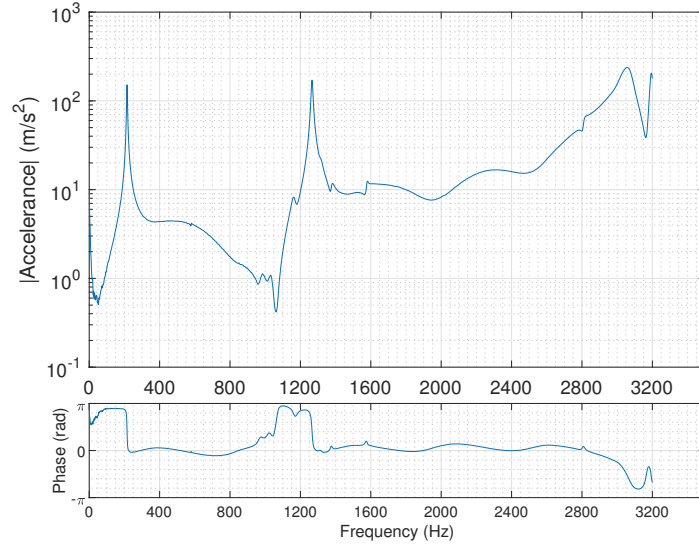
(a) Measuring points



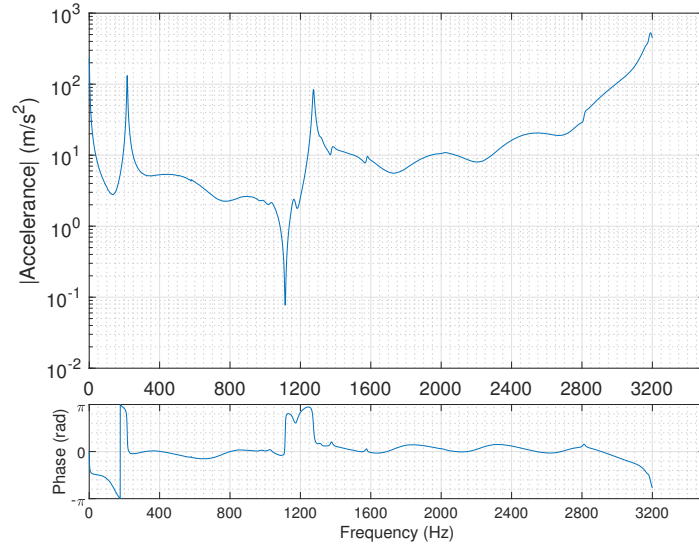
(b) Impact point

Figure 3.22: Cylindrical Tube (400mm) - Measuring and impact points for the EMA

The first point was 15 mm away from the end of the handlebar. The second point was spaced apart from the first one by 30 mm. The other points were equally spaced apart by 40 mm. The last point was 10 mm away from the fixed support. It is important to mention that the setup is exactly the same as in the stiffness tests with the clamped cylindrical tube. After the measurements, the results were analyzed in the commercial software ARTeMIS Modal. ARTeMIS uses two different methods to estimate and identify the modes: Complex Mode Identification Function (CMIF) and Rational Fractional Polynomial in Z-Domain (RFP-Z). Figure 3.23 shows the point FRF_{10,10} and a transfer FRF_{9,10}.



(a) Point FRF_{10,10}



(b) Transfer FRF_{9,10}

Figure 3.23: Point and transfer FRFs of the cylindrical tube (400 mm)

In the point FRF, it is possible to notice the classic behavior of a point FRF with an anti-resonance between the two resonances. It is possible to distinguish the first resonances of the 35 mm diameter cylindrical tube with 400 mm length. Those resonances are at frequencies of 214.9 and 1270.9 Hz. However, in these two FRFs, the third resonance is not identified. Ahead, it will be shown another transfer FRF where the third resonance can be easily identified. Figure 3.24 shows the coherence plot of both point and transfer FRFs.

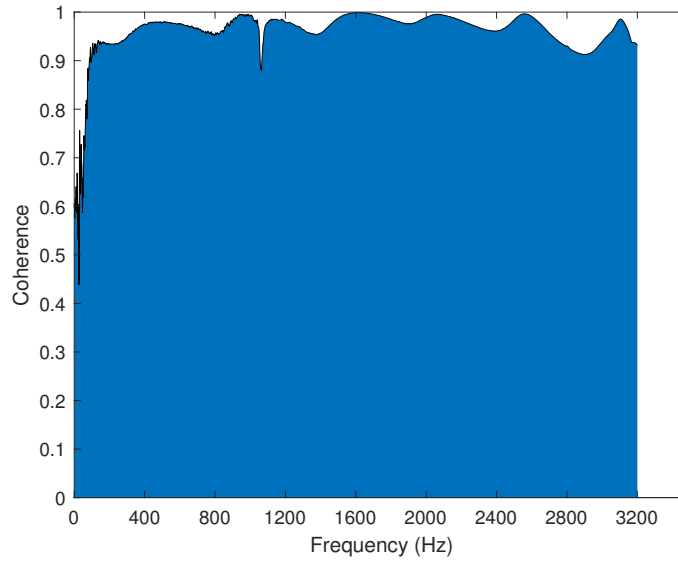
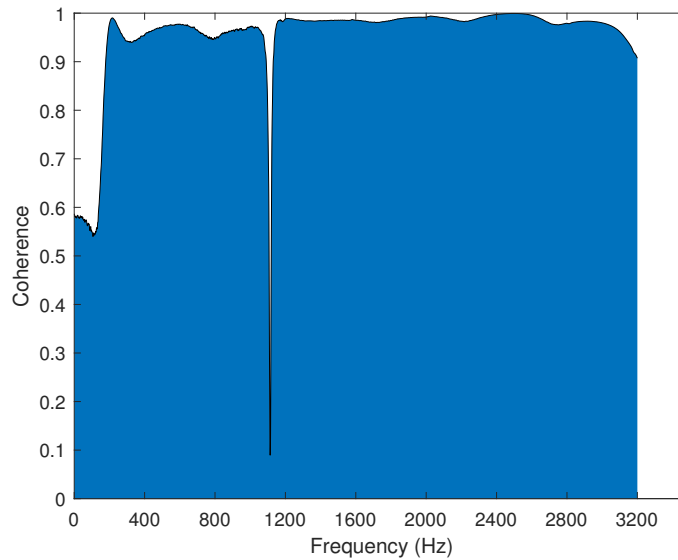
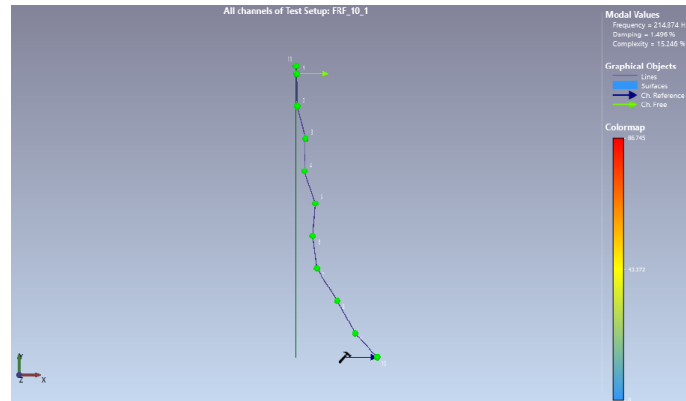
(a) Coherence of the point FRF_{10,10}(b) Coherence of the transfer FRF_{9,10}

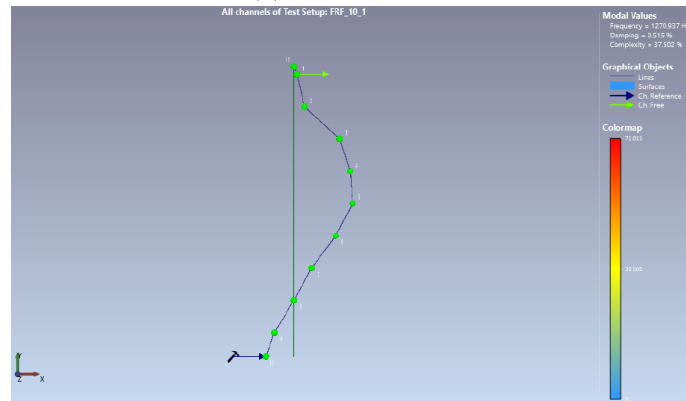
Figure 3.24: Coherence of the point and transfer FRFs of the cylindrical tube (400 mm)

The coherence indicates how much of the output is due to the input in the FRF. It can be seen as an indicator of the quality of the FRF. In the results for this cylindrical tube, the coherence at the anti-resonances is always worse. The reason for that is that at the anti-resonances, the stiffness of the structure is very high, and a slight deviation from the impact point affects the coherence. The coherence of both measurements is good, as can be seen in the coherence plot. Figure 3.25 presents the modes shapes obtained in the commercial software ARTEMIS.

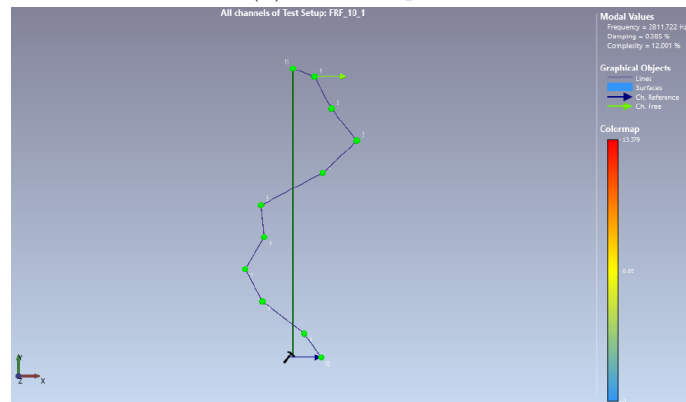
3. Experimental Tests



(a) Mode shape 1



(b) Mode shape 2



(c) Mode shape 3

Figure 3.25: Mode shapes of the cylindrical tube (400 mm)

The mode shapes presented are similar with the known mode shapes of fixed-free beam. Figure 3.26 shows the time response of the cylindrical tube for the same measuring points of the point FRF.

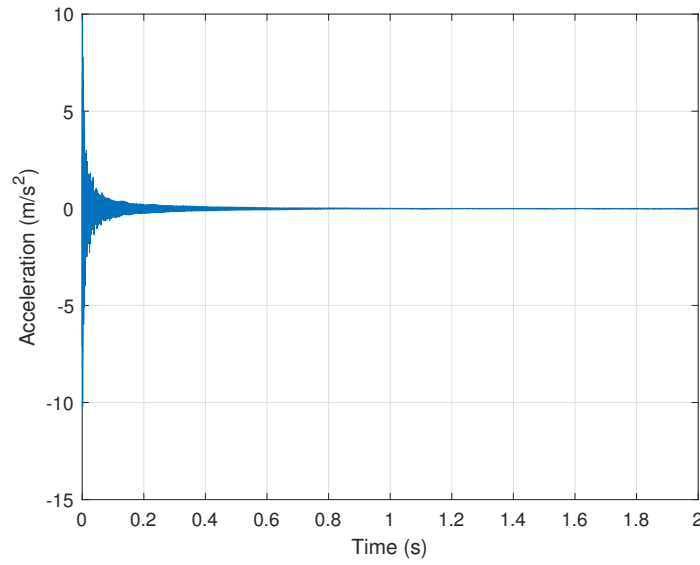


Figure 3.26: Time response for the measuring points of the point $\text{FRF}_{10,10}$ of the cylindrical tube (400 mm)

The time response follows the expected behavior. At first, the acceleration was higher due to the impact. As time goes by, the system tends to the static equilibrium position. After presenting all the results of the cylindrical tubes and handlebars, they will be compared with each other. Figure 3.27 shows another transfer $\text{FRF}_{7,10}$ where the third resonance is easily identified.

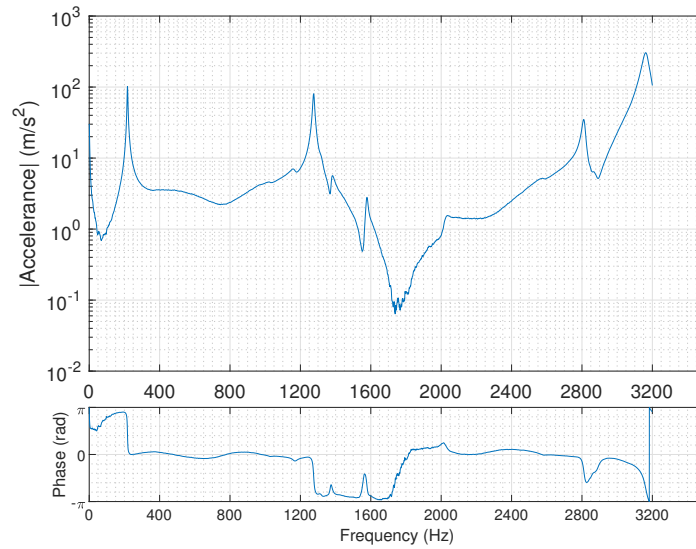


Figure 3.27: Transfer $\text{FRF}_{7,10}$ of the cylindrical tube (400 mm)

The natural frequency of the third mode is 2811.7 Hz. The coherence of this FRF is shown in Figure 3.28.

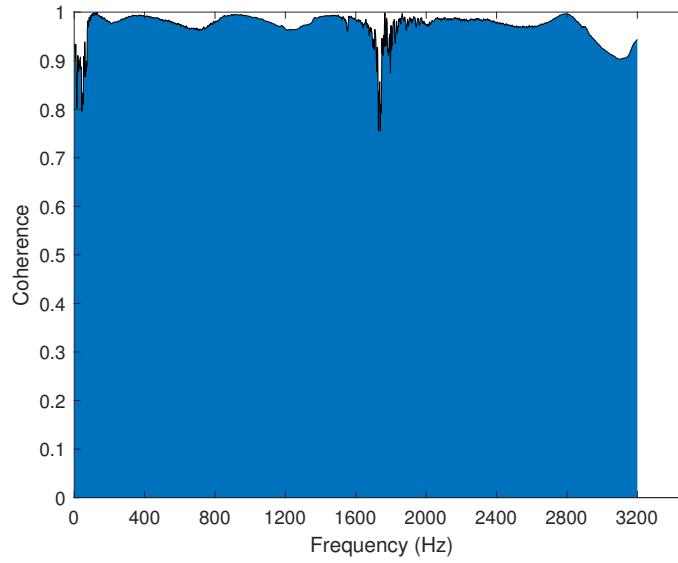


Figure 3.28: Coherence of the transfer $FRF_{7,10}$ of the cylindrical tube (400 mm)

The damping ratios of the first three modes were estimated using the circular curve fitting method. Table 3.6 presents the results considering a mean of every damping ratio for every FRF obtained in the experimental modal analysis for each mode of the cylindrical tube with 400 mm length.

Table 3.6: Natural frequencies and modal damping ratios of the cylindrical tube (400 mm)

	Mode 1	Mode 2	Mode 3
Natural frequency (Hz)	214.9	1270.9	2811.7
Damping ratio (%)	0.952	0.414	0.366

3.2.3 Cylindrical Aluminum Tube (775mm)

The second experimental modal analysis was performed for a longer cylindrical tube with 775mm, also for validation purposes. Figure 3.29 shows the ten measuring points considered in the cylindrical tube for the experimental modal analysis..

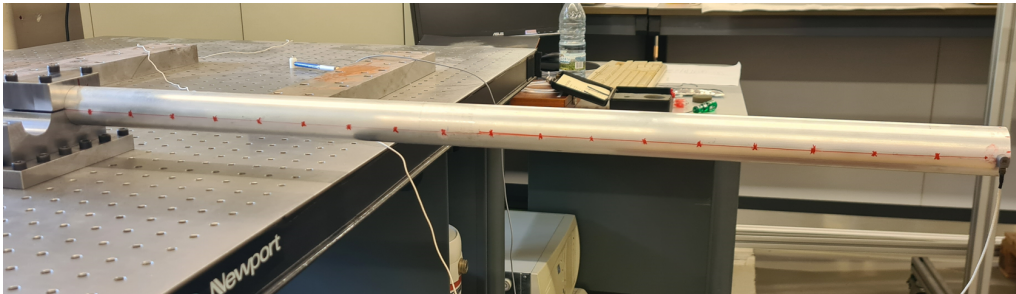


Figure 3.29: Cylindrical Tube (775mm) - Measuring and impact points for the EMA

The first point was 5 mm apart from the end of the handlebar. The second point was spaced by 40 mm from the first one. The remaining points were spaced apart by 80 mm.

The last point was 25 mm apart from the fixed support. The impact point was defined at 45 mm apart from the end of the handlebar on the opposing side from the second point. Once again, after the measurements, the results were analyzed in the commercial software ARTEMIS Modal. Figure 3.30 shows the point FRF_{9,9} and a transfer FRF_{10,9}.

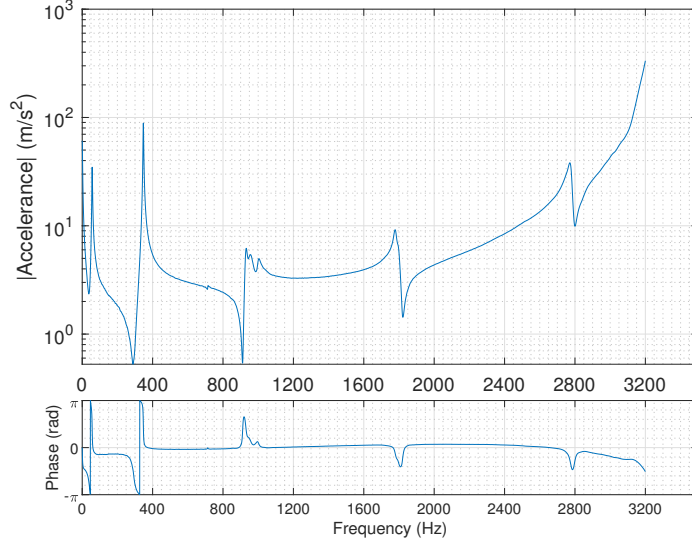
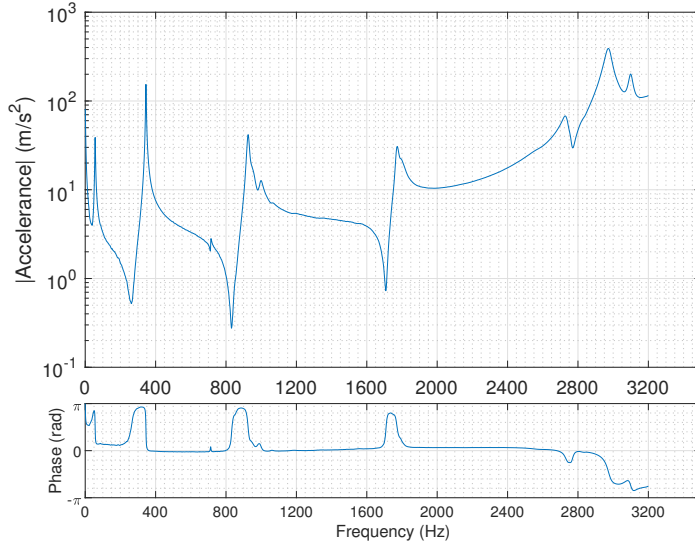
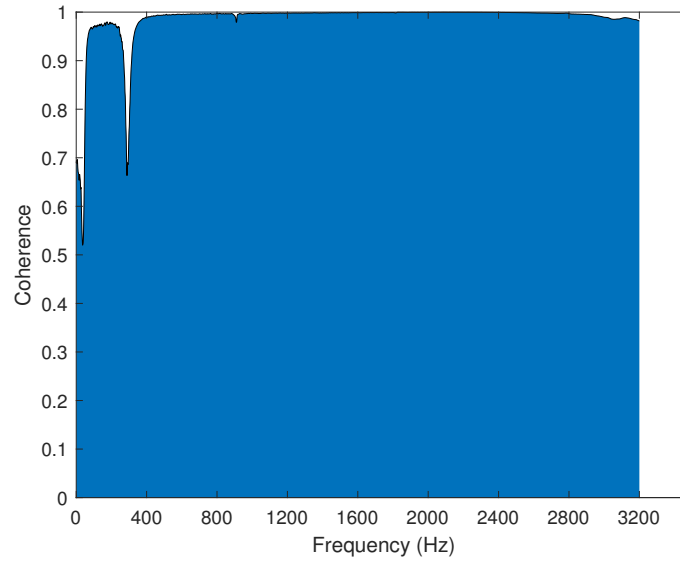
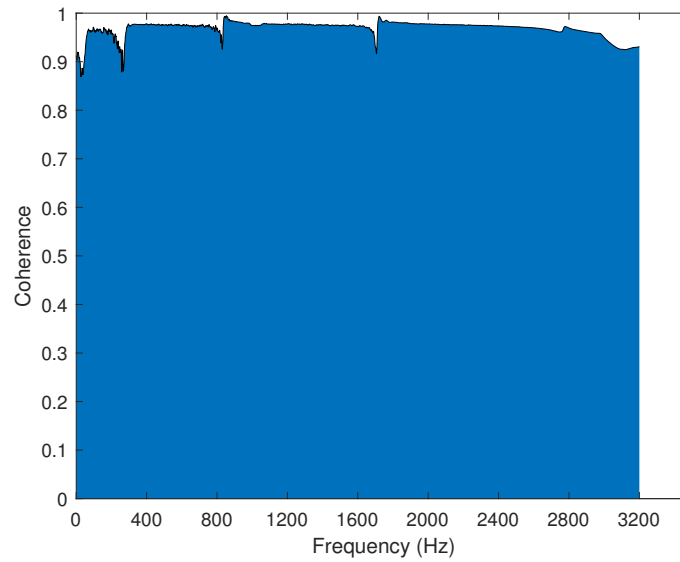
(a) Point FRF_{9,9}(b) Transfer FRF_{10,9}

Figure 3.30: Point and transfer FRFs of the cylindrical tube (775 mm)

In the point FRF, it is possible to notice the expected behavior of an FRF of this type with an anti-resonance between each pair of resonances. Considering the entire set of FRFs, it is possible to identify the first five modes of the 35 mm diameter cylindrical tube with a 775 mm length. The corresponding natural frequencies are 56.5, 346.6, 927.9, 1795.1, and 2769.5 Hz. Figure 3.31 shows the coherence plot of both point and transfer FRFs.



(a) Coherence of the point $\text{FRF}_{9,9}$



(b) Coherence of the transfer $\text{FRF}_{10,9}$

Figure 3.31: Coherence of the point and transfer FRFs of the cylindrical tube (775 mm)

Once more, the coherence of both measurements is good, as can be seen in Figure 3.31. As expected, the coherence in anti-resonances zones is a bit worse. Figure 3.32 presents the modes shapes obtained in the commercial software ARTeMIS.

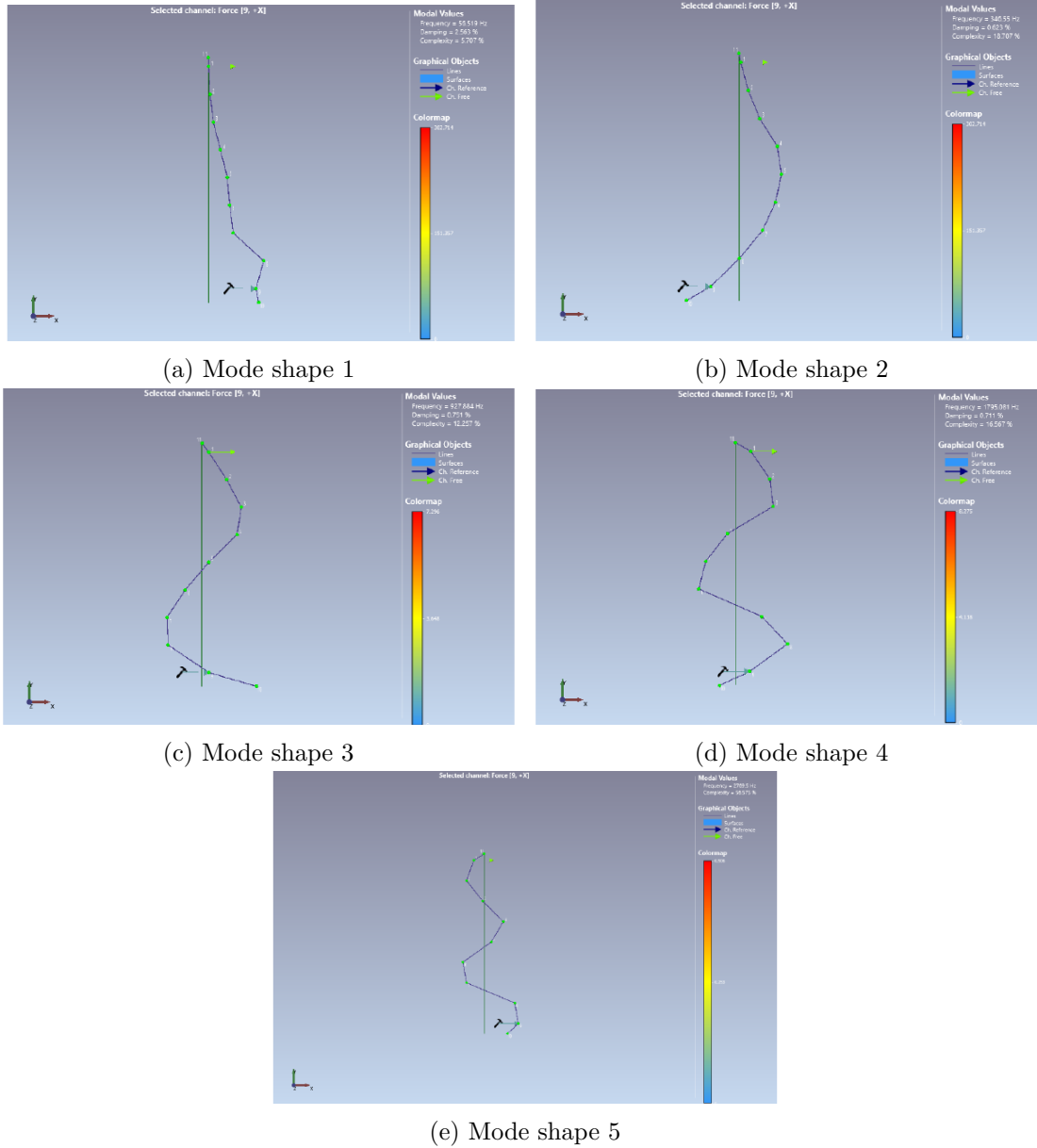


Figure 3.32: Mode shapes of the cylindrical tube (775 mm)

The mode shapes presented are very similar with the known mode shapes of fixed-free beam. Figure 3.33 shows the time response of the cylindrical tube for the same measuring points of the point FRF_{9,9}.

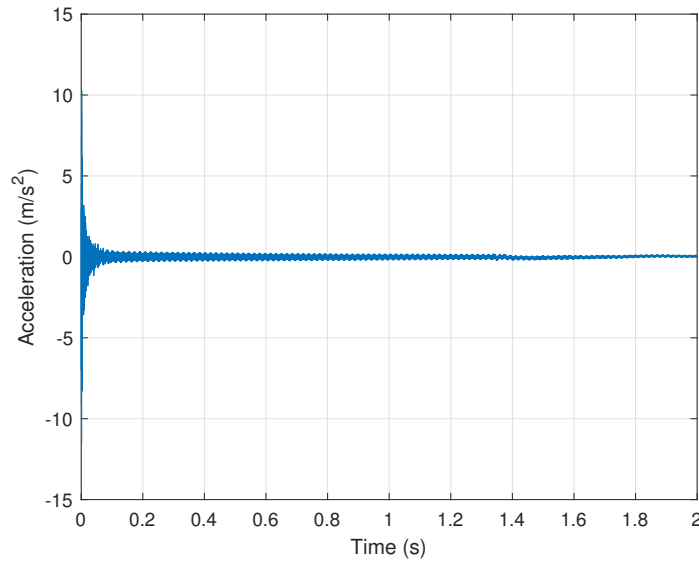


Figure 3.33: Time response for the measuring points of the point FRF_{9,9} of the cylindrical tube (775 mm)

The time response follows the expected behavior. At first, the acceleration was higher due to the impact. As time goes by, the system tends to the static equilibrium position.

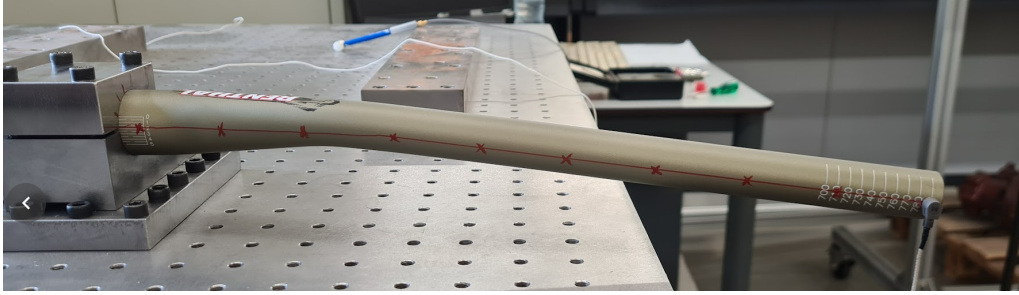
The damping ratios of the first five modes were estimated using the circular curve fitting method. Table 3.7 presents the results considering a mean of every damping for every FRF obtained in the experimental modal analysis for each mode of the cylindrical tube with 775 mm length.

Table 3.7: Natural frequencies and modal damping ratios of the cylindrical tube (775 mm)

	Mode 1	Mode 2	Mode 3	Mode 4	Mode 5
Natural Frequency (Hz)	56.5	346.6	927.9	1795.1	2769.5
Damping Ratio (%)	2.882	0.494	0.814	0.608	0.514

3.2.4 Renthal's Handlebar

The experimental modal analysis of the Renthal's handlebar was performed considering ten measuring points. Figure 3.34 shows the measuring and impact points.



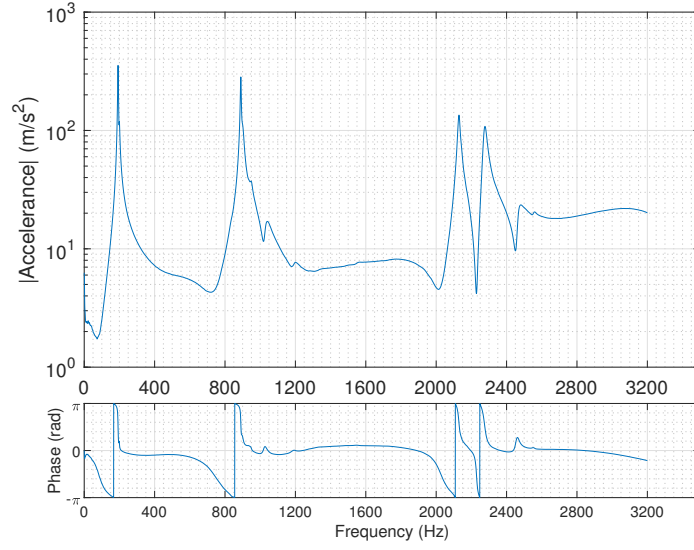
(a) Measuring points



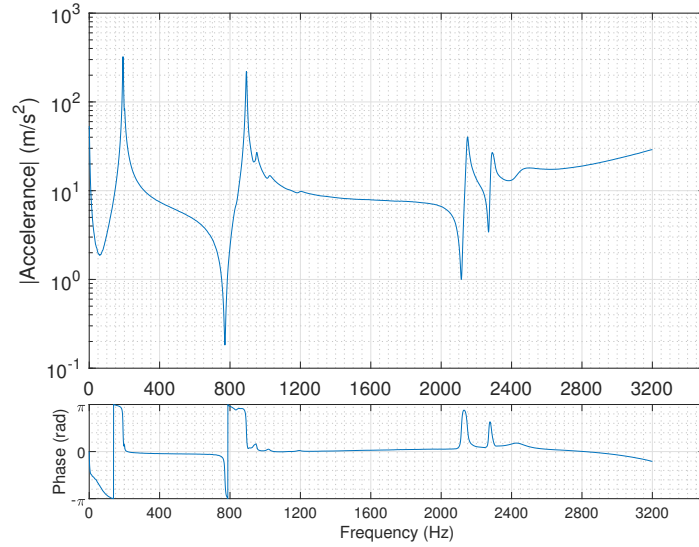
(b) Impact point

Figure 3.34: Measuring and impact points for the experimental modal analysis

The measuring direction is the same as in the stiffness tests with the handlebar in Position 1. The first measuring point is 15 mm apart from the end of the handlebar, and the second point is spaced 30 mm from the first one. The other ones were equally spaced apart by 40 mm. The last point is at 10 mm from the fixed support. The impact point is 15 mm apart from the end of the handlebar on the opposing side of the first measuring point. After all the measurements, the commercial software ARTEMIS was used to identify the modal parameters. Figure 3.35 shows the point FRF_{10,10} and the transfer FRF_{9,10}.



(a) Point FRF_{10,10}



(b) Transfer FRF_{9,10}

Figure 3.35: Point and transfer FRFs of Renthal's handlebar

In the point FRF, it is possible to notice the expected behavior of an FRF of this type with an anti-resonance between each pair of resonances. Considering the entire set of FRFs, it is possible to identify the first three modes of the Renthal's handlebar. The corresponding natural frequencies are 192.3, 891.0, and 2282.5 Hz. Figure 3.36 shows the coherence plot of both point and transfer FRFs.

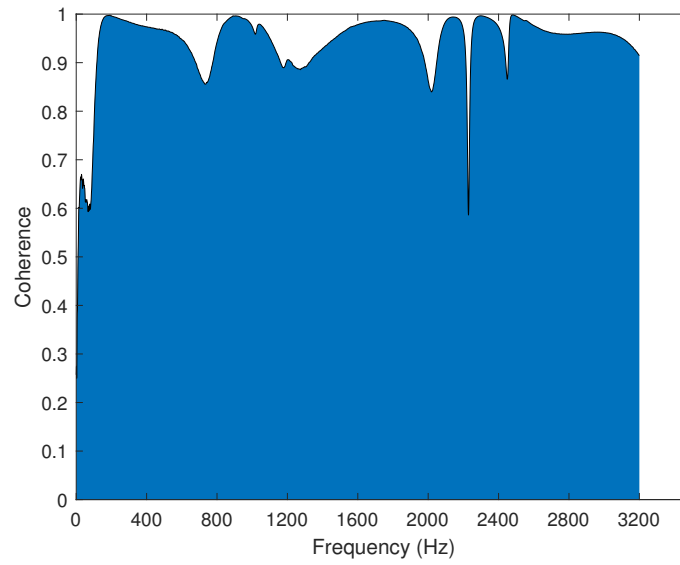
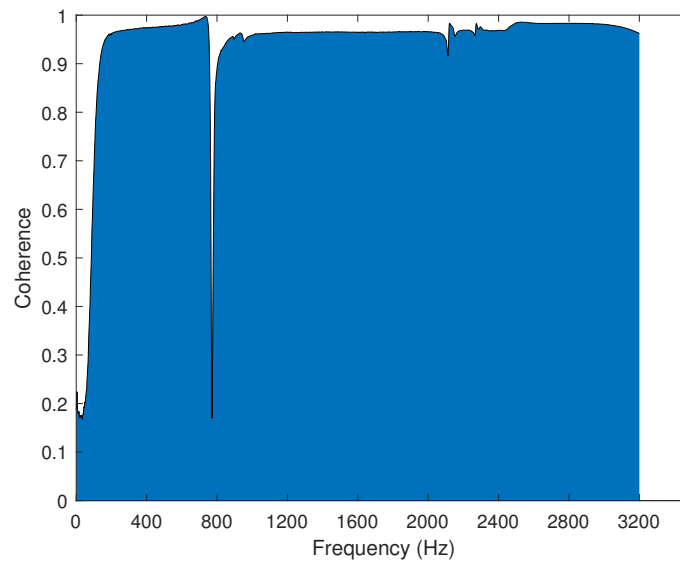
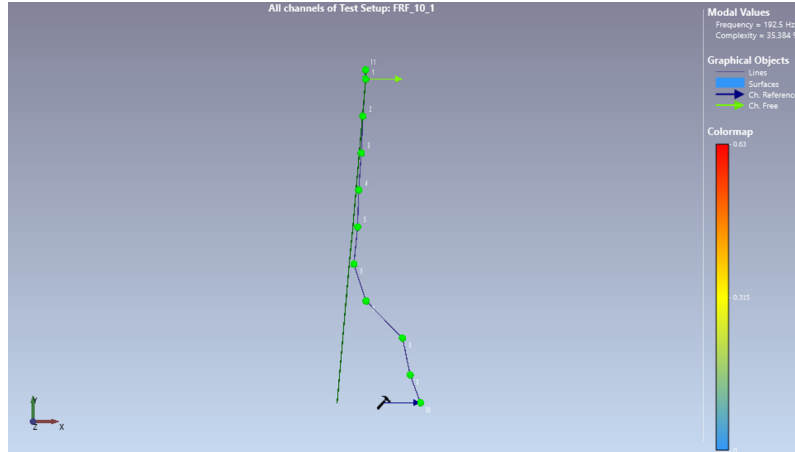
(a) Coherence of the point $\text{FRF}_{10,10}$ (b) Coherence of the transfer $\text{FRF}_{9,10}$

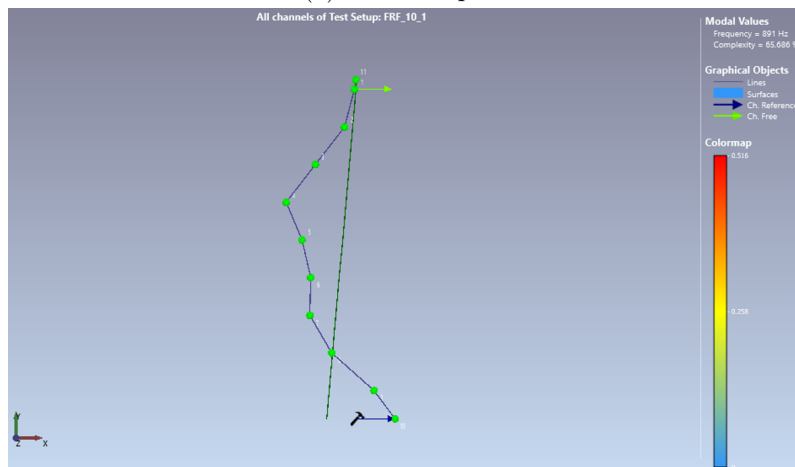
Figure 3.36: Coherence of the point and transfer FRFs of Renthal's handlebar

The coherence of both measurements is good, as can be seen in Figure 3.36. As already discussed, lower coherence in anti-resonance zones is expected. Figure 3.37 presents the modes shapes obtained in the commercial software ARTEMIS.

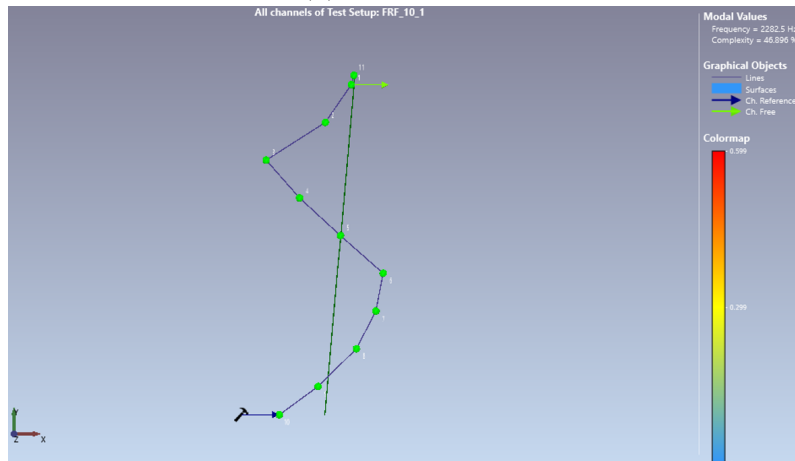
3. Experimental Tests



(a) Mode shape 1



(b) Mode shape 2



(c) Mode shape 3

Figure 3.37: Mode shapes of the Renthal's handlebar

The mode shapes presented are similar to the known mode shapes of a fixed-free beam. Figure 3.38 shows the time response of the handlebar for the same measuring points of the point FRF.

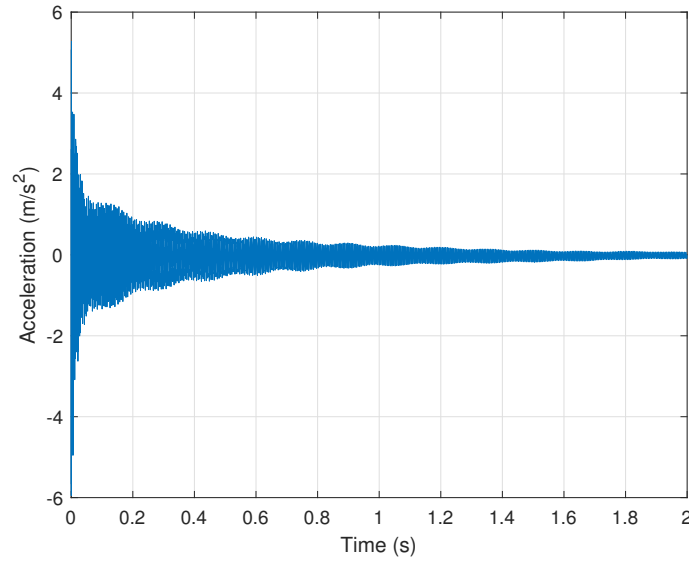


Figure 3.38: Time response for the measuring points of the point FRF_{10,10} of the Renthal's handlebar

The time response follows the expected behavior. At first, the acceleration was higher due to the impact. As time goes by, the system tends to the equilibrium position.

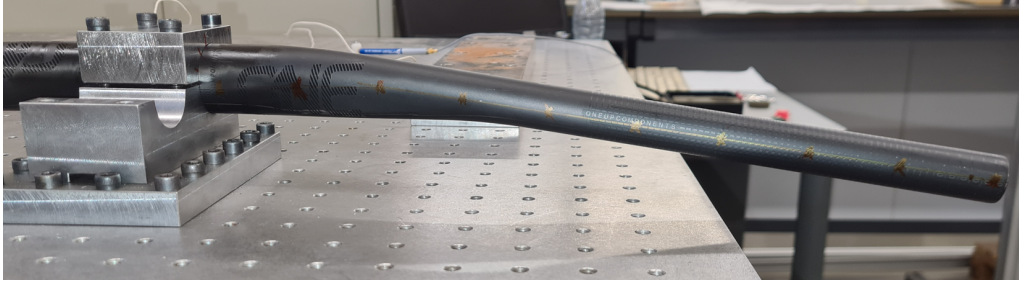
The damping ratios of the first three modes were estimated using the circular curve fitting method. Table 3.8 presents the results considering a mean of every damping for every FRF obtained in the experimental modal analysis for each mode of the Renthal's handlebar.

Table 3.8: Natural frequencies and modal damping ratios of the Renthal's handlebar

	Mode 1	Mode 2	Mode 3
Natural Frequency (Hz)	192.3	981.0	2285.5
Damping Ratio (%)	0.876	0.317	0.309

3.2.5 OneUp's Handlebar

Following the same procedure, the experimental modal analysis of the OneUp's handlebar was performed considering ten measuring points. Figure 3.39 shows the measuring and impact points.



(a) Measuring points



(b) Impact point

Figure 3.39: Measuring and impact points for the experimental modal analysis

The location of all measuring and impact points are the same as in the Renthal's handlebar since they have the same length. After all the measurements, the commercial software ARTEMIS was used to identify the modal parameters. The only difference here is the geometry created in ARTEMIS because the upsweep is 8° , contrary to the Renthal's handlebar, which is 7° . Figure 3.40 shows the point $FRF_{10,10}$ and the transfer $FRF_{9,10}$.

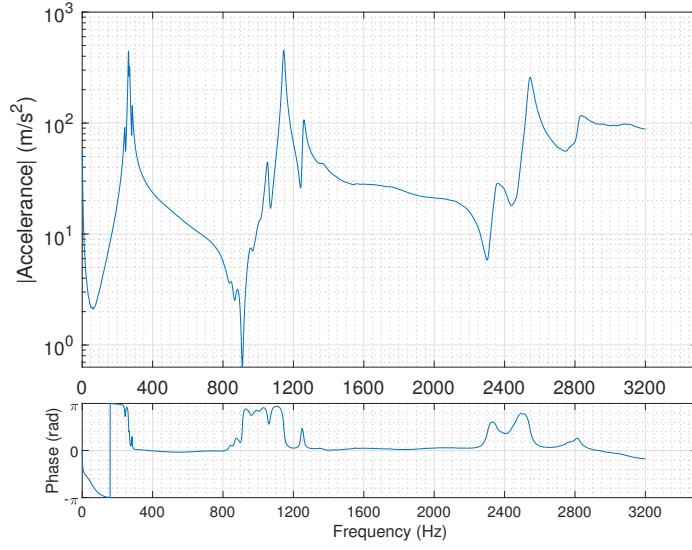
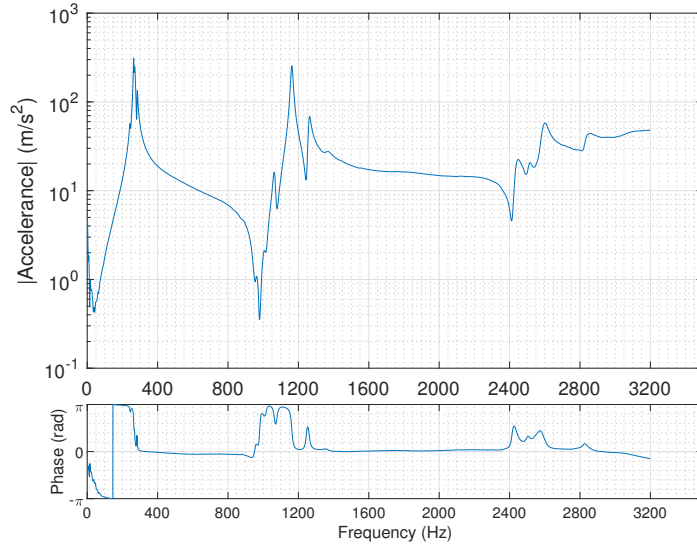
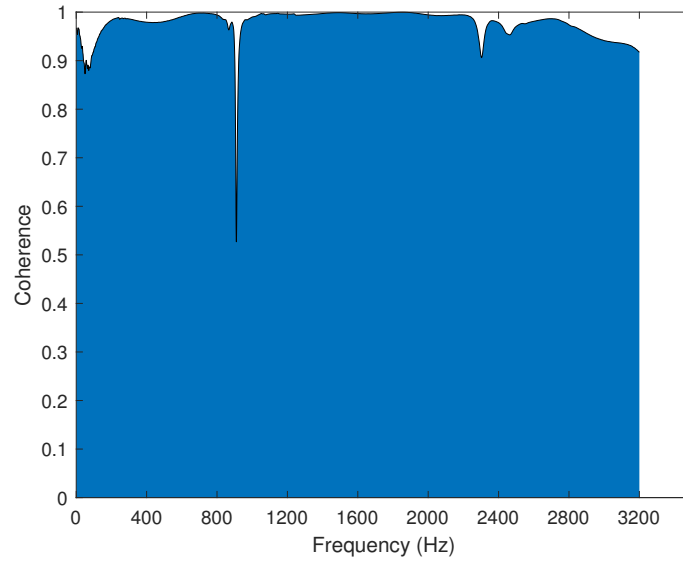
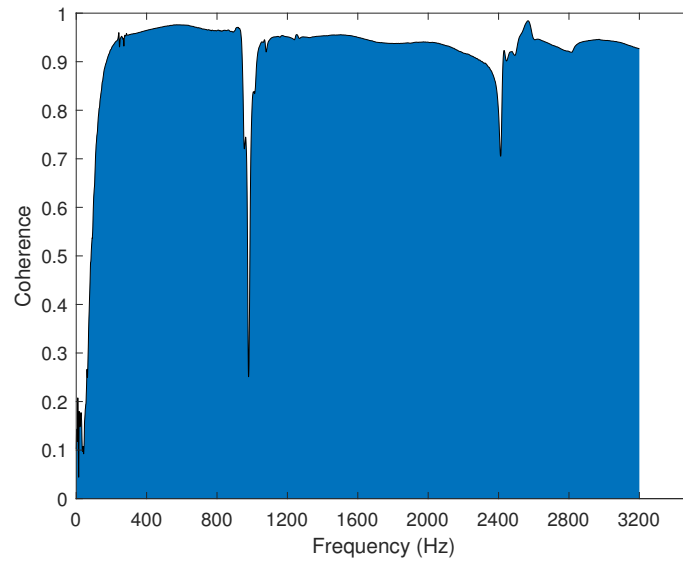
(a) Point FRF_{10,10}(b) Transfer FRF_{9,10}

Figure 3.40: Point and transfer FRFs of OneUp's handlebar

In the point FRF, it is possible to notice the expected behavior of an FRF of this type with an anti-resonance between each pair of resonances. Considering the entire set of FRFs, it is possible to identify the first three modes of the OneUp's handlebar. The corresponding natural frequencies are 263.5, 1265.5, and 2837.0 Hz. Figure 3.41 shows the coherence plot of both point and transfer FRFs.



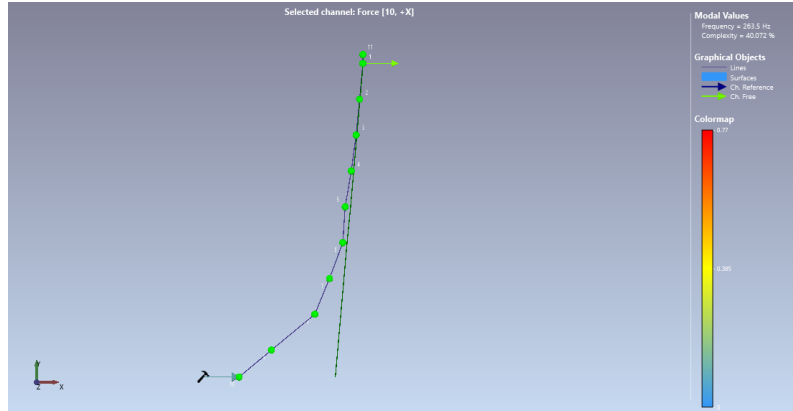
(a) Coherence of the point FRF_{10,10}



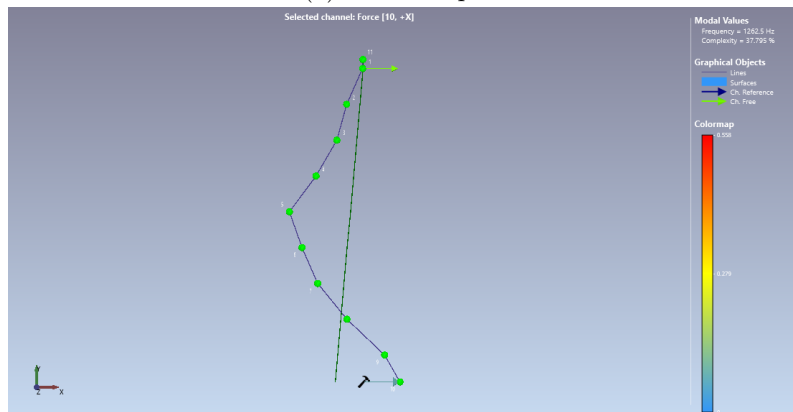
(b) Coherence of the transfer FRF_{9,10}

Figure 3.41: Coherence of the point and transfer FRFs of OneUp's handlebar

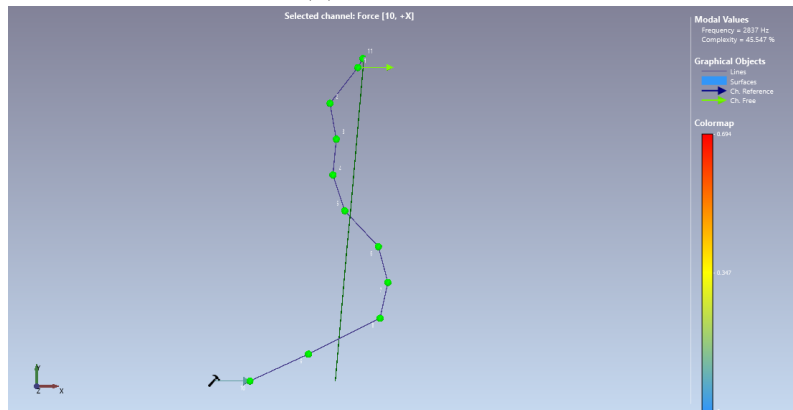
The coherence of both measurements is good, as can be seen in Figure 3.41. Once again, the coherence in anti-resonance zones is a bit worse. Figure 3.42 presents the modes shapes obtained in the commercial software ARTEMIS.



(a) Mode shape 1



(b) Mode shape 2



(c) Mode shape 3

Figure 3.42: Mode shapes of the OneUp's handlebar

The mode shapes presented are similar to the known mode shapes of a fixed-free beam. Figure 3.43 shows the time response of the handlebar for the same measuring points of the point FRF.

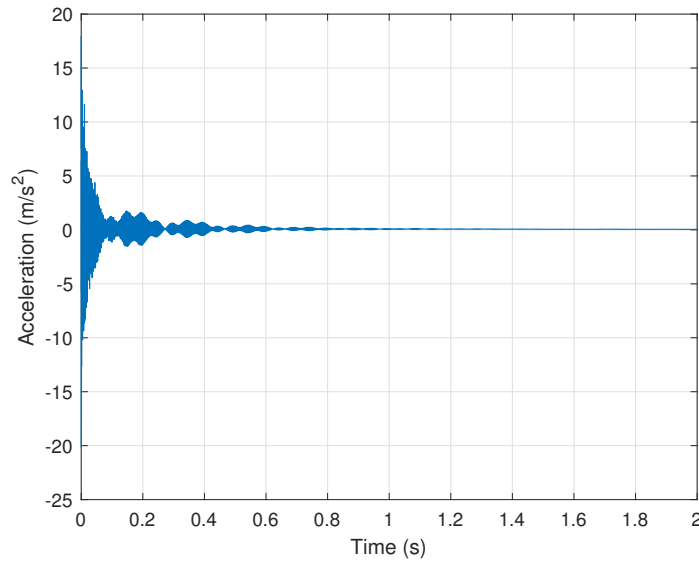


Figure 3.43: Time response for the measuring points of the point FRF_{10,10} of the OneUp's handlebar

The time response follows the expected behavior. At first, the acceleration was higher due to the impact. As time goes by, the system tends to the equilibrium position. However, it is possible to notice that different modes influence the free response of the handlebar when impacted at its end.

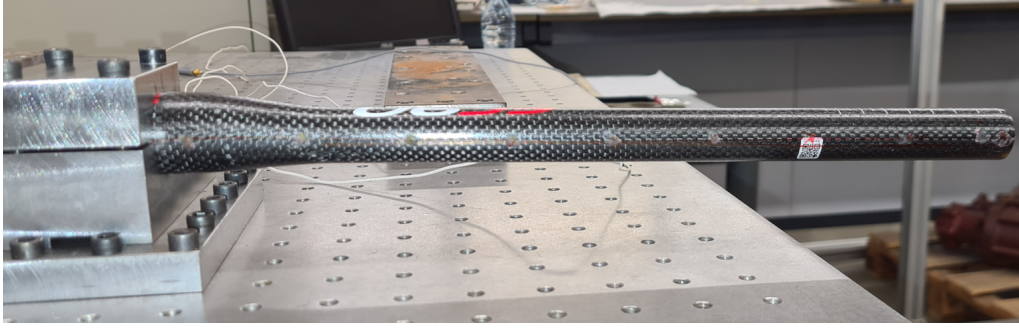
Once more, the damping ratios of the first three modes were estimated using the circular curve fitting method. Table 3.9 presents the results considering a mean of every damping for every FRF obtained in the experimental modal analysis for each mode of the OneUp's handlebar.

Table 3.9: Natural frequencies and modal damping ratios of the OneUp's handlebar

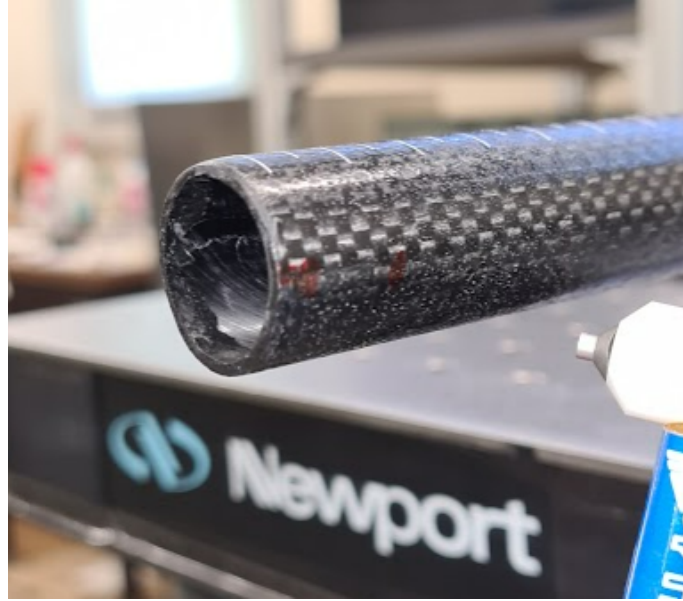
	Mode 1	Mode 2	Mode 3
Natural Frequency (Hz)	263,5	1265,5	2837,0
Damping Ratio (%)	0,745	0,641	0,827

3.2.6 EC90 Handlebar

The experimental modal analysis of the EC90's handlebar was performed considering nine measuring points. Figure 3.44 shows the measuring and impact points.



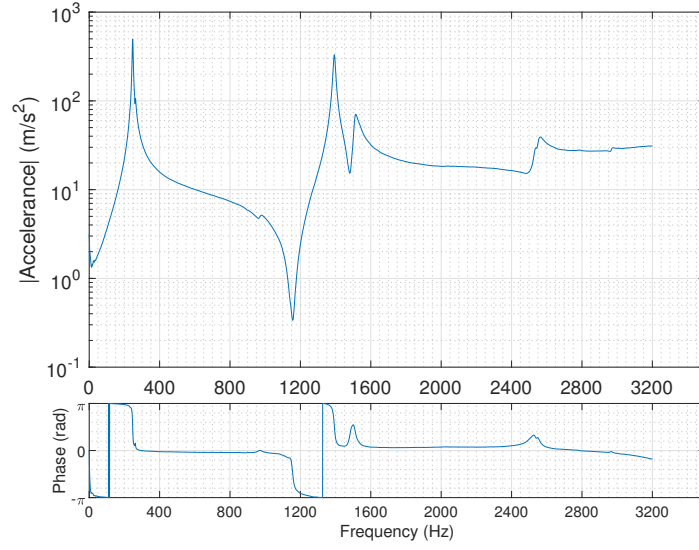
(a) Measuring points



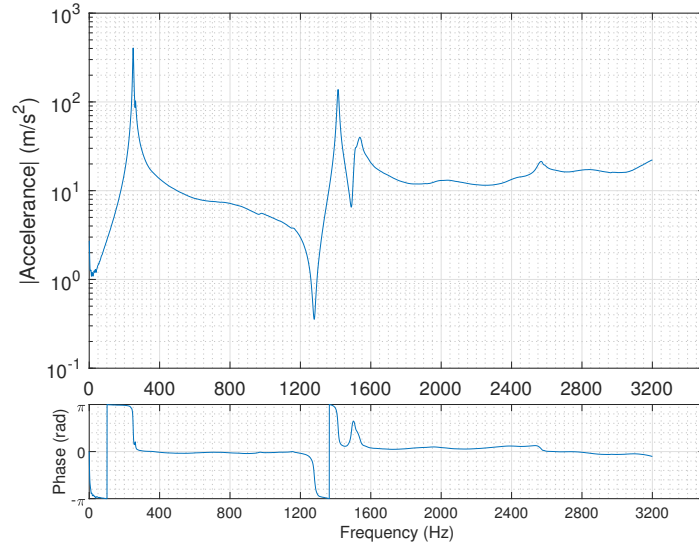
(b) Impact point

Figure 3.44: Measuring and impact points for the experimental modal analysis

The first measuring point is 15 mm apart from the end of the handlebar, and the second point is spaced 30 mm from the first one. The other ones were equally spaced apart by 40 mm. The last point is at 10 mm from the fixed support. The impact point is 15 mm apart from the end of the handlebar on the opposing side of the first measuring point. After all the measurements, the commercial software ARTEMIS was used to identify the modal parameters. Figure 3.45 shows the point FRF_{9,9} and the transfer FRF_{8,9}.



(a) Point FRF_{9,9}



(b) Transfer FRF_{8,9}

Figure 3.45: Point and transfer FRFs of EC90's handlebar

In the point FRF, it is possible to notice the expected behavior of an FRF of this type with an anti-resonance between each pair of resonances. Considering the entire set of FRFs, it is possible to identify the first three modes of the EC90's handlebar. The corresponding natural frequencies are 247.5, 1515.5, and 2556.5 Hz. Figure 3.46 shows the coherence plot of both point and transfer FRFs.

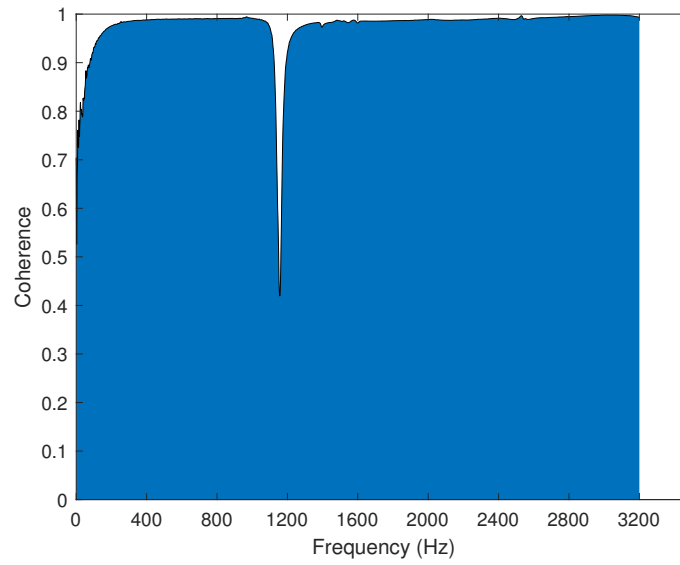
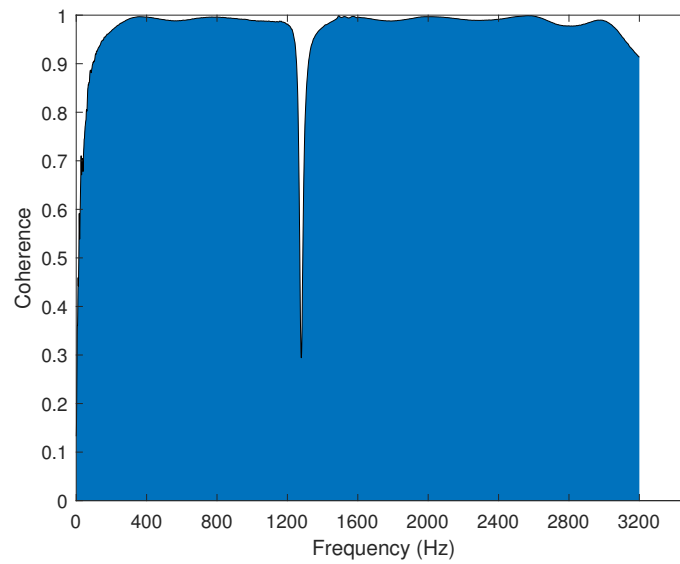
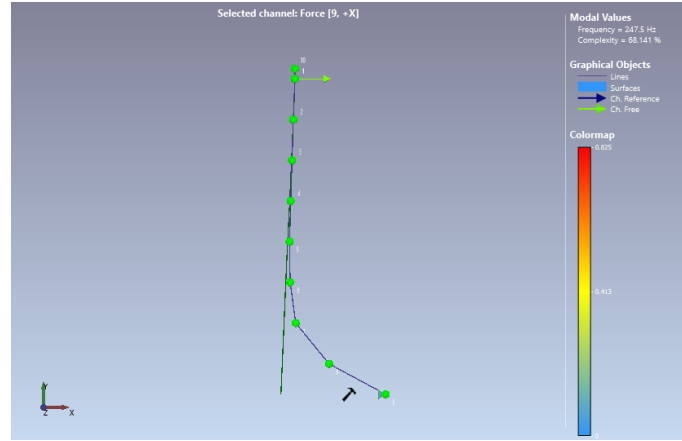
(a) Coherence of the point FRF_{9,9}(b) Coherence of the transfer FRF_{8,9}

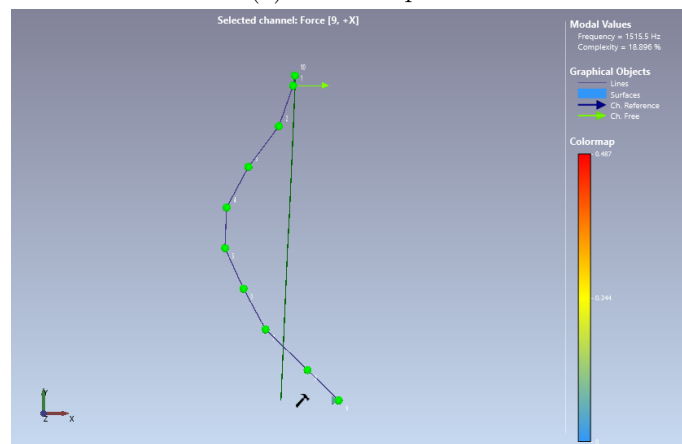
Figure 3.46: Coherence of the point and transfer FRFs of EC90's handlebar

The coherence of both measurements is good, as can be seen in Figure 3.46. Figure 3.47 presents the modes shapes obtained in the commercial software ARTeMIS.

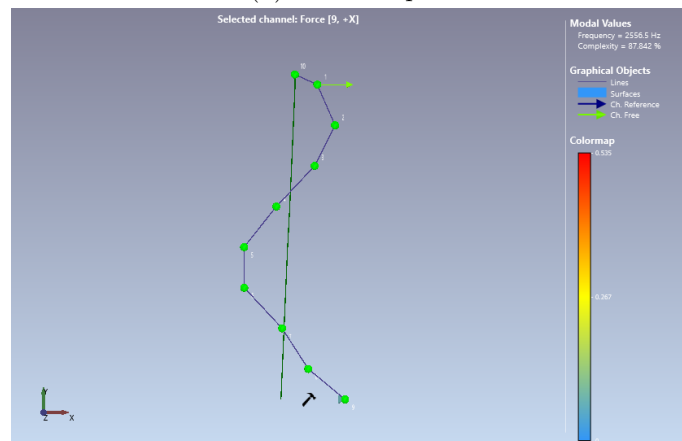
3. Experimental Tests



(a) Mode shape 1



(b) Mode shape 2



(c) Mode shape 3

Figure 3.47: Mode shapes of the EC90's handlebar

The mode shapes presented are similar to the known mode shapes of a fixed-free beam. Figure 3.48 shows the time response of the handlebar for the same measuring points of the point FRF.

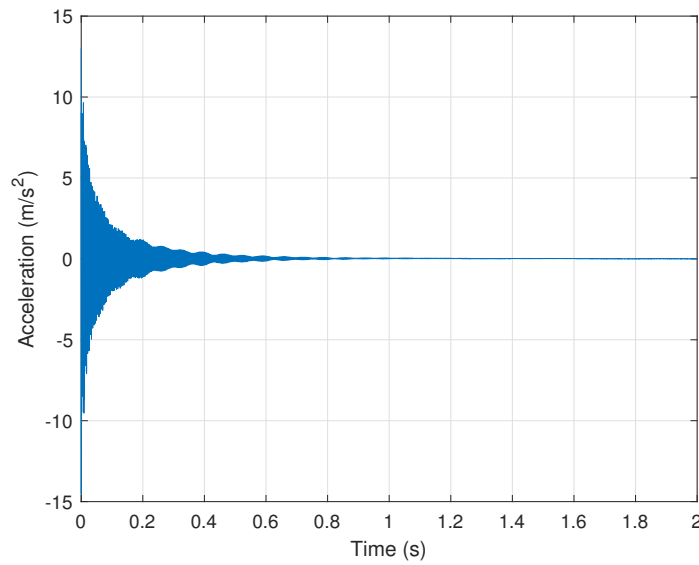


Figure 3.48: Time response for the measuring points of the point FRF_{9,9} of the EC90's handlebar

The time response follows the expected behavior. At first, the acceleration was higher due to the impact. As time goes by, the system tends to the equilibrium position.

The damping ratios of the first three modes were estimated using the circular curve fitting method. Table 3.10 presents the results considering a mean of every damping for every FRF obtained in the experimental modal analysis for each mode of the EC90's handlebar.

Table 3.10: Natural frequencies and modal damping ratios of the EC90's handlebar

	Mode 1	Mode 2	Mode 3
Natural Frequency (Hz)	247.5	1515.5	2556.5
Damping Ratio (%)	0.849	0.860	0.802

3.2.7 Comparison Between Geometries

Table 3.11 presents the natural frequencies estimated for each geometry in the experimental modal analysis.

3. Experimental Tests

Table 3.11: Identified natural frequencies (Hz) of all geometries

Geometry	Mode 1	Mode 2	Mode 3	Mode 4	Mode 5
Cylindrical Tube (400 mm)	214.9	1270.9	2811.7	-	-
Cylindrical Tube (775 mm)	56.5	346.55	927.9	1795.1	2769.5
Renthal	192.5	891.0	2282.5	-	-
OneUp	263.5	1265.5	2837.0	-	-
EC90	247.5	1515.5	2556.5	-	-

Comparing Renthal’s aluminum handlebar with the cylindrical aluminum tube of the same length (400 mm), it can be easily seen that the natural frequencies are also higher for the cylindrical tube. The differences are only due to the greater stiffness of the cylindrical tube compared to the handlebar. Comparing both cylinders, it is obvious that the longer one has lower natural frequencies.

Comparing the natural frequencies of the Renthal’s handlebar with the carbon fiber composite handlebars, it can be concluded that its natural frequencies are lower. This was expected because aluminum has a higher density than carbon fiber composites. Besides, the fact that OneUp’s handlebar is stiffer than the one from Renthal is another factor contributing to those differences. The comparison between the natural frequencies of both carbon handlebars is more complicated. The first and third natural frequencies from EC90’s handlebar are lower than OneUp’s handlebar. This can be explained by the fact that EC90’s handlebar is more flexible, as discussed in the flexural stiffness tests. However, the second natural frequency is higher, which can be attributed to the geometric differences. Table 3.12 shows the modal damping ratios of different geometries.

Table 3.12: Damping ratios (%) for each mode of different geometries

Geometry	Mode 1	Mode 2	Mode 3	Mode 4	Mode 5
Cylindrical Tube (400 mm)	0.952	0.414	0.366	-	-
Cylindrical Tube (775 mm)	2.882	0.494	0.814	0.608	0.514
Renthal	0.876	0.317	0.309	-	-
OneUp	0.745	0.641	0.827	-	-
EC90	0.849	0.860	0.802	-	-

Some amateur cyclists in some blogs or online forums say that carbon fiber composite handlebars and frames seem to be more comfortable because damping is higher when compared to other materials. Amiri et al. [2018] made some tests showing that the damping properties of carbon fiber composites are higher than aluminum. This means that what these cyclists feel can be true in the practice. The damping ratios obtained with the circular curve fitting method can also support these theories. Analyzing the damping ratios of Renthal’s handlebar and the damping ratios of the other two carbon fiber composite handlebars, it is possible to conclude that the first damping ratio from Renthal’s handlebar is slightly higher than the first damping ratio of the other two handlebars. However, the remaining damping ratios from the second and third modes are lower. The main damping mechanism present here is hysteretic damping. In this damping mechanism, there is energy

loss within the moving structure itself due to the material properties. Damping comes from the structure deformation and the conversion of mechanical energy into heat. Therefore, higher deformations result in higher energy dissipation and, consequently, higher damping. For higher modes, the structure deformation is higher, meaning that the differences in the damping ratios between materials might be attributed to this fact. This could explain the higher damping ratio of Renthal's handlebar for the first mode (lower deformation of the material) and lower ones for the remaining identified modes (higher deformation of the material). The damping ratios of the carbon fiber composite handlebars are very similar. However, in the second mode, the damping ratio of EC90's handlebar is higher.

In the case of the cylindrical tubes, the damping ratios are different. In general, the longer cylindrical tube has higher damping ratios. The higher volume of the longer cylindrical tube increases the viscous damping caused by the air. This reason is enough to justify the larger differences in damping ratios.

Finally, the damping ratios of Renthal's handlebar and the shorter cylindrical tube can be also comparable. The higher volume from the shorter cylindrical tube can justify the higher damping ratios of this geometry. Once more, the viscous damping of the air has an effect on the damping ratios.

Numerical Results

4.1 Numerical Model

4.1.1 Introduction

This section focuses on the numerical model using the commercial finite element package Ansys considered in this work. In the beginning, four different handlebar geometries were considered. It is important to highlight that the geometry is only half of the handlebar due to symmetry. There are two geometries with a 31.8 mm diameter bar clamp and two others with a 35 mm diameter. The only difference between geometries with the same clamp diameter is that the thickness must be the same all over the handlebar for one, and it is possible to have different thicknesses along different sections for the other. From now on, the geometries with different thicknesses are called split geometries. Figure 4.1 shows the 31.8 mm clamp diameter handlebar split geometry.

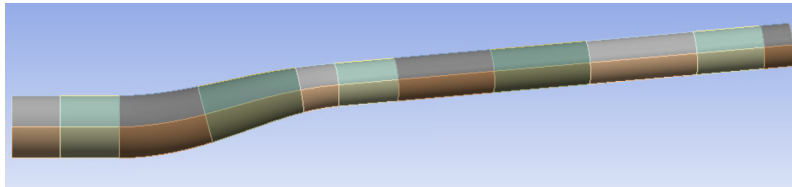


Figure 4.1: 31.8 mm diameter bar clamp handlebar split geometry - Ansys

The other dimensions of the handlebar model are equal for the 31.8 and 35 mm diameter bar clamp geometries. This way, it is easier to compare both geometries because the only difference between them is the diameter of the bar clamp.

Handlebar Geometry:

- Width - 400 mm (half of the handlebar)
- Rise: 20 mm
- Backsweep: 7°
- Upsweep: 5°

In the initial stage, all the geometries were considered. However, as the work progressed, only the split geometries were used. This happened because it is possible to have a handlebar that has not the same thickness all over the geometry. Besides, as it will

be shown later, a handlebar with regular thickness is not a good solution due to the fact that it will be heavier when compared to a handlebar with higher thickness in the critical sections and a lower thickness in the remaining zones.

4.1.2 Finite Element

There are many finite elements that can be used for meshing a given geometry, depending on the complexity. Figure 4.2 details a flowchart to help in the selection of an adequate finite element for a FEM model.

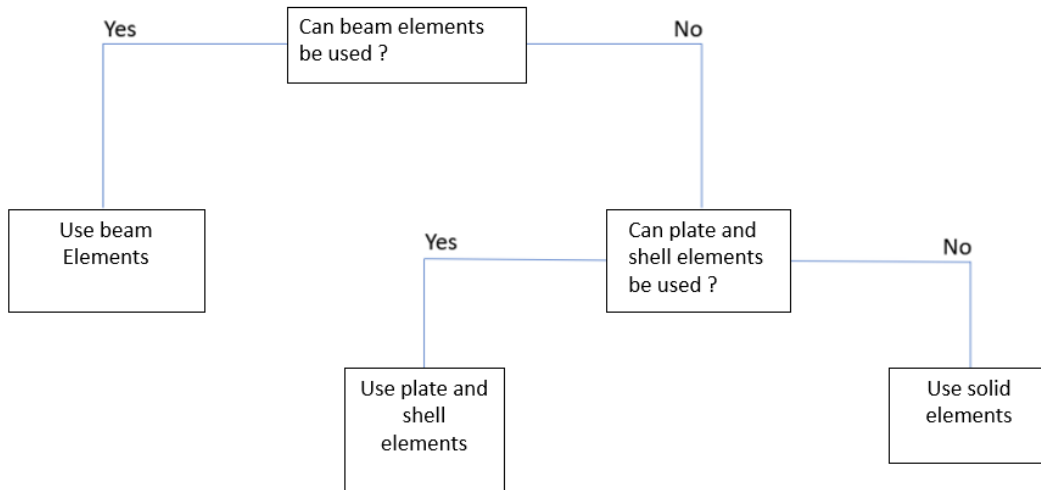


Figure 4.2: Path to follow when choosing the adequate finite element for a given model

This means that the first step is to consider if beam elements can be used. If the answer is yes, they should be used. Beam elements are considered for simple geometries and are a good choice due to the modeling and faster computation. In addition, changes in the geometry do not take too long to perform. Although, the best advantage is that it does not require too much from the computer and is fast to solve the model. However, these finite elements can just be used in basic geometries. If the answer is no, the next step is to examine if plate or shell elements can be used. In the handlebar geometry, it is not possible to use beam elements. Shell elements are still faster than solid elements and do not require huge capability from the computer. Plate and shell elements are faster than solid elements and do not require extensive capability from the computer. Plate and shell elements are extensively used for geometries with small thicknesses compared to the other dimensions. With these elements, meshing is also easier than with solid elements. Besides, it is possible to change the thickness without changing the geometry and re-meshing the whole geometry.

Another advantage is that, in some cases, the results could be more accurate than solid elements. The handlebar is an example where the thickness is much smaller than the other dimensions, and it was concluded that shell elements should be used in this work. Solid elements should be considered when plate or shell elements are not an option.

In this work, SHELL181 finite elements from ANSYS were used. It is an element well suited to the study of thin to moderately thick shell structures. It is a four-node element with six degrees of freedom at each node: x , y , and z translations, as well as rotations around the x , y , and z -axes. SHELL181 is also used for linear, large rotation,

and/or large strain nonlinear applications. Change in shell thickness is accounted for in nonlinear analyses. Both complete and limited integration techniques are supported in the element domain. The fact that SHELL181 can be used for layered applications for modeling composite shells makes it the perfect choice for the handlebar geometry because part of this work considers composite laminates. Finite membrane strains (stretching) are possible due to the element kinematics.

4.1.3 Mesh Convergence - Static Tests

The first step in the numerical model was the mesh convergence for all geometries. The objective of the mesh convergence was to obtain a refined mesh. If the element size is constantly reduced and the obtained results almost don't vary, the mesh convergence is reached. The mesh convergence is performed to reach an equilibrium between the accuracy of the model and its complexity. It is not needed a better mesh than that one because it would be heavier for the computer, and the results would be similar.

To perform the mesh convergence for all geometries, the boundary conditions of the model are a fixed support at the clamp (25 mm) and a load of 1000 N at 50 mm away from the end of the handlebar. The boundary conditions are in agreement with the standard ISO 4210-5:2014 - Lateral bending test. These boundary conditions are not just considered in the mesh convergence but also in almost all the analyses conducted in this work. Figure 4.3 shows the boundary conditions.

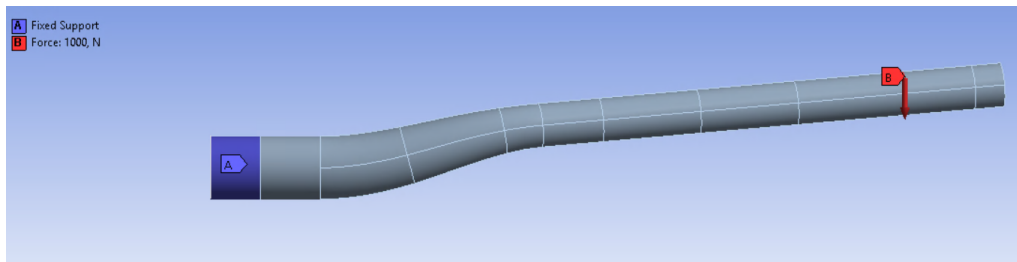


Figure 4.3: Boundary conditions of the model

The material used to perform the mesh convergence was the Aluminum 7050 T-7651. The material properties are presented in the next section, together with all the material properties considered in the FEM analysis. The thickness was 1.5 mm, equal all over the handlebar. This material was chosen once it is very similar to the one from Renthal's handlebar.

31.8 mm Diameter Geometry

In all geometries, the mesh has to be as regular as possible. To have a regular mesh, the number of elements along the circumferential direction is defined. This way, the geometries have the same number of elements along the circumferential direction for the entire handlebar. The number of elements in all sections through the length is also defined. This way, it is easy to obtain the number of elements all over the length of the model.

To refine the mesh, it is required to increase the number of elements in both directions until the stress at a specific point and the average displacement at 15 mm apart from the end of the handlebar converge. The stress is computed at a point belonging to a critical section for all geometries. Figures 4.4 and 4.5 show the point where the stress and the edge where the displacements are computed, respectively.

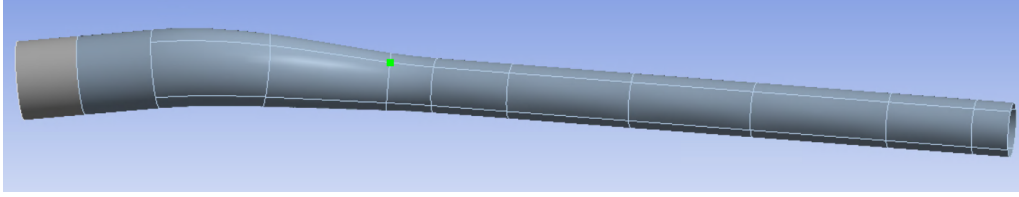


Figure 4.4: The point where the stress is computed

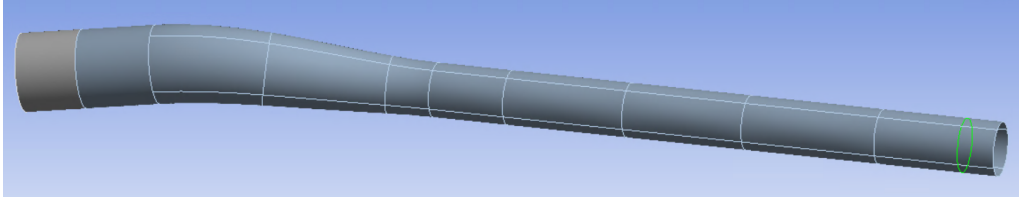


Figure 4.5: The edge where the displacement is computed

As mentioned before, the number of elements increases with mesh refinement, and the main goal is to reach a mesh for which results converge. Table 4.1 shows the results obtained with Ansys for different meshes.

Table 4.1: Mesh convergence for the 31.8 mm diameter geometry

Elements (Circumferential- Length)	Elements (Total)	Nodes	Stress (MPa)	Displacement (mm)
24-79	1896	1920	397.12	18.56
28-95	2660	2688	396.96	18.51
28-116	3248	3276	397.44	18.51
32-140	4480	4512	397.14	18.47
32-159	5088	5120	397.30	18.47
32-164	5248	5280	397.12	18.47
36-188	6768	6804	396.79	18.45
40-216	8640	8680	396.56	18.43
40-226	9040	9080	396.64	18.43
44-246	10824	10868	396.62	18.41
48-289	13872	13920	396.38	18.40
52-289	15028	15080	396.28	18.40

As can be seen from the convergence results, the differences between stress and displacement values are small. This means that mesh convergence was reached for this geometry. Multiplying the number of elements along the circumferential direction for the number of elements along the length gives the total number of elements of the mesh. For the 31.8 mm diameter geometry, the last mesh in Table 4.1 with 52 elements along the circumferential direction and 289 elements along the length is the mesh used afterward. As discussed later in this work, there are no significant differences between the static and modal analyses regarding mesh convergence.

31.8 mm Diameter Split Geometry

Following the same approach, the process was repeated for the 31.8 mm diameter split geometry. The number of elements through the length in this case, is slightly different than before. So the total number of elements is a little different. However, this has practically no influence on the variation of the obtained values. Table 4.2.

Table 4.2: Mesh convergence for 31.8 mm diameter split geometry

Elements (Circumferential- Length)	Elements (Total)	Nodes	Stress (MPa)	Displacement (mm)
24-78	1872	1896	409.02	18.56
28-94	2632	2660	406.98	18.51
28-110	3080	3108	406.86	18.51
32-134	4288	4320	405.62	18.47
32-142	4544	4576	405.06	18.47
32-148	4736	4768	404.66	18.47
36-170	6120	6156	403.42	18.45
40-204	8160	8200	402.41	18.43
44-242	10648	10692	401.6	18.42
48-264	12672	12720	400.95	18.40
52-286	14872	14924	400.24	18.40

As can be seen in the Table 4.2, the last values start to converge compared to the initial ones. After the convergence analysis, the mesh used for this geometry was 52 elements at a circumferential level and 286 through the length. In the split geometry, the stress is computed at the same point, but it is slightly different from the no split geometry. The difference is that there are many surfaces to be able to have different thicknesses along the handlebar in the split geometry, and the software computes the stress from different surfaces. There is displacement continuity between surfaces, but not stress continuity. This creates discontinuities in the stress in the interface between the different surfaces, and the computed stress is slightly higher than in the 31.8 mm diameter geometry. Nevertheless, it has not had a huge influence on this problem. Figure 4.6 helps to illustrate these discontinuities..

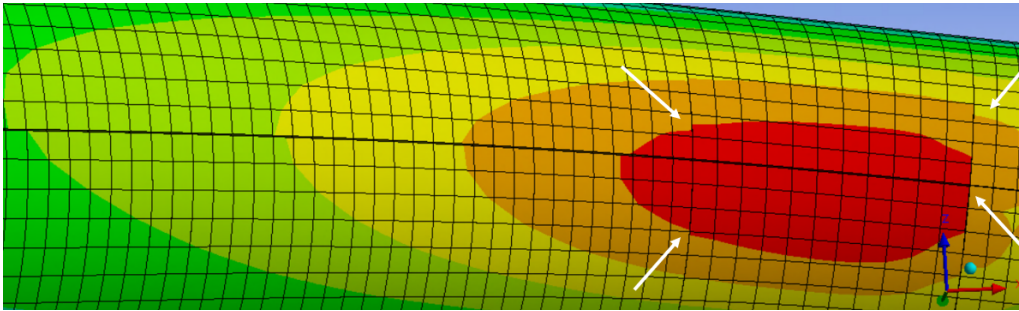


Figure 4.6: Discontinuities in the stress analysis in the 31.8 mm diameter split geometry

35 mm Diameter Geometry

The convergence analysis for this geometry followed the same procedure. The difference between the geometries of 35 mm and 31.8 mm diameter is that the meshes of the 35 mm diameter geometries must have more elements at both levels due to the higher diameter in the bar clamp. As in the previous cases, the mesh convergence was performed by increasing the number of elements circumferentially and along the length. The stresses and displacements were computed in the same positions as the previous ones. Table 4.3 presents the results of stress and displacement for the different meshes.

Table 4.3: Mesh convergence for 35 mm diameter geometry

Elements (Circumferential- Length)	Elements (Total)	Nodes	Stress (MPa)	Displacement (mm)
24-79	1896	1920	398.45	16.80
28-95	2660	2688	398.33	16.75
28-116	3248	3276	398.85	16.75
32-140	4480	4512	398.59	16.72
32-159	5088	5120	398.75	16.72
32-164	5248	5280	398.59	16.72
36-188	6768	6804	398.27	16.70
40-216	8640	8680	398.03	16.68
40-226	9040	9080	398.11	16.68
44-246	10824	10868	398.07	16.67
48-289	13872	13920	397.83	16.66
52-289	15028	15080	397.72	16.65
56-312	17472	17528	397.57	16.64
60-330	19800	19860	397.44	16.64
68-330	22440	22508	397.33	16.63

As can be seen in the Table 4.3, the last values start to converge and present smaller and smaller variations from each other. This means that the mesh convergence was reached. After the convergence analysis, the mesh used for this geometry was 68 elements at a circumferential level and 330 through the length.

35 mm Diameter Split Geometry

Following the same approach, the process was repeated for the 35 mm diameter split geometry. The stress and displacement were computed in the same positions as the previous geometries. Table 4.4 presents the stress and displacement results for the 35 mm diameter split geometry.

Table 4.4: Mesh convergence for 35 mm diameter split geometry

Elements (Circumferential- Length)	Elements (Total)	Nodes	Stress (MPa)	Displacement (mm)
24-78	1872	1896	410.33	16.80
28-94	2632	2660	408.37	16.75
28-110	3080	3108	408.23	16.75
32-134	4288	4320	406.89	16.72
32-142	4544	4576	406.51	16.72
32-148	4736	4768	406.14	16.72
36-170	6120	6156	404.90	16.70
40-204	8160	8200	403.88	16.68
44-242	10648	10692	403.07	16.67
48-264	12672	12720	402.41	16.66
52-286	14872	14924	401.87	16.65
56-300	16800	16856	401.33	16.64
60-314	18840	18900	400.90	16.64
64-324	20736	20800	400.67	16.64
64-330	21120	21760	400.65	16.64

As can be seen in Table 4.4, the last values start to converge compared to the initial ones. After the convergence analysis, the mesh used for this geometry was 64 elements at a circumferential level and 330 elements along the length. Here, as in the 31.8 mm diameter split geometry, the stress is slightly different than the 35 mm diameter no split geometry. The explanation for this is the same. The stress is different because there is displacement continuity between surfaces, but not stress continuity.

4.1.4 Mesh Convergence - Modal Analysis

In addition to the mesh convergence in terms of stress and static displacement, the first ten natural frequencies of each geometry were also computed to check if the mesh was already converging for natural frequencies or if it needed a more refined mesh. To notice that in this section the thickness used was constant along the length and of 1.5 mm.

31.8 mm Diameter Geometry

Table 4.5 presents the results of the first ten natural frequencies for this geometry with the first and last mesh that have been previously considered for this geometry. The process was performed for all the meshes used before in the static mesh convergence. However, only the results of the first and last mesh are shown.

Table 4.5: Mesh convergence (modal analysis) for 31.8 mm diameter geometry

Elements (Circumferential-Length)	Natural Frequencies (Hz)
24-79	201.9
	202.0
	1043.8
	1050.1
	2437.6
	2551.7
	2642.8
	3553.6
	4782.9
	4843.3
52-289	202.5
	202.6
	1047.0
	1053.5
	2441.3
	2556.2
	2647.9
	3552.7
	4787.3
	4847.8

Analyzing the results, it is easy to conclude that the mesh refinement has a lower influence on the first ten natural frequencies than the static analysis, namely stress. So the mesh is defined by the stress analysis. After the convergence analysis, the mesh used for this geometry was 52 elements at a circumferential level and 289 through the length.

31.8 mm Diameter Split Geometry

As mentioned before, the mesh refinement does not have a major influence on the modal analysis. Therefore, Table 4.6 presents the ten first natural frequencies of the mesh selected before.

Table 4.6: Mesh convergence (modal analysis) for 31.8 mm diameter split geometry

Elements (Circumferential-Length)	Natural Frequencies (Hz)
52-286	202.5
	202.6
	1047.0
	1053.4
	2441.3
	2556.2
	2647.9
	3552.7
	4787.2
	4847.8

As expected, the natural frequencies are similar to the natural frequencies of 31.8 mm diameter geometry.

35 mm Diameter Geometry

Table 4.7 shows the first ten natural frequencies for the 35 mm diameter geometry with a mesh with 68 elements at the circumferential level and with 330 elements through the length.

Table 4.7: Mesh convergence (modal analysis) for 35 mm diameter geometry

Elements (Circumferential-Length)	Natural Frequencies (Hz)
68-330	215.2
	215.3
	1101.5
	1107.1
	2513.9
	2602.7
	2694, 6
	3625.5
	4849.2
	4892.1

Comparing the natural frequencies of the 35 mm diameter geometries with the 31.8 mm diameter geometries, it is easy to conclude that natural frequencies are higher in the first case, justified by the fact that this geometry is stiffer, being the natural frequencies higher.

35 mm Diameter Split Geometry

As in the previous geometries, the mesh refinement does not have a major influence on the modal analysis. So in Table 4.8, it is possible to see the first ten natural frequencies of this geometry with a mesh with 64 elements at the circumferential level and with 339 elements throughout the length.

Table 4.8: Mesh convergence (modal analysis) for 35 mm diameter split geometry

Elements (Circumferential-Length)	Natural Frequencies (Hz)
64-339	215.1
	215.3
	1101.4
	1107
	2513.8
	2602.5
	2694.5
	3625.5
	4848.9
	4891.8

As expected, the natural frequencies are similar to the natural frequencies of the 35 mm diameter with no split geometry.

4.2 Materials

There were different materials under consideration in the simulations performed during this work. In this section, those materials and the corresponding properties used in the FEM analysis are presented.

4.2.1 Aluminum 7050 T-7651

This is the aluminum with the most similar properties to the one used in Renthal's handlebar. Table 4.9 shows the properties of Aluminum 7050 T-7651 used in the FEM analysis.

Table 4.9: Properties of Aluminum 7050 T-7651 used in the FEM analysis

Density (kg/m³)	2830
Young's Modulus (GPa)	71.7
Poisson's Ratio	0.33
Bulk Modulus (GPa)	70.294
Shear Modulus (GPa)	26.955
Tensile Yield Strength(MPa)	490
Tensile Ultimate Strength (MPa)	552

4.2.2 Titanium 3AL-2.5 V

This is a titanium that is many times used in bicycles made of titanium. Table 4.10 shows the properties of Titanium 3AL-2.5 V used in the FEM analysis.

Table 4.10: Properties of Titanium 3AL-2.5 V used in the FEM analysis

Density (kg/m³)	4470
Young's Modulus (GPa)	91
Poisson's Ratio	0.35
Bulk Modulus (GPa)	101.11
Shear Modulus (GPa)	33.704
Tensile Yield Strength(MPa)	483
Tensile Ultimate Strength (MPa)	621

4.2.3 Bcomp TDS - Prepreg - ampliTex 150 gsm UD 44% RW - Generic

This material consists of unidirectional flax fibers with 150 gsm and 44% fiber volume fraction. Table 4.11 shows the properties of the unidirectional flax fiber composite used in this work provided by their Research and Development team, as well as some estimated properties.

Table 4.11: Properties of Bcomp TDS - Prepreg - ampliTex 150 gsm UD 44% RW - Generic used in the FEM analysis

Ply Density (kg/m³)	1330
Ply Thickness (mm)	0.20
Young's Modulus X (GPa)	32.5
Young's Modulus Y (GPa)	4.8
Poisson's Ratio XY	0.39
Poisson's Ratio YZ	0.05
Poisson's Ratio XZ	0.39
Shear Modulus XY (GPa)	2
Shear Modulus YZ (GPa)	2
Shear Modulus XZ (GPa)	2
Tensile X - Stress(MPa)	345
Tensile Y - Stress(MPa)	50
Compressive X - Stress (MPa)	-172.5
Compressive Y - Stress (MPa)	-172.5
Shear XY - Stress (MPa)	35
Shear YZ - Stress (MPa)	35
Shear XZ - Stress (MPa)	35
Tensile X - Strain	0.009
Tensile Y - Strain	0.010417
Compressive X - Strain	-0.00531
Compressive Y - Strain	-0.03594
Shear XY - Strain	0.01750
Shear YZ - Strain	0.01750
Shear XZ - Strain	0.01750

As mentioned before, some values were not given and so were estimated. It was assumed that Young's modulus and tensile stress in direction Z were equal to the value in the Y direction. Besides, it was assumed that the shear stress and shear modulus in all

directions are equal. The Poisson's ratio was considered equal in the directions XY and XZ. The compressive stress was estimated by analyzing other flax fiber composites from other companies. However, the assumed values were a little more conservative and equal in all directions. Regarding strain, only the tensile X is known. The remaining ones were estimated.

The following equations were used to calculate each value of tensile and compressive strain.

$$\varepsilon_1 = \frac{\sigma_1}{E_1} \quad (4.1)$$

$$\varepsilon_2 = \frac{\sigma_2}{E_2} \quad (4.2)$$

$$\varepsilon_3 = \frac{\sigma_3}{E_3} \quad (4.3)$$

To estimate the value of shear strain, the following equations were considered.

$$\gamma_{12} = \frac{\tau_{12}}{G_{12}} \quad (4.4)$$

$$\gamma_{13} = \frac{\tau_{13}}{G_{13}} \quad (4.5)$$

$$\gamma_{23} = \frac{\tau_{23}}{G_{23}} \quad (4.6)$$

where G is the shear modulus and E is the Young's modulus.

4.2.4 Bcomp TDS - Prepreg - ampliTex 500 gsm twill 4-4 44% RW - Generic

This material consists of flax fibers with 500 gsm and a 44% fiber volume fraction. The main difference between this material and the previous one is the fact that this material is a woven flax fiber composite and has the same properties in the X and Y directions. Table 4.12 shows the properties of the woven flax fiber composite used in this work provided by their Research and Development, as well as some estimated properties.

Table 4.12: Properties of Bcomp TDS - Prepreg - ampliTex 500 gsm twill 4-4 44% RW - Generic used in the FEM analysis

Ply Density (kg/m³)	1340
Ply Thickness (mm)	0.65
Young's Modulus X (GPa)	18.5
Young's Modulus Y (GPa)	18.5
Poisson's Ratio XY	0.11
Poisson's Ratio YZ	0.11
Poisson's Ratio XZ	0.11
Shear Modulus XY (GPa)	2.1
Shear Modulus YZ (GPa)	1.5
Shear Modulus XZ (GPa)	1.5
Tensile X - Stress(MPa)	179
Tensile Y - Stress(MPa)	179
Compressive X - Stress (MPa)	-145
Compressive Y - Stress (MPa)	-145
Shear XY - Stress (MPa)	89.1
Shear YZ - Stress (MPa)	27
Shear XZ - Stress (MPa)	27
Tensile X - Strain	0.00968
Tensile Y - Strain	0.00968
Compressive X - Strain	-0.00784
Compressive Y - Strain	-0.00784
Shear XY - Strain	0.04243
Shear YZ - Strain	0.01800
Shear XZ - Strain	0.01800

It was assumed that the Young's Modulus, Poisson's ratio, tensile stress, and compressive stress are equal in all directions. The assumed compressive stress values are conservative estimates. The shear modulus and stress were assumed equal in directions YZ and XZ. The strain values were calculated in the same way as before.

4.2.5 XC110 210g 2x2 Twill 3k Prepreg Carbon Fiber

This material consists of a woven carbon fiber composite with 210 gsm and 58% fiber volume fraction. Table 4.13 shows the properties of the woven carbon fiber composite used in this work, which can be found in Appendix, as well as some estimated properties.

Table 4.13: Properties of XC110 210g 2x2 Twill 3k Prepreg Carbon Fibre used in the FEM analysis

Ply Density (kg/m³)	1152
Ply Thickness (mm)	0.25
Young's Modulus X (GPa)	46.7
Young's Modulus Y (GPa)	46.7
Poisson's Ratio XY	0.04
Poisson's Ratio YZ	0.3
Poisson's Ratio XZ	0.3
Shear Modulus XY (GPa)	3.3
Shear Modulus YZ (GPa)	2.7
Shear Modulus XZ (GPa)	2.7
Tensile X - Stress(MPa)	777
Tensile Y - Stress(MPa)	777
Compressive X - Stress (MPa)	-483
Compressive Y - Stress (MPa)	-483
Shear XY - Stress (MPa)	64.7
Shear YZ - Stress (MPa)	64.7
Shear XZ - Stress (MPa)	64.7
Tensile X - Strain	0.01664
Tensile Y - Strain	0.01664
Compressive X - Strain	-0.01034
Compressive Y - Strain	-0.01034
Shear XY - Strain	0.01961
Shear YZ - Strain	0.02396
Shear XZ - Strain	0.02396

The Poisson's ratios were not disclosed in the catalog of the material, so the values were estimated using the ones of the default material Epoxy Carbon Woven (230 GPa) Prepreg of the Ansys software. The same goes for the shear modulus. The tensile, compressive, and shear stress in X and Y directions are known. Lastly, the tensile, compressive, and shear strain values were calculated using the equations presented before.

4.3 Comparison of the Model with Different Materials

The stress and displacement are computed in the same positions as before. Table 4.14 presents the results of stress and displacement calculated in the software Ansys for different materials and geometries. It is important to highlight that the meshes used for all geometries are the ones selected in the mesh convergence section, and the model thickness is 1.5 mm, equal for all handlebars. The boundary conditions are in agreement with ISO 4210-5:2014 - Lateral bending test being the load of 1000 N and the displacement computed at 50 mm from the end of the handlebar.

Table 4.14: Stress and displacement of the different geometries using two materials

Material	Geometry	Stress (MPa)	Displacement (mm)
Aluminum	31.8 mm diameter	396.28	18.40
	31.8 mm diameter split	400.42	18.40
	35 mm diameter	397.32	16.63
	35 mm diameter split	400.65	16.64
Titanium	31.8 mm diameter	398.49	14.49
	31.8 mm diameter split	402.89	14.49
	35 mm diameter	399.61	13.10
	35 mm diameter split	403.15	13.10

The differences in stress between the different geometries using aluminum were already discussed. So, as reported previously, for geometries with the same diameter and material, the stress is slightly different due to the stress discontinuities. For the geometries with different diameters, the stress is higher in the geometry with a higher diameter, as expected. Nevertheless, this difference is minimal. The same is valid for titanium. The displacement is equal for geometries with the same diameter and material. For the geometries with different diameters and the same material, the displacement is lower in the geometries where the diameter is higher, as expected. It can be concluded that the stress is higher when using titanium when comparing the same geometry using different materials. The displacement is lower when using titanium since this material is much stiffer than aluminum. Furthermore, the first ten natural frequencies were obtained in Ansys for the different geometries using aluminum and titanium. Tables 4.15, 4.16, 4.17, and 4.18 show those results.

Table 4.15: Natural frequencies of the 31.8 mm diameter geometries using aluminum

Material	Geometry	Natural Frequencies (Hz)
Aluminum 7050 T-7651	31.8 mm diameter	202.5
		202.6
		1047.0
		1053.5
		2441.3
		2556.2
		2647.9
		3552.7
	31.8 mm diameter split	4787.3
		4847.8
		202.5
		202.6
		1047.0
		1053.4
		2441.3
		2556.2
		2647.9
		3552.7
		4787.2
		4847.8

Table 4.16: Natural frequencies of the 35 mm diameter geometries using aluminum

Material	Geometry	Natural Frequencies (Hz)
Aluminum 7050 T-7651	35 mm diameter	215.2
		215.3
		1101.5
		1107.1
		2513.9
		2602.7
		2694.6
		3625.5
		4849.2
		4892.1
	35 mm diameter split	215.1
		215.3
		1101.4
		1107.0
		2513.8
		2602.5
		2694.5
		3625.5
		4848.9
		4891.8

Table 4.17: Natural frequencies of the 31.8 mm diameter geometries using titanium

Material	Geometry	Natural Frequencies (Hz)
Titanium 3AL-2.5V	31.8 mm diameter	181.6
		181.7
		938.3
		944.1
		2173.8
		2290.3
		2370.6
		3183.8
		4286.4
		4341.4
	31.8 mm diameter split	181.6
		181.7
		938.3
		944.1
		2173.8
		2290.3
		2370.6
		3183.8
		4286.3
		4341.3

Table 4.18: Natural frequencies of the 35 mm diameter geometries using titanium

Material	Geometry	Natural Frequencies (Hz)
Titanium 3AL-2.5V	35 mm diameter	192.9
		193.0
		987.0
		992.1
		2238.5
		2331.9
		2412.3
		3249.0
	35 mm diameter split	4341.9
		4381.4
		192.9
		193.0
		987.0
		992.0
		2238.4
		2331.7
		2412.1
		3249.0
		4341.6
		4381.1

Natural frequencies are very similar for the geometries with the same diameter using the same material. However, as expected, natural frequencies are slightly different for different diameters. In geometries with a higher diameter, the natural frequencies are also higher. Handlebars with a higher diameter are stiffer, so the natural frequencies are higher. The same is valid for aluminum and also for titanium. When comparing the same geometries with different materials, it is easy to notice that the natural frequencies of titanium handlebars are lower. This can be explained by the fact that titanium has a higher density than aluminum, decreasing the natural frequencies of the handlebar.

4.4 Variable Thickness Model using Aluminum 7050 T-7651

From this point until the end, only the 31.8 mm and 35 mm diameter split geometries were used once the results of both geometries with the same diameter were very similar. Firstly, the simulations were performed for different thickness values using the 31.8 mm diameter split geometry. It is important to highlight that the same thickness all over the handlebar was considered at first. The parameters analyzed here were the mass of the handlebar, the displacement at 15 mm from the end of the handlebar, the structural safety factor, and also the fatigue safety factor. The boundary conditions were the load of 1000 N at 50 mm from the end of the handlebar and the fixed support in the middle of the handlebar in agreement with ISO 4210-5:2014 - Lateral bending test. Table 4.19 shows the results from 31.8 mm diameter split geometry.

Table 4.19: Results of 31.8 mm diameter split geometry for constant thickness

Thickness (mm)	Mass (kg)	Max Stress (MPa)	Displacement (mm)	Safety Factor	Fatigue Safety Factor
1.5	0.13463	486.05	20.81	1.01	0.90
1.6	0.14360	451.07	19.58	1.09	0.97
1.7	0.15258	420.51	18.51	1.17	1.04
1.8	0.16155	393.64	17.57	1.24	1.11
1.9	0.17053	369.88	16.73	1.32	1.18
2.0	0.17950	348.76	15.98	1.40	1.26
2.1	0.18848	329.89	15.31	1.49	1.33
2.2	0.19745	312.96	14.70	1.57	1.40
2.3	0.20643	298.38	14.15	1.64	1.47
2.4	0.21540	288.24	13.65	1.70	1.52
2.5	0.22438	279.02	13.19	1.76	1.57

Analyzing the structural safety factor and the fatigue safety factor of the different thicknesses, it is easy to conclude that having the same thickness for the entire handlebar is not the best option once the safety factors are not sufficient without compromising the handlebar in terms of mass. This means it could be possible to reduce the mass without compromising the safety factors if the handlebar has a variable thickness. Therefore, using the 31.8 mm diameter split geometry, the model was numerically solved for many cases varying the thicknesses in the different sections. The mass of the Renthal's handlebar is a great way to compare with the model. Table 4.20 shows the most promising results with a similar mass to the Renthal's handlebar. It is important to mention that for the fatigue safety factor, the handlebar was submitted to a zero-based cyclic load with a maximum amplitude of 450 N in agreement with the ISO 4210-5:2014 - Fatigue test. The loading shouldn't exceed the frequency of 10 Hz, according to ISO 4210-3:2014 - Fatigue test. Therefore, the frequency considered was 10 Hz. The criterium used was Goodman which is slightly less conservative than the Soderberg criterium. As presented previously, aluminum is a material with low fatigue resistance compared with other structural materials, being one of the cons of its use in handlebars.

Table 4.20: Results of 31.8 mm diameter split geometry for variable thickness

Thicknesses (mm)	Mass (kg)	Max Stress (MPa)	Displacement (mm)	Safety Factor	Fatigue Safety Factor
2.0/2.0/1.8/1.8/	0.15887	358.49	17.17	1.37	1.22
2.0/1.9/1.8/1.7/					
1.5/1.5/1.5					
2.1/2.1/1.8/1.8/	0.15788	352.43	17.26	1.39	1.24
2.1/1.9/1.7/1.5/					
1.5/1.5/1.5					
2.1/2.1/1.8/1.8/	0.15886	352.43	17.19	1.39	1.24
2.1/1.9/1.7/1.6/					
1.5/1.5/1.5					

As mentioned before, Table 4.20 only presents the most promising cases. However, many more cases were simulated, but the fatigue safety factors were not as high, or the total

mass of the handlebar was very high compared with Renthal's handlebar. The presented cases are those where the double mass of the model (total mass of the handlebar) was similar to Renthal's handlebar mass and had better safety factors. The model with the best compromise between mass and safety factors is the second one. Here, the mass is very similar to the Renthal's Handlebar, and both safety factors are high enough.

After that, the procedure was repeated for the 35 mm diameter split geometry. There was no commercial aluminum handlebar of 35 mm for this geometry to compare. However, it can be used with the same thicknesses that have been used before for the best cases of the 31.8 mm handlebar. Table 4.21 shows the results of the most promising cases for the 35 mm diameter split geometry.

Table 4.21: Results of 35 mm diameter split geometry for variable thickness

Thicknesses (mm)	Mass (kg)	Max Stress (MPa)	Displacement (mm)	Safety Factor	Fatigue Safety Factor
2.0/2.0/1.8/1.8/ 2.0/1.9/1.8/1.7/ 1.5/1.5/1.5	0.16508	357.51	15.54	1.37	1.23
2.1/2.1/1.8/1.8/ 2.1/1.9/1.7/1.5/ 1.5/1.5/1.5					
2.1/2.1/1.8/1.8/ 2.1/1.9/1.7/1.6/ 1.5/1.5/1.5					
2.1/2.1/1.8/1.8/ 2.1/1.9/1.7/1.5/ 1.5/1.5/1.5	0.16425	357.14	15.65	1.37	1.23
2.1/2.1/1.8/1.8/ 2.1/1.9/1.7/1.6/ 1.5/1.5/1.5	0.16522	357.14	15.58	1.37	1.23

The safety factors were very similar to the previous results. As expected, the displacement was lower, leading to a stiffer handlebar than the 31.8 mm diameter one.

4.5 Model Validation

One of the methods embraced to validate the model was comparing the stiffness of the FEM model with the stiffness obtained in the stiffness tests for the 35 mm diameter aluminum cylindrical tube with 400 mm length and also for Renthal's handlebar.

It is also important to compare the displacements in the cylindrical tube obtained in stiffness tests and FEM analysis with the theoretical value. The method used to calculate the theoretical displacements in the tube was Castigliano's theorem. In Figure 4.7, it is possible to see the boundary conditions of the theoretical problem.

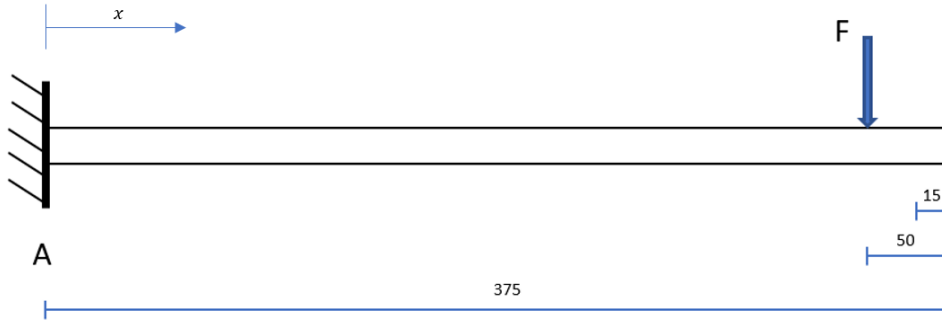


Figure 4.7: Boundary conditions of the problem

To calculate the displacement at 15 mm from the end of the cylindrical tube by Castigliano's theorem, a fictional load P introduced at that point is required. Figure 4.8 shows this process.

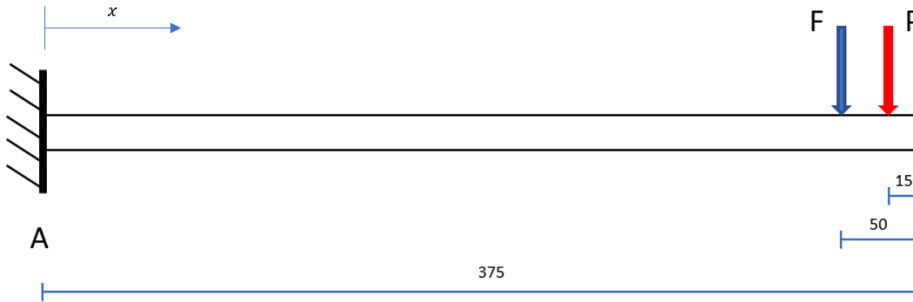


Figure 4.8: First step of solving the problem by Castigliano's theorem

The second step is to calculate the reaction forces in point A. In the next equations, those calculations are shown.

$$R_x = 0 \quad (4.7)$$

$$R_y = F + P \quad (4.8)$$

$$M_A = F \times 0,325 + P \times 0,360 \quad (4.9)$$

The bending moments must be calculated after the reaction forces. For that, it is necessary to calculate the bending moment from section $0 < x < 0,325$ and from $0,325 < x < 0,360$. Figure 4.9 shows the section cut considered.

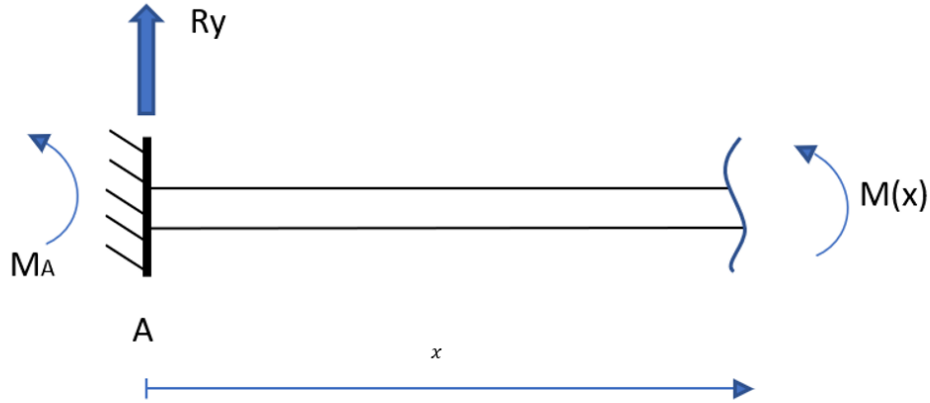


Figure 4.9: Calculation of the bending moment for the first section

In the following equation is presented the calculation of the bending moment of the first section.

$$M_x = F(x - 0,325) + P(x - 0,360) \quad (4.10)$$

Figure 4.10 shows the section cut for the second section.

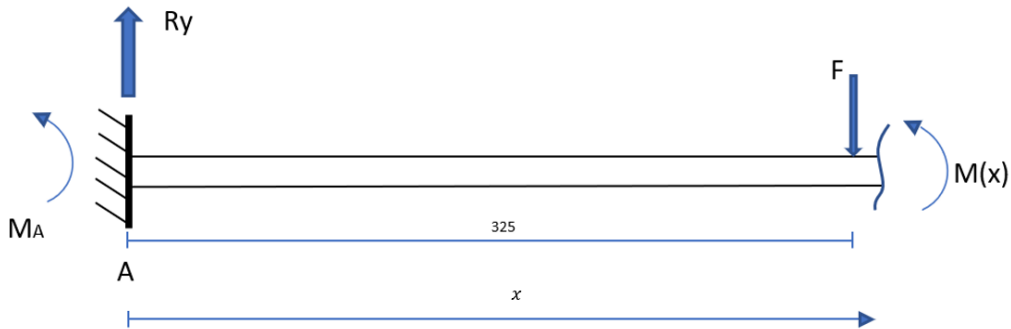


Figure 4.10: Calculation of the bending moment for the second section

The calculation of the bending moment of the first section is presented in the following equation.

$$M_x = P(x - 0,360) \quad (4.11)$$

After the bending moments for both sections, the displacement can be calculated. The following equation is used to calculate the vertical displacement in a beam at the point where the load is applied.

$$\delta_t = \int_0^l \frac{M(x)}{EI} \left(\frac{\partial M(x)}{\partial P} \right) dx \quad (4.12)$$

The following equation expresses the vertical displacement of the cylindrical tube at 15 mm from its tip.

$$\delta_t = \delta_1 + \delta_2 = \int_0^{0,325} \frac{(F(x - 0, 325) + P(x - 0, 360))(x - 360)}{EI} dx + \int_{0,325}^{0,360} \frac{P(x - 0, 360)(x - 0, 360)}{EI} dx \quad (4.13)$$

During the calculation of the displacement after the derivation of M in order to P, the fictional load should have the value of zero. The following equation is the final equation to calculate the displacement.

$$\delta_t = \delta_1 + \delta_2 = \int_0^{0,325} \frac{F(x - 0, 325)(x - 360)}{EI} dx + \int_{0,325}^{0,360} \frac{(x - 0, 360)}{EI} dx \quad (4.14)$$

Table 4.22 presents the displacement values obtained for the different loads (stiffness tests) for the cylindrical tube of 400 mm in length and 35 mm in diameter. The Young's Modulus used in theoretical values was 71.7 GPa.

Table 4.22: Displacements of the 35 mm cylindrical aluminum tube for different loads

Load (N)	Displacement (mm)		
	Experimental	FEM	Theoretical
0	0		
20.39	0.16	0.19	0.17
40.28	0.38	0.38	0.34
60.25	0.61	0.57	0.50
79.92	0.85	0.76	0.67
99.80	1.10	0.95	0.83
120.79	1.35	1.15	1.01
140.60	1.61	1.34	1.17
160.46	1.85	1.53	1.34
178.23	2.06	1.70	1.49
195.76	2.30	1.87	1.63

After that, the results were used to plot the flexural stiffness considering experimental results, the FEM model, and the theoretical cylindrical tube -Figure 4.11.

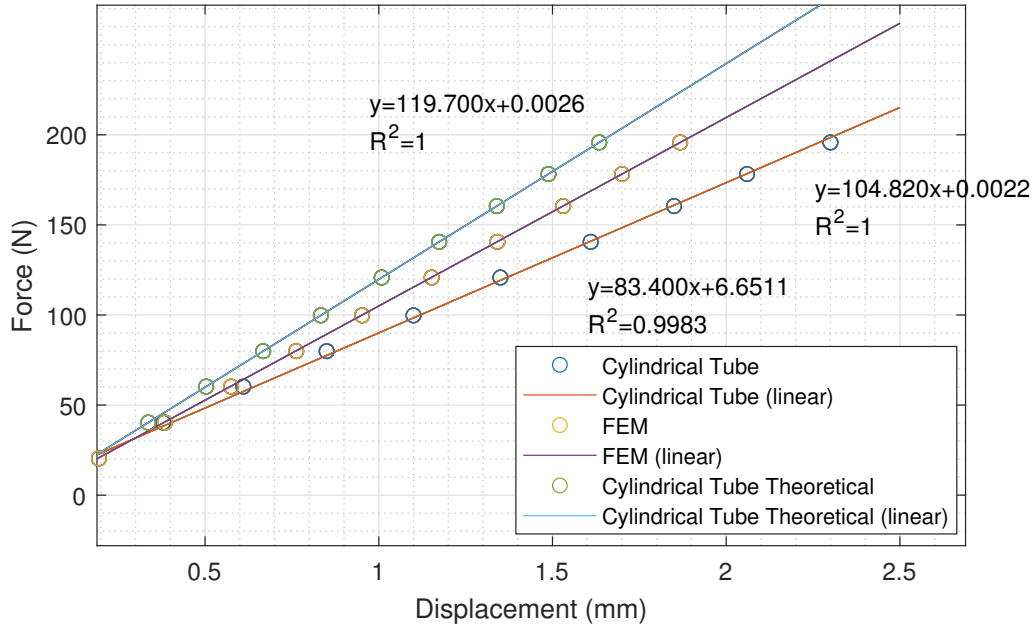


Figure 4.11: Stiffness plot from real cylinder, FEM model and theoretical cylinder

Analyzing the results, the slope of the regression line in the FEM model is higher. This means that the FEM model is stiffer. This could be explained by the perfect fixed support of the FEM model. In the experimental test, this doesn't happen once there are no undeformable bodies and pure fixed supports. Therefore, the stiffness will be lower than the one from the FEM model. The calculation of the relative differences in flexural stiffness between the experimental values and FEM model is shown in the following equation.

$$\text{Relative Difference} = \frac{104.820 - 83.400}{104.820} = 20.3\% \quad (4.15)$$

In the following equations are presented the relative differences between the experimental results and the FEM model in comparison with the theoretical cylindrical tube, respectively.

$$\text{Relative Difference} = \frac{119.700 - 104.820}{119.700} = 12.4\% \quad (4.16)$$

$$\text{Relative Difference} = \frac{119.700 - 83.400}{119.700} = 30.3\% \quad (4.17)$$

The theoretical flexural stiffness is higher because the Euler-Bernoulli beam formulation used in Castigliano's theorem is appropriate for thin beams, which is not the case here.

The same procedure was applied for the Renthal's handlebar. Table 4.23 shows the displacements of the Renthal's handlebar.

Table 4.23: Displacements of the Renthal's handlebar

Load (N)	Displacement (mm)	
	Experimental	FEM
0	0	
20.39	0.38	0.35
40.28	0.81	0.70
60.25	1.27	1.04
79.92	1.72	1.38
99.80	2.19	1.72
120.79	2.66	2.09
140.60	3.13	2.43
160.46	3.58	2.77
178.23	3.89	3.08
195.76	4.05	3.38

Following the same procedure, it is possible to plot the flexural stiffness for the handlebar and its FEM model. Figure 4.12 shows the flexural stiffness plot for Renthal's handlebar.

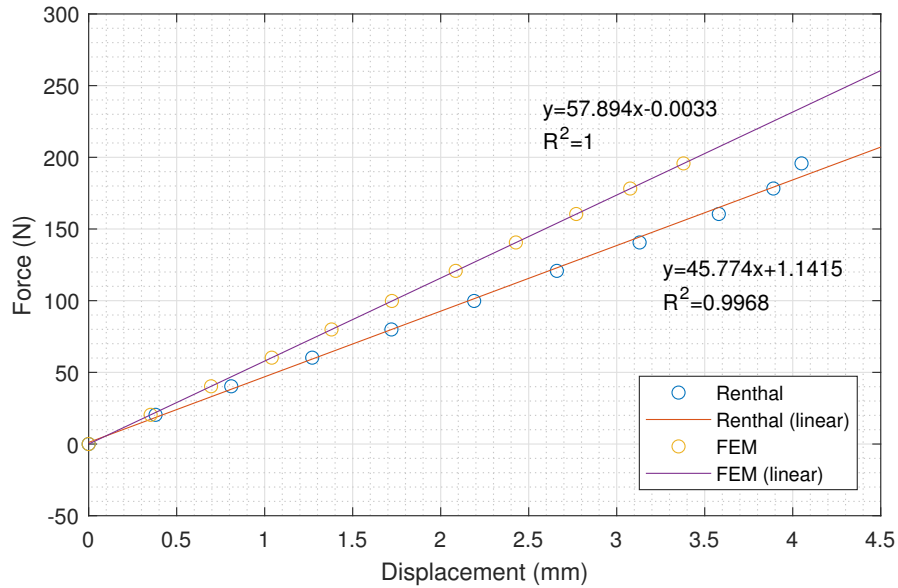


Figure 4.12: Plot of stiffness of the Renthal handlebar and the FEM model

Once more, the relative difference between experimental and FEM results was calculated.

$$\text{Relative Difference} = \frac{57.894 - 45.774}{57.894} = 20.9\% \quad (4.18)$$

As can be seen, the relative difference in both cases is similar, meaning that there is an approximately 20% difference in the value of flexural stiffness between the experimental setup and the FEM model. The FEM model has a higher stiffness than the experimental setup once the fixed support is infinitely rigid. Consequently, the natural frequencies in the FEM model will also be higher.

4.6 Flax Fibers in FEM

Initially, the objective was to develop a solution providing good performance and comfort, being the more sustainable as possible. For that, it was ideal to have a handlebar made only of flax fibers. If passed the structural requirements, the handlebar only made of flax fibers would be more comfortable due to the better damping properties of this material. Also, natural fibers like flax have a lower environmental impact than carbon fiber composites, aluminum, steel, and titanium which are the most common materials used in bike frames and handlebars nowadays. This way, the first step was to test many different cases in Ansys with Bcomp's flax fiber composites. Firstly, to better understand the influence of fiber orientation and the number of layers in the different sections, simulations on a cylindrical tube of 400 mm length were performed in Ansys. The handlebar has a 35 mm diameter bar clamp since the handlebar will be stiffer. For that reason, the handlebar with a 31.8 mm diameter wasn't considered at all. Many simulations considering different numbers of layers and different fiber orientations were performed. The boundary conditions in this analysis are a 1000 N load at the end of the handlebar and the fixed support in the middle of the handlebar (25 mm clamped) in agreement with the ISO 4210-5:2014 - Lateral bending test. The result analysis was carried out by taking into account the mass of the cylindrical aluminum tube with 1,5 mm thickness, the maximum displacement, and the safety factor. The following equation calculates the mass of a cylinder with a 35 mm diameter and a 1,5 mm thickness made of Aluminum 7050 T-7651.

$$\text{Mass} = \pi \cdot (R_{\text{ext}}^2 - R_{\text{int}}^2) \cdot l \cdot \rho = \pi \cdot \left(\left(\frac{0.035}{2} \right)^2 - \left(\frac{0.032}{2} \right)^2 \right) \cdot 0.4 \cdot 2830 = 0.17870 \text{ kg} \quad (4.19)$$

Figure 4.13 shows the geometry of the cylindrical tube in Ansys divided into five sections.

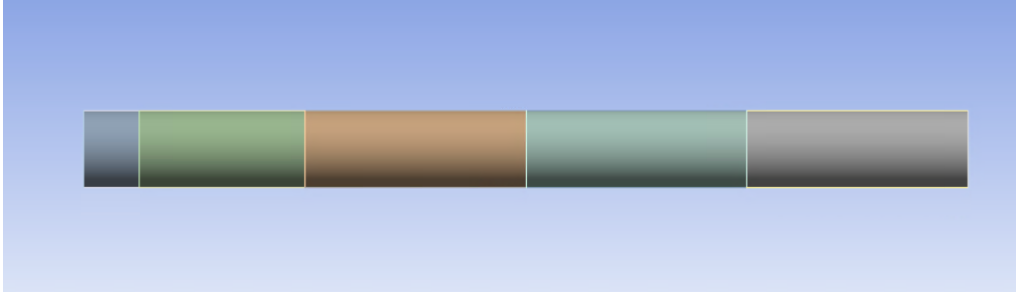


Figure 4.13: Geometry of the 35 mm diameter cylindrical tube

After some simulations it was concluded that:

- The best results were obtained when the unidirectional plies had a fiber orientation of 0°;
- The higher the number of layers, the higher the safety factor;
- The higher the number of layers, the higher the mass of the cylinder;
- The higher the number of layers, the stiffer the cylinder;
- Constant thickness all over the handlebar is not appropriate in terms of the mass and safety factor balance.

4. Numerical Results

A ply of woven flax fiber composite in the top is considered to restrict the number of simulations. Woven plies are generally more resistant to impacts, and the possibility of failure is reduced. The other plies are unidirectional. It is also important to say that the top is the first ply, and the number of layers increases inwards. The number of plies in the different sections can not be huge since it is not practical to have huge thicknesses in the handlebar. Table 4.24 presents some of the results accomplished in Ansys for a cylindrical tube of 400 mm made of flax fiber composites.

Table 4.24: Results for a cylindrical tube with a 35 mm diameter made of flax fibers

Nº of Layers	Mass (kg)	Max. Displacement (mm)	Safety Factor
15/15/15/15/15	0.20202	13.83	0.99
19/19/11/9/8	0.16401	15.73	0.88
19/19/15/9/8	0.17571	14.33	1.13
19/19/15/9/5	0.16481	14.76	1.13

The last case from Table 4.24 is the one with a lower mass and also has a higher safety factor. It is important to refer that the four criteria used in FEM to calculate the safety factor were the Maximum Stress, Maximum Strain, Tsai-Hill, and Tsi-Wu criterium. From the four criteria, the software shows the critical criterium for each element. The maximum thickness for this case is 4.25 mm. So the simulations with the handlebar geometry of flax fiber composites had these results as a reference. The geometry of the handlebar used in these simulations is the 35 mm diameter split geometry. This geometry has eleven sections, as represented in Figure 4.14.

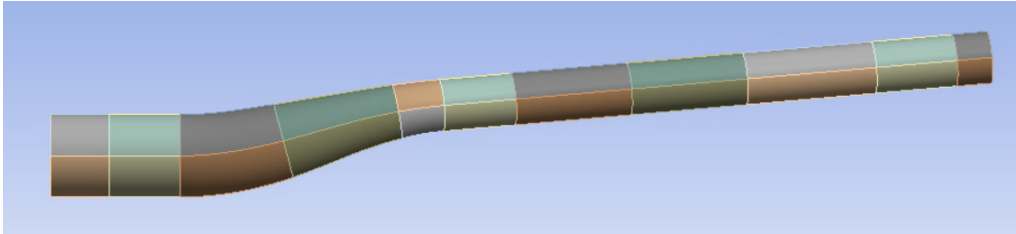


Figure 4.14: Split geometry of the 35 mm diameter handlebar

In the case of the handlebar, the fiber orientation of unidirectional plies was studied again since a 0° orientation in all plies might not be the best due to the more complex geometry. However, after some tests, it was concluded that the best results were once more obtained with the unidirectional plies with a fiber orientation of 0° . As for the top ply, the woven flax fibers were considered again. As in the cylindrical tube, the first ply is a woven flax fiber composite, and it is at the top. The remaining ones are unidirectional with a fiber orientation of 0° . The boundary conditions are those of ISO 4210-5:2014 - Lateral bending test being the load of 1000 N. Table 4.25 shows some results of the handlebar with flax fiber composites, where the number of plies was the same all over the handlebar.

Table 4.25: Results of a 35 mm diameter handlebar made of flax fibers and with the same number of plies all over the handlebar

N ^o of Layers	Mass (kg)	Max. Displacement (mm)	Displacement - 15 mm (mm)	Safety Factor
7	0.08106	52.88	48.45	0.35
14	0.14225	30.04	27.38	0.65
18	0.17721	25.05	22.78	0.76

As can be seen, the safety factor of the handlebar only made with flax fibers is too low, and the mass is already too high. Therefore, it was required to increase the number of plies in the critical zone and decrease it in the other zones. The critical zones are between sections 1 and 2 and in section 5. Besides, an important topic to address is the fact that the fatigue safety factor is not calculated for the handlebar made of flax fiber composites since the fatigue properties of this material are unknown. However, it should be noted that fiber-reinforced composites have been demonstrating a higher fatigue resistance than aluminum. The model was divided into four zones to ease the manufacturing process of the handlebar. The first zone consists of the first five sections of the geometry model, the second zone encompasses the 6th and 7th sections, the third zone covers the 8th and 9th sections, and finally, the fourth zone includes the 10th and 11th sections. Figure 4.15 shows the four zones of the handlebar.

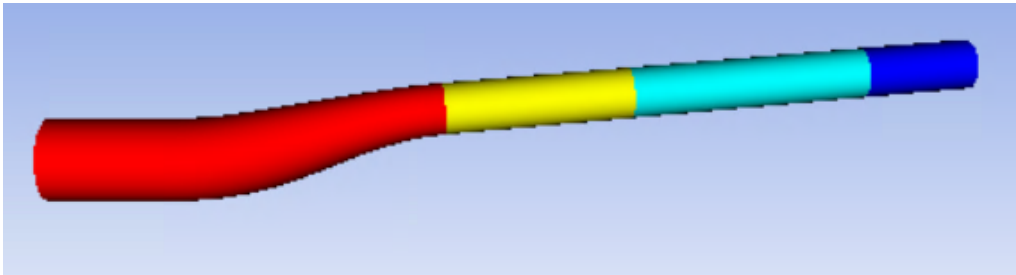


Figure 4.15: The division of the handlebar into four sections

Some simulations were performed, even though the results were not good. Table 4.26 shows the best case scenarios.

Table 4.26: Results of a 35 mm diameter handlebar made of flax fibers and with different number of plies

N ^o of Layers	Mass (kg)	Max. Displacement (mm)	Displacement - 15 mm (mm)	Safety Factor
20/15/9/5	0.15315	26.34	23.94	0.76
22/15/9/5	0.16193	25.52	23.19	0.77

As can be seen, the safety factor in the last case from Table 4.26 is low, and the mass is higher than Renthal's handlebar. Besides, the thickness in the critical zone is 4,85 mm, which is near the maximum limit previously defined, 5 mm. Moreover, the thickness of the different zones can not be very different because it is impracticable for manufacture. So the improvement margin was limited. Consequently, it was concluded that a handlebar only with flax fibers composite for a mountain bike does not accomplish the required

static requirements. So it was decided to consider a hybrid composite using carbon and flax fibers to increase the stiffness and the safety factor of the handlebar. Nevertheless, the addition of carbon fibers increases its environmental impact.

However, the static requirements could be reached if the objective of this work were to develop a handlebar for a city bike or a young adult since the load used to test the handlebar would be only 600 N and not 1000 N as in the mountain bikes, as reported in the ISO 4210-5:2014 - Lateral bending test. This way, some simulations were performed to verify if it is possible to have a city bike with a handlebar made only of flax fibers. As mentioned before, the handlebar must support a load of 600 N at 50 mm from its end for this type of bicycle. The other boundary condition is the fixed support in the middle of the handlebar, as has been considered in this work. Table 4.27 shows the results from three different simulations. The first ply is a flax fiber woven composite, and the remaining ones are unidirectional.

Table 4.27: Results for a 35 mm diameter handlebar made of flax fibers and with different number of plies for a city bike

N ^o of Layers	Mass (kg)	Max. Displacement (mm)	Displacement - 15 mm (mm)	Safety Factor
20/15/9/5	0.15315	15.81	14.37	1.26
21/15/9/6	0.15754	15.54	14.13	1.27
22/15/9/5	0.16193	15.31	13.91	1.28

Analyzing the results it is easy to conclude that for a city bike or a bike of a young adult is completely possible to have a handlebar with this geometry made only of flax fibers because the safety factor is higher than 1,25 and mass is lower or similar to Renthal's handlebar (first 2 situations). Also, the maximum thickness was from 4.45 mm and 4.65 mm for the first 2 situations and wasn't higher than the maximum limit of 5 mm that was defined.

4.7 Carbon and Flax Fiber Hybrid Composite Handlebar

As discussed before, it is impossible to have a mountain bike's handlebar only made of a flax fiber composite since the safety factor is low, and the handlebar would not reach the static requirements. Therefore the next step was to consider a hybrid composite in the handlebar. The material used was a hybrid composite with flax and carbon fibers. The objective of using a hybrid composite is to take advantage of the excellent stiffness-to-mass ratio and higher strength of the carbon fiber in combination with the damping capability of the natural fibers, in addition to the lower environmental impact of those natural fibers. Thus, the handlebar will meet the static requirements due to the use of carbon fibers and better damping properties due to flax fibers.

Hay [2015] use an outer layer of woven carbon fiber and justify it as an industry practice. The woven in the first ply is important because its strength is equal in both directions. This makes the first ply much more resistant to impacts. Additionally, if it was not a woven fabric, even a minor flaw in the ply may have disastrous effects on the handlebar. The use of carbon fiber composite in the first ply is better at a structural level. However, in this thesis, the first ply is a woven fabric with flax fibers. Impact resistance justifies the use of a woven fabric. The use of a flax fiber composite in the first ply serves

more as a design purpose than a structural one. If it was only for the structural function, the first ply would have to be of a carbon fiber composite.

Pil et al. [2016] stated that designers are fascinated with flax and hemp fibers not only because of their damping properties or the fact that are natural fibers but also because the appealing non-technical characteristics will lead to increasing use of flax and hemp fiber composites in consumer goods. This way, having a different design can also captivate more people. Besides, the fact that the first ply is of natural material can also have an impact on people that care about the environment. In such a manner, we must optimize the structure to reach the static requirements in order to gain at a design level. After the first ply, the next ones are from woven carbon fiber, giving the handlebar more stiffness and strength. After those plies, the remaining ones are unidirectional flax fiber plies. Placing flax fibers plies in the interior of the handlebar is important due to the fact that the interior plies are the ones that are more responsible for vibration damping once the shear strain is higher.

Many simulations were performed in the commercial software Ansys to find the best solution. At first, only woven carbon fiber composites with the same number of plies all over the handlebar were considered. The carbon fiber material that was used in FEM was the XC110 210g 2x2 Twill 3k Prepreg Carbon Fibre presented previously. Table 4.28 shows some of those results.

Table 4.28: Results of the handlebar with woven carbon fiber composite

N^o of Layers	Mass (kg)	Max. Displacement (mm)	Displacement - 15 mm (mm)	Safety Factor
8	0.07571	27.07	24.69	1.34
10	0.09464	22.25	20.28	1.62
12	0.11356	19.17	17.45	1.87
14	0.13249	17.05	15.51	2.08

After that, it was performed a simulation to understand the impact of using woven flax fiber in the first ply instead of woven carbon fiber. Table 4.29 presents the results.

Table 4.29: Results of the handlebar with woven carbon and flax fiber composites

N^o of Layers	Mass (kg)	Max. Displacement (mm)	Displacement - 15 mm (mm)	Safety Factor
14	0.15165	18.17	16.53	1.41

As can be seen, considering the first ply of woven flax fiber composite affects the safety factor enormously, decreasing from 2.08 to 1.41. After that, the objective was to change the interior plies from woven carbon fiber composite to unidirectional flax fibers until the safety factor reached a minimum of 1.25. Once more, it is also important to mention that the fatigue safety factor was not calculated due to unknown properties at that level. However, as already mentioned, the impact of fatigue in aluminum is much higher than in fiber-reinforced composites. Therefore the difference between both safety factors should be lower. Table 4.30 shows results from these simulations. The first case has woven flax fiber in the first ply and unidirectional flax fiber in the 14th ply. The next ones have one more unidirectional flax fiber ply from the inside to the outside than the previous case.

4. Numerical Results

Table 4.30: Results of the handlebar with woven carbon and flax fiber composites - increasing use of flax UD's

N ^o of Layers	Mass (kg)	Max. Displacement (mm)	Displacement - 15 mm (mm)	Safety Factor
14	0.15092	18.62	16.94	1.37
14	0.15020	19.11	17.40	1.33
14	0.14948	19.66	17.90	1.29
14	0.14876	20.28	18.47	1.25

As the safety factor was already 1.25, it was necessary to increase the number of plies in the critical zone and decrease it in the other zones to reduce the mass. The previous geometry considering eleven sections was divided into only three zones. In the following simulations, the first five sections had the same number of plies and, consequently, thickness. The same applies for sections 6-8, and for sections 9-11, the number of plies is the same inside each zone. These divisions considered in the handlebar were designed instead of using the eleven sections in the geometry to ease the handlebar's manufacturing process, in particular, the ply layup. Figure 4.16 presents the handlebar divided into three zones.

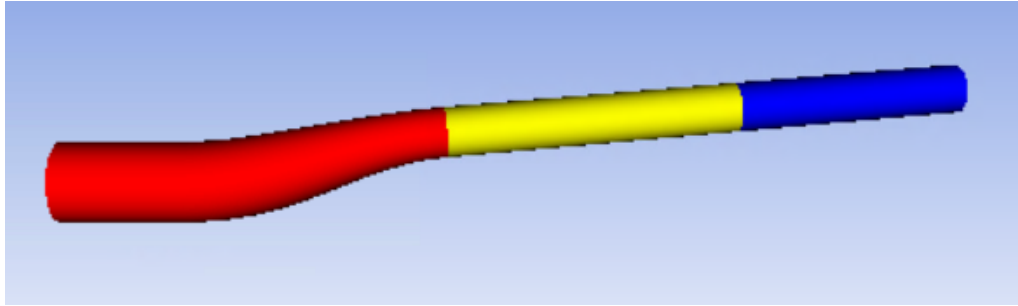


Figure 4.16: The division of the handlebar into three sections

Of the three zones, the more critical is the first one. So the number of plies in this zone must be increased, while in the other zones it can be decreased or not. Subsequently, the procedure was repeated, changing woven carbon fiber composite plies for unidirectional flax fiber composite plies until the safety factor was again 1.25. Table 4.31 shows the results of these simulations. In the first case, the first ply was woven flax fiber composite, and from the 11th ply, all other plies were unidirectional flax fiber composites. In the other case, the 10th ply was also changed to a unidirectional flax fiber ply.

Table 4.31: Results of the handlebar with woven carbon and flax fiber composites

N ^o of Layers	Mass (kg)	Max. Displacement (mm)	Displacement - 15 mm (mm)	Safety Factor
16/14/12	0.15365	19.62	17.87	1.28
16/14/12	0.15293	20.24	18.43	1.24

After that, many more simulations were carried out using the same procedure until reaching the best result - presented in Table 4.32. In this solution, the handlebar was divided into four zones, as before. The first zone encompasses the first five sections, the

second one the 6th and 7th sections, and the third one the 8th and 9th sections. Finally, the last zone includes the 10th and 11th sections. The first ply of this solution was also a woven flax fiber composite. All plies were from unidirectional flax fiber composite from the 8th to the 20th layer. The remaining plies were woven carbon fiber composite.

Table 4.32: Results of the best solution for the handlebar with carbon and flax fiber composites

N° of Layers	Mass (kg)	Max Displacement (mm)	Displacement - 15 mm (mm)	Safety Factor
20/15/9/6	0.15741	20.43	18.59	1.25

This is the best solution because of a safety factor of 1.25. The mass was very similar to Renthal's handlebar. Besides, the maximum thickness in the critical zone was 4.75 mm, which is acceptable. Some important factors were considered when the results of the simulations were analyzed. The safety factor and mass were the more important ones. The minimum limit of safety factor was 1.25, and the maximum limit of mass was near 157g for half of the handlebar (a value equal to Renthal's handlebar). Moreover, the maximum limit of thickness was defined as 5 mm. After that, some stiffness tests in the FEM model were performed for the same loads as the experimental flexural stiffness tests. Table 4.33 presents the displacement values for each load.

Table 4.33: Flexural stiffness test in FEM for the flax and carbon fiber composite handlebar

Load (N)	Displacement (mm)
0	0
20.39	0.38
40.28	0.75
60.25	1.12
79.92	1.49
99.80	1.86
120.79	2.25
140.60	2.61
160.46	2.98
178.23	3.31
195.76	3.64

Figure 4.17 presents the flexural stiffness plot.

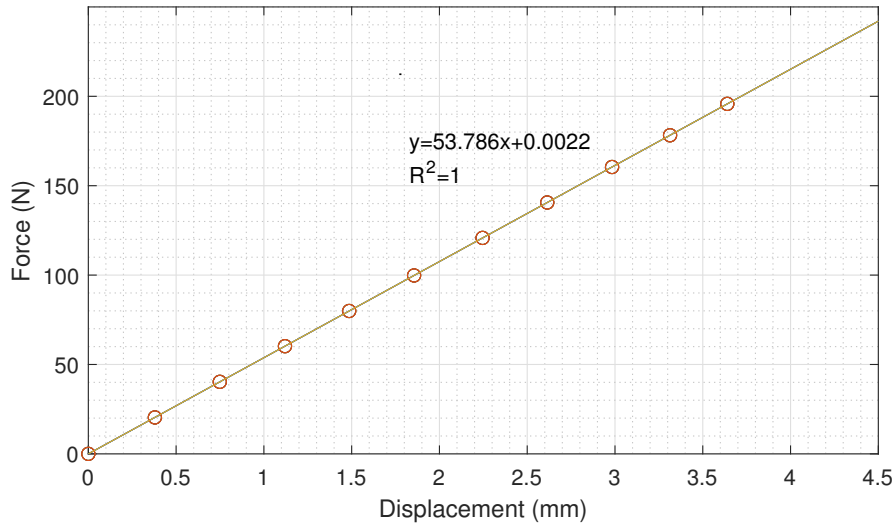


Figure 4.17: FEM analysis of the flexural stiffness for the flax and carbon fiber composite handlebar

As discussed before, it is expected some difference in flexural stiffness in real conditions. This way, considering a 20% relative difference, calculating the flexural stiffness for the experimental test gives 43.02N/mm. This flax and carbon fiber composite handlebar is more flexible when compared with commercial handlebars. However, this is not a big problem because OneUp has just released a carbon composite handlebar 20% more flexible than other carbon handlebars on the market. OneUp claims that a handlebar with a lower stiffness is more comfortable and causes less fatigue [Components, 2022].

Finally, another important parameter is the quantity of flax fiber plies used. The objective was to use the maximum percentage of flax fiber plies and the minimum carbon fiber plies. This way, the environmental impact of the handlebar is reduced even more and would make the handlebar more comfortable as a consequence of the better damping capacity of this material. Epoxy resin would be used as the matrix of flax and carbon fibers to manufacture this handlebar; Bcomp's flax fiber (woven and unidirectional) and woven carbon fiber composites are preregs. Epoxy is a thermoset. As previously mentioned, thermosets can not be recycled and have a higher environmental impact.

As previously mentioned, having the first ply of woven flax fiber is a design proposal. If the first ply is of woven carbon fiber composite, the safety factor would be higher, and the handlebar's mass would be lower. Therefore, a simulation switching the first ply from woven flax fiber to woven carbon fiber composite was also performed, and Table 4.34 presents the results.

Table 4.34: Results of the best solution for the handlebar with of carbon and flax fiber with a woven carbon ply at the top

Nº of Layers	Mass (kg)	Max. Displacement(mm)	Displacement - 15 mm (mm)	Safety Factor
20/15/9/5	0.13825	19.25	17.51	1.29

The difference in the safety factor is minimum. Therefore, using a woven flax fiber composite in the first ply is not as compromising as expected. However, the mass of the handlebar decreases, being the performance higher at this level. For this solution, the

flexural stiffness plot was computed for the same loads, using the vertical displacement values at 15 mm from the end of the handlebar. Table 4.35 presents the displacements for each load.

Table 4.35: Flexural stiffness test in FEM for the flax and carbon fiber handlebar with woven carbon fiber in the first ply

Load (N)	Displacement (mm)
0	0
20.39	0.36
40.28	0.71
60.25	1.06
79.92	1.40
99.80	1.75
120.79	2.12
140.60	2.46
160.46	2.81
178.23	3.12
195.76	3.43

Figure 4.18, presents the flexural stiffness plot obtained with FEM analysis.

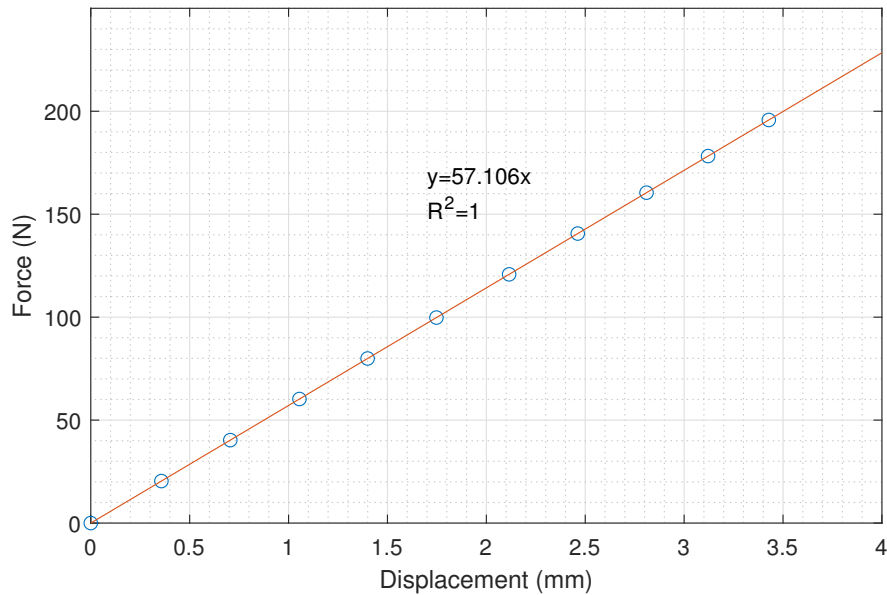


Figure 4.18: Flexural stiffness plot for the flax and carbon fiber composite handlebar with a woven carbon fiber in the first ply in FEM analysis

As can be seen, the flexural stiffness of this solution is higher than in the previous case and is similar to Renthal's handlebar. If this handlebar was experimentally tested, the flexural stiffness would have a relative difference of 20% and would be $45.7N/mm$.

4.8 Comparison of Results for Experimental Tests and FEM Model

As previously reported, the handlebars and the two cylindrical tubes were dynamically tested with the impact hammer technique. In this section, the results obtained with such tests are compared with the results obtained with the FEM model in Ansys.

4.8.1 Cylindrical Aluminum Tube (400 mm)

Figure 4.19 shows the point FRF_{10,10} of cylindrical tube (400 mm) and its FEM model.

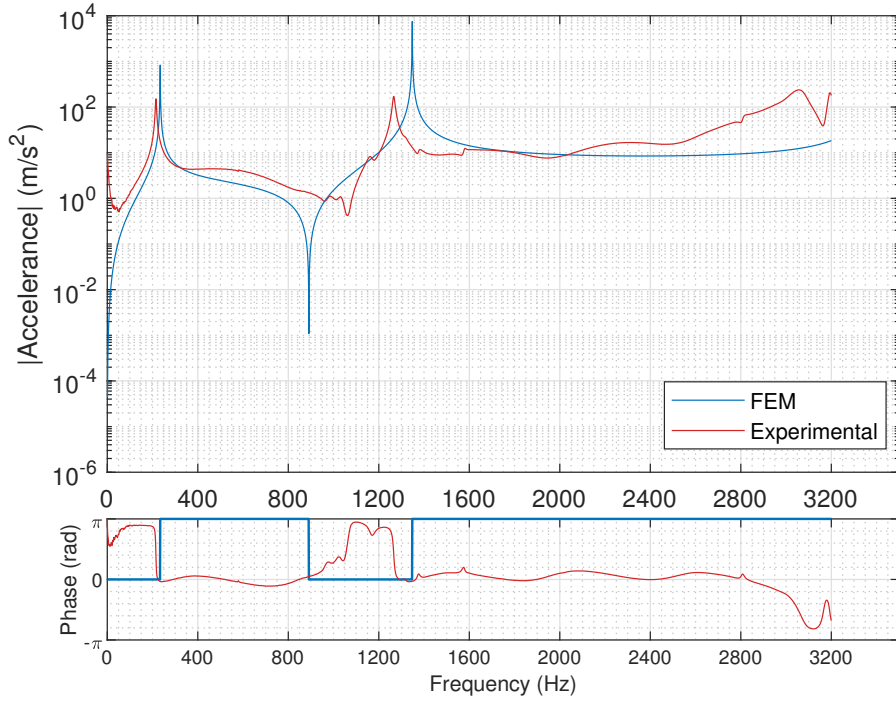


Figure 4.19: Point FRF_{10,10} of the cylindrical tube (400 mm) and its FEM model

As can be seen, both FRFs are similar, being the first two resonances easily identified. As previously discussed in chapter 3, the third resonance is not easily identifiable with this point FRF. However, in the FEM model, the third resonance only appears after the limit frequency of 3200 Hz and can not be seen in the FRF. This difference between the natural frequencies of the third mode is due to the stiffness differences between the experimental setup and the FEM model. The amplitude differs between the experimental tests and the FEM model. This happens because the FEM model was developed without including any damping mechanism. As discussed later, this is a feature to consider in future works. Table 4.36 shows the natural frequencies of the cylindrical tube (400 mm) and its FEM model.

Table 4.36: Natural frequencies (Hz) of the cylindrical tube (400 mm) and its FEM model

	Mode 1	Mode 2	Mode 3
Experimental	214.9	1270.9	2811.7
FEM	233.8	1347.8	3358.4

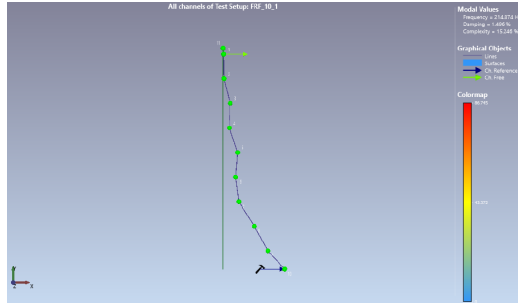
As expected, the natural frequencies of the cylindrical tube of 400 mm are lower than the FEM model. This happens since the FEM model is stiffer than reality because the fixed support is pure and perfect. Once more, calculating the relative difference for each natural frequency is possible to see that they never exceed 17%, which is lower than the relative difference in flexural stiffness. Table 4.37 shows the relative difference between the experimental and FEM model.

Table 4.37: Relative difference between the natural frequencies of the cylindrical tube (400 mm and FEM model

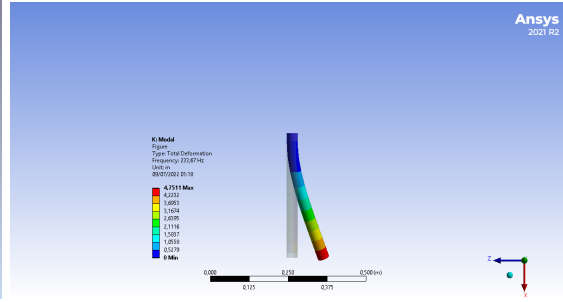
	Mode 1	Mode 2	Mode 3
Relative Difference (%)	8.0	5.7	16.3

The mode shapes of the cylindrical tube and its FEM model can also be compared for each mode. In Figure 4.20, it is possible to see the mode shapes obtained experimentally and those computed with Ansys.

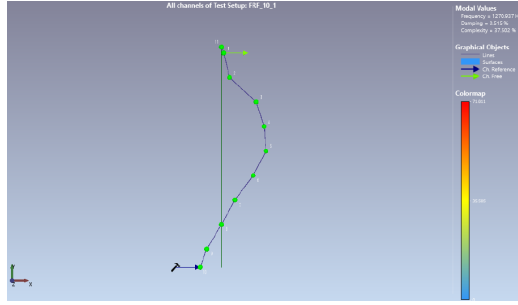
4. Numerical Results



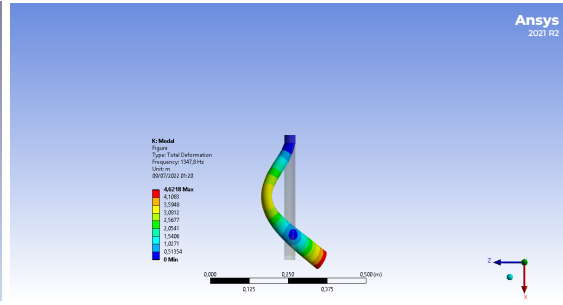
(a) Mode shape 1 - Cylindrical tube (400mm)



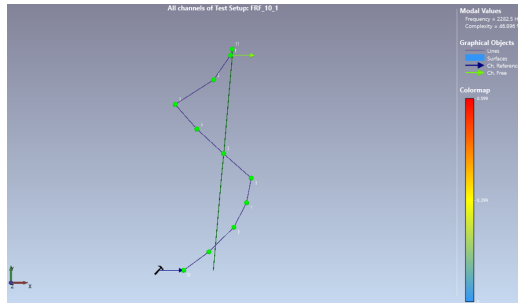
(b) Mode shape 1 - FEM



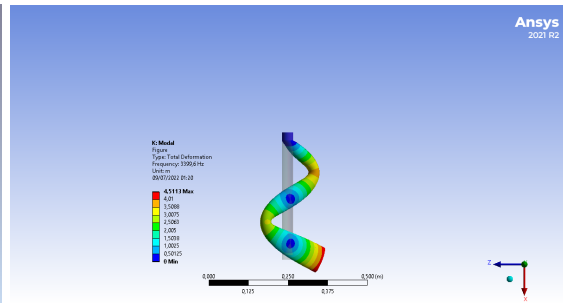
(c) Mode shape 2 - Cylindrical tube (400mm)



(d) Mode shape 2 - FEM



(e) Mode shape 3 - Cylindrical tube (400mm)



(f) Mode shape 3 - FEM

Figure 4.20: Mode shapes of the cylindrical tube (400 mm) and its FEM model

4.8.2 Cylindrical Aluminum Tube (775 mm)

Figure 4.21 shows the point FRF_{9,9} of the cylindrical tube (775 mm) and its FEM model.

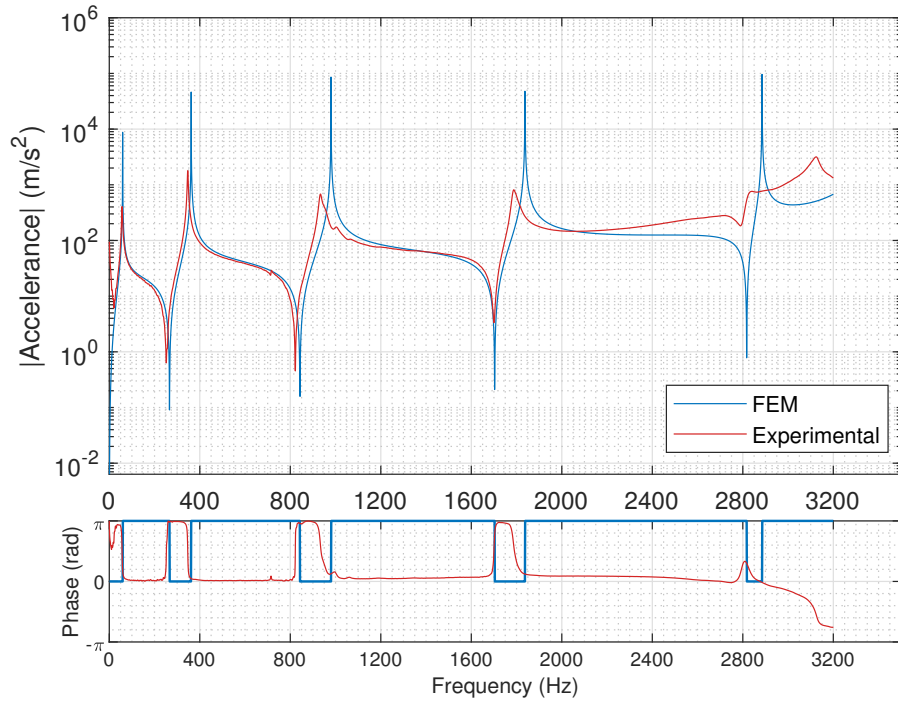


Figure 4.21: Point $FRF_{9,9}$ of the cylindrical tube (775 mm) and its FEM model

As can be seen, both FRFs are similar, being the first five resonances easily identified. Once more, the amplitude differences between the cylindrical tube (775 mm) and its FEM model are visible once the FEM model does not include any damping mechanism. Table 4.38 presents the natural frequencies of cylindrical tube (775 mm) and its FEM model.

Table 4.38: Natural frequencies (Hz) of the cylindrical tube (775 mm) and its FEM model

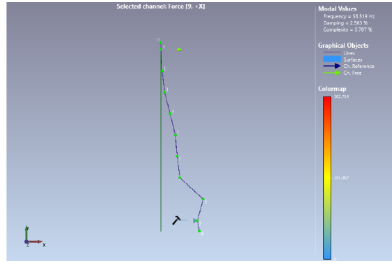
	Mode 1	Mode 2	Mode 3	Mode 4	Mode 5
Experimental	56.5	346.6	927.9	1795.1	2769.5
FEM	59.2	363.1	983.8	1845.2	2885.2

As expected, the natural frequencies of the cylindrical tube (775 mm) are lower than the FEM model. This happens because the FEM model, as previously discussed, is stiffer than reality since the fixed support is pure and perfect. Once more, calculating the relative difference for each frequency is possible to see that they never exceed 6%. Table 4.39 shows the relative difference between the experimental and FEM model.

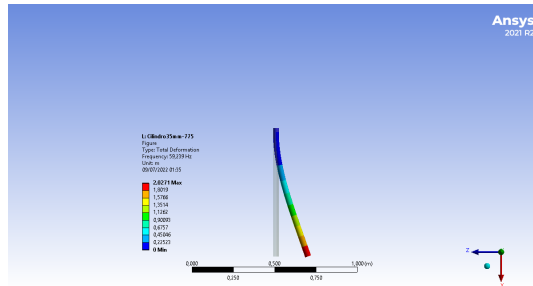
Table 4.39: Relative difference between natural frequencies of cylindrical tube (775 mm) and its FEM model

	Mode 1	Mode 2	Mode 3	Mode 4	Mode 5
Relative Difference (%)	4.6	4.6	5.7	2.7	4.0

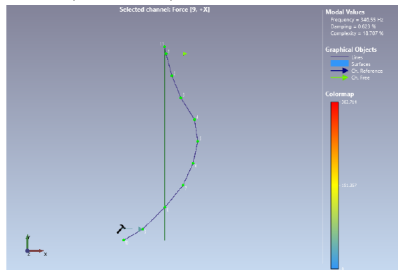
The mode shapes of the cylindrical tube (775 mm) and its FEM model can also be compared for each mode. In Figure 4.22, it is possible to see the first four mode shapes obtained experimentally and those computed with Ansys.



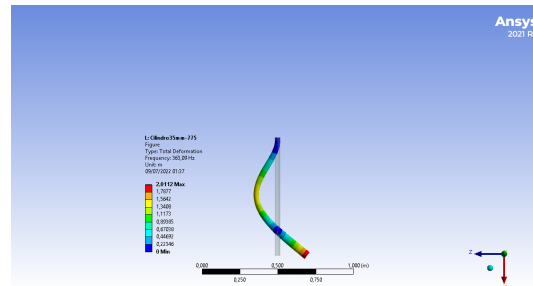
(a) Mode shape 1 - Cylindrical tube (775 mm)



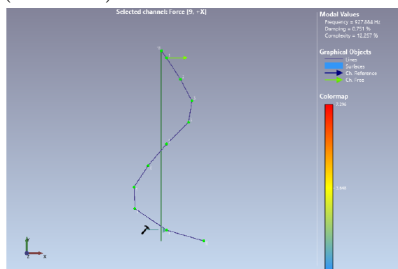
(b) Mode shape 1 - FEM



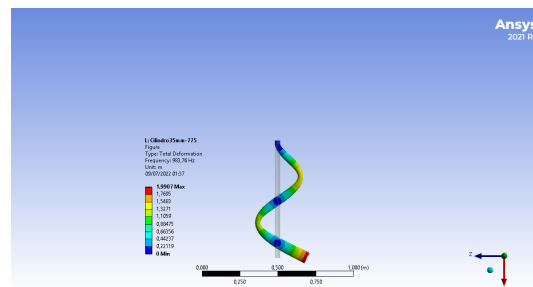
(c) Mode shape 2 - Cylindrical tube (775 mm)



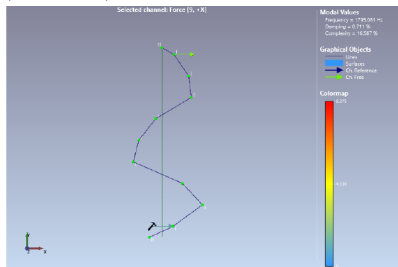
(d) Mode shape 2 - FEM



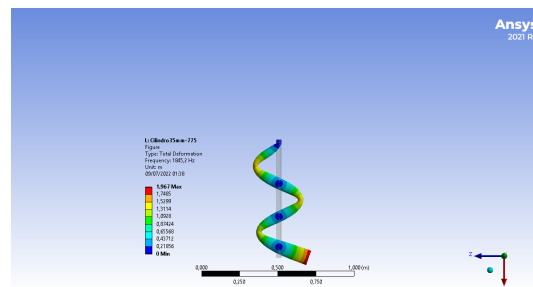
(e) Mode shape 3 - Cylindrical tube (775 mm)



(f) Mode shape 3 - FEM



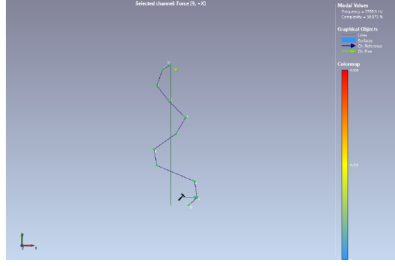
(g) Mode shape 4 - Cylindrical tube (775 mm)



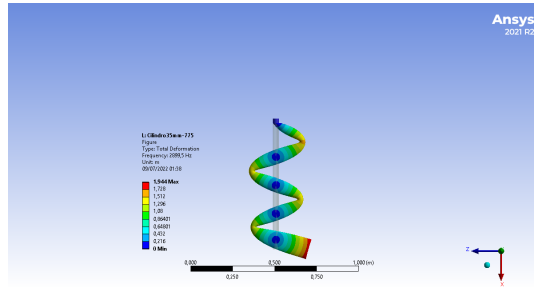
(h) Mode shape 4 - FEM

Figure 4.22: Mode shapes of the cylindrical tube (775 mm) and in its FEM model

In Figure 4.23, it is possible to see the fifth mode shape obtained experimentally and computed with Ansys.



(a) Mode shape 5 - Cylindrical tube (775 mm)



(b) Mode shape 5 - FEM

Figure 4.23: Mode shapes of the cylindrical tube (775 mm) and in its FEM model

4.8.3 Renthal's Handlebar

Figure 4.24 presents the point FRF_{10,10} of the Renthal's handlebar and the corresponding FEM model.

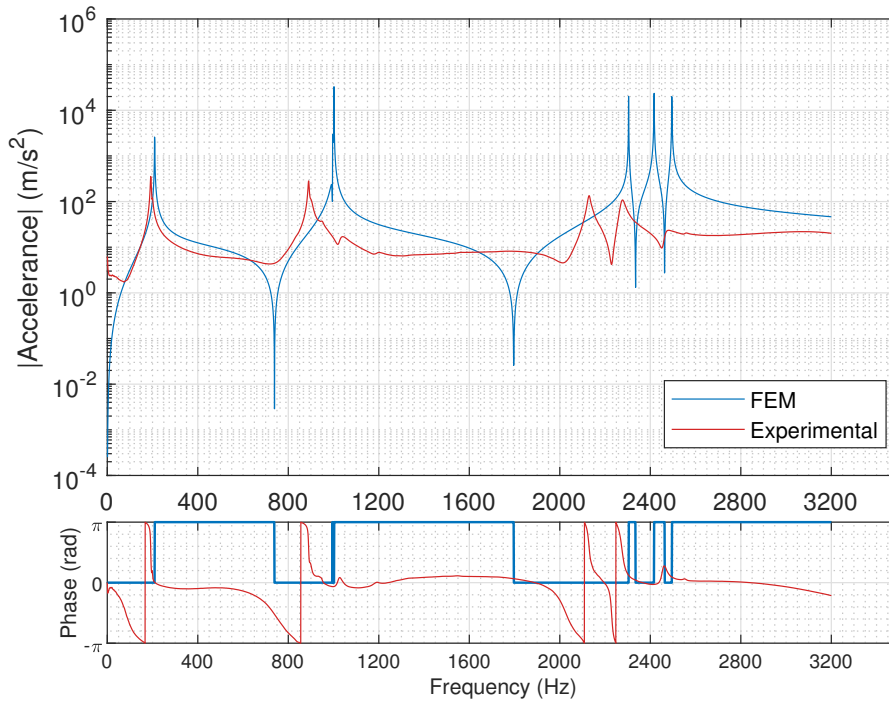


Figure 4.24: Point FRF_{10,10} of the Renthal's handlebar and of its FEM model

As can be seen, both FRFs are similar, being the first three resonances easily identified. Once again, the amplitudes in the FEM model are higher. Table 4.40 shows the first three natural frequencies of the Renthal's handlebar obtained experimentally and those computed with the FEM model.

Table 4.40: Natural frequencies (Hz) of the Renthall's handlebar and the FEM model

	Mode 1	Mode 2	Mode 3
Experimental	192.5	891.0	2282.5
FEM	209.4	996.4	2416.6

As expected, the natural frequencies of Renthall's handlebar are lower than the FEM model. This happens because the FEM model, as previously discussed, is stiffer than the experimental setup since the fixed support is pure and perfect. Calculating the relative difference for each natural frequency, it is possible to conclude that they never exceed 11%. Table 4.41 presents the relative difference between the natural frequencies identified experimentally and those obtained with the FEM model.

Table 4.41: Relative difference between natural frequencies of Renthall's handlebar and FEM model

	Mode 1	Mode 2	Mode 3
Relative Difference (%)	8.2	10.6	5.5

The mode shapes of Renthall's handlebar and its FEM model can also be compared for each mode. In Figure 4.25, it is possible to see the mode shapes obtained experimentally and those computed with Ansys.

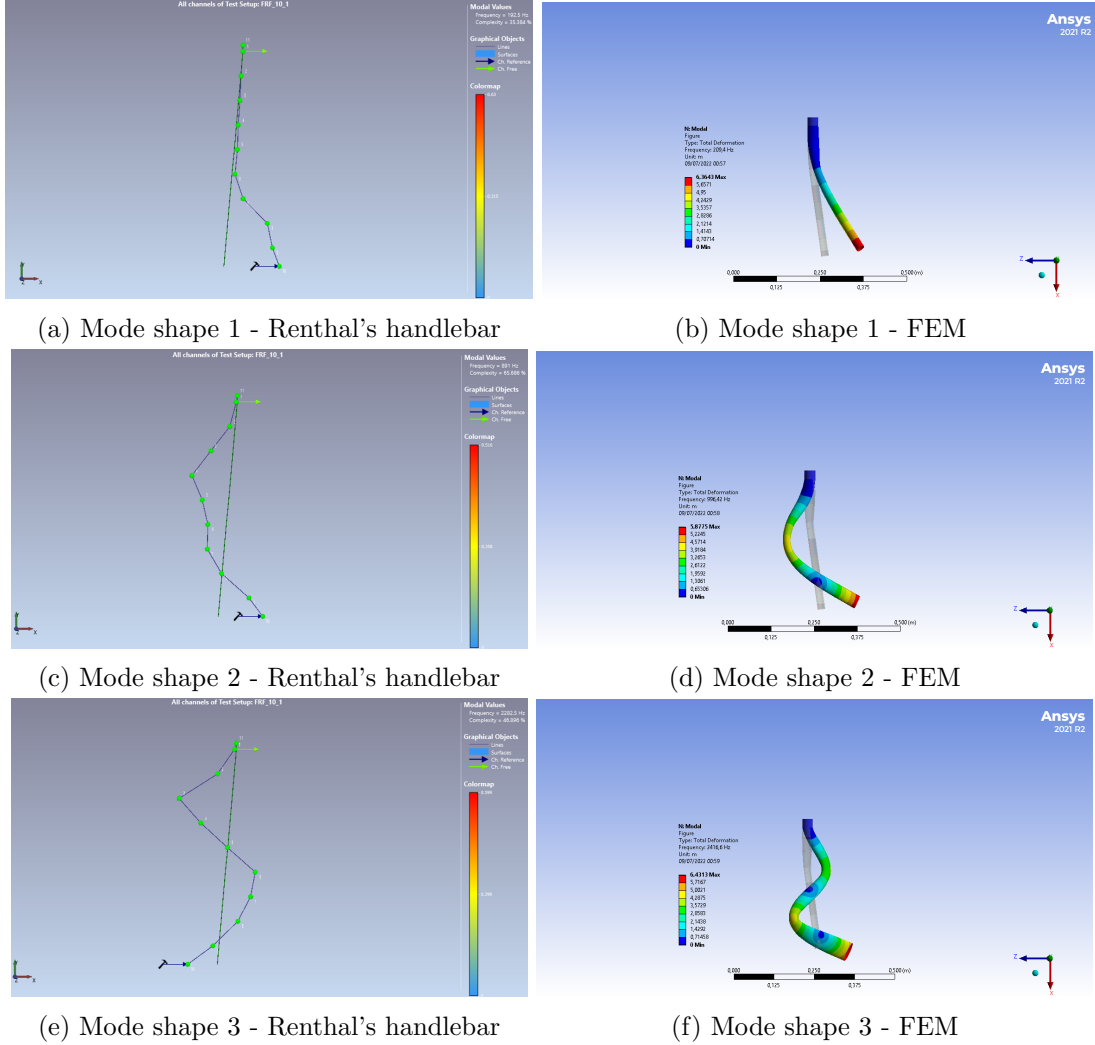


Figure 4.25: Mode shapes of the Renthal's handlebar and its FEM model

4.9 Dynamic Tests - FEM

The results from dynamic tests made in the commercial software Ansys are presented in this section.

4.9.1 Carbon Fiber Composite Handlebar

The first case considers a carbon fiber composite handlebar with 12 plies all over the handlebar with constant thickness. This carbon fiber composite handlebar can be compared to the OneUp's handlebar because they have similar mass and are both made of carbon fiber composite. In Figure 4.26, it is possible to see the point FRF obtained in Ansys being the point of impact at 15 mm from the end of the handlebar as in the other tests. The frequency range is 0 to 3200 Hz. The frequency resolution is 8 Hz because decreasing it would take too long for the simulation to run.

In the point FRF, it is possible to identify the first three resonances and one anti-resonance between each pair of resonances as expected. Table 4.42 shows the natural

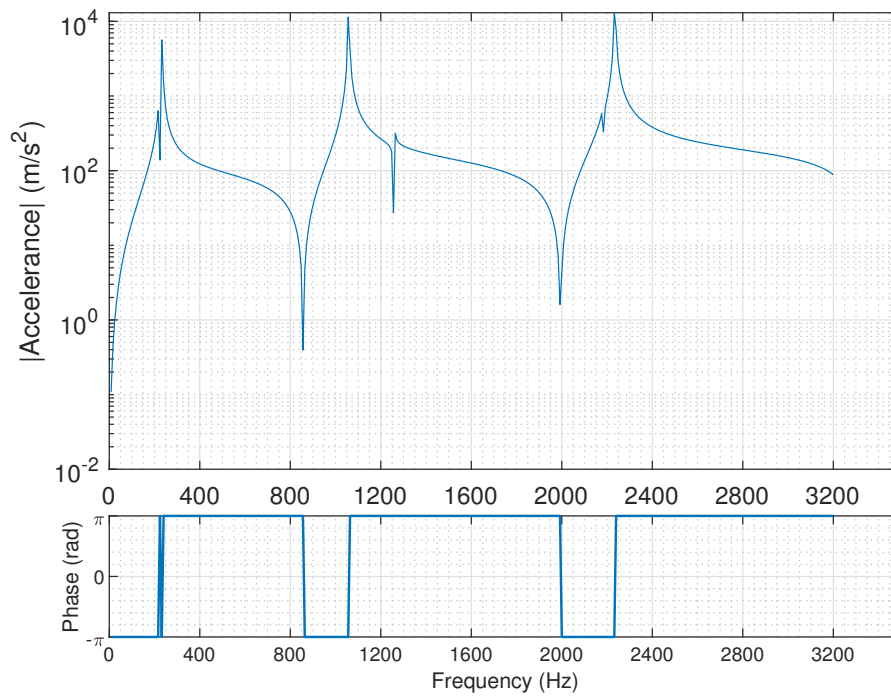


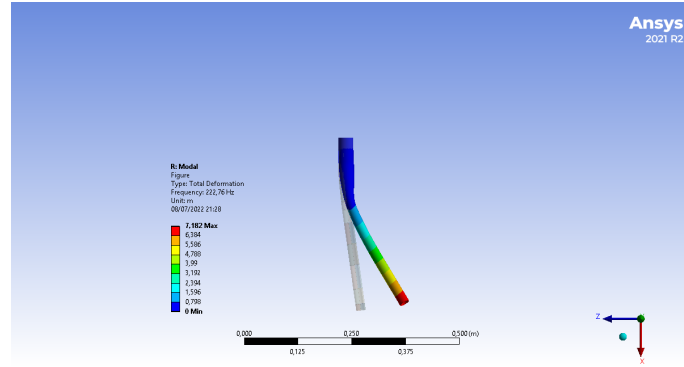
Figure 4.26: Point FRF of the carbon fiber composite handlebar in FEM

frequencies calculated by the software Ansys and obtained experimentally for the OneUp's handlebar.

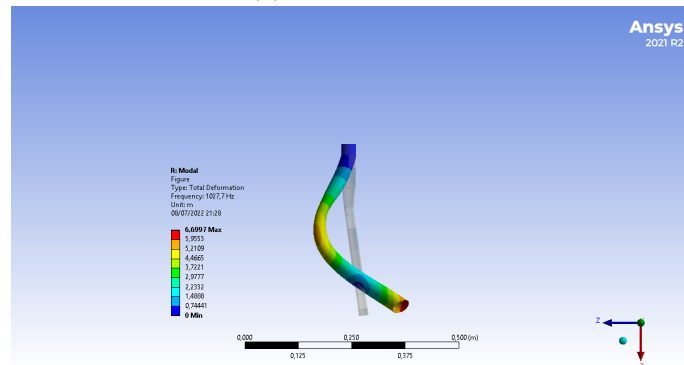
Table 4.42: Natural frequencies (Hz) obtained in Ansys for the carbon fiber composite handlebar and obtained experimentally for the OneUp's handlebar

Geometry	Mode 1	Mode 2	Mode 3
Carbon Fiber Composite Handlebar (FEM)	222.8	1027.7	2182.2
OneUp	263.5	1265.5	2837.0

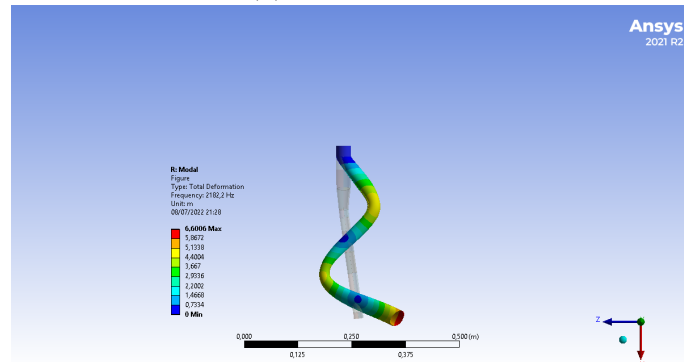
The natural frequencies are lower than OneUp's handlebar as expected because this handlebar is more flexible. In Figure 4.27 can be seen the first three mode shapes obtained in FEM analysis.



(a) Mode shape 1



(b) Mode shape 2



(c) Mode shape 3

Figure 4.27: Mode shapes obtained in FEM for the carbon fiber composite handlebar

4.9.2 Flax and Carbon Fiber Composite Handlebar

The final solution of this work, the hybrid composite handlebar with flax and carbon fibers, was also tested in FEM. Figure 4.28 presents the point FRF obtained in Ansys, being the point of impact 15 mm from the end of the handlebar as in the other tests.

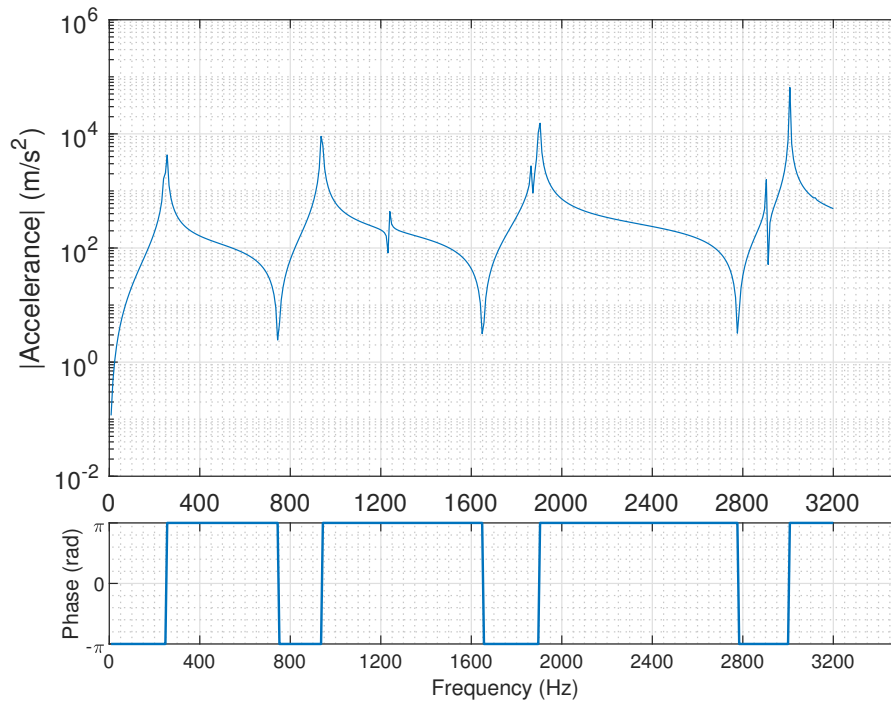


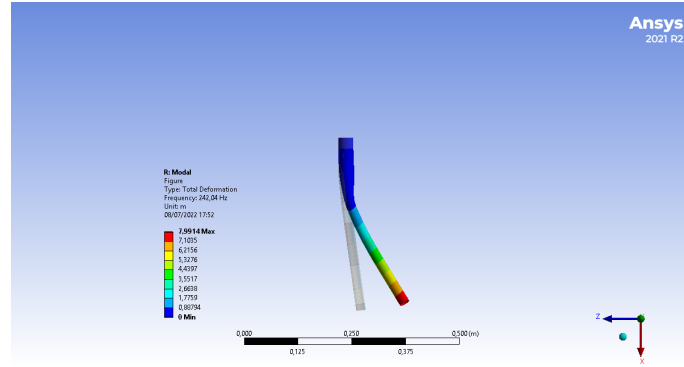
Figure 4.28: Point FRF for the flax and carbon fiber composite handlebar in FEM

In the point FRF, it is possible to identify the first four resonances and one anti-resonance between each pair of resonances, as expected. Table 4.43 shows the natural frequencies calculated by the software Ansys.

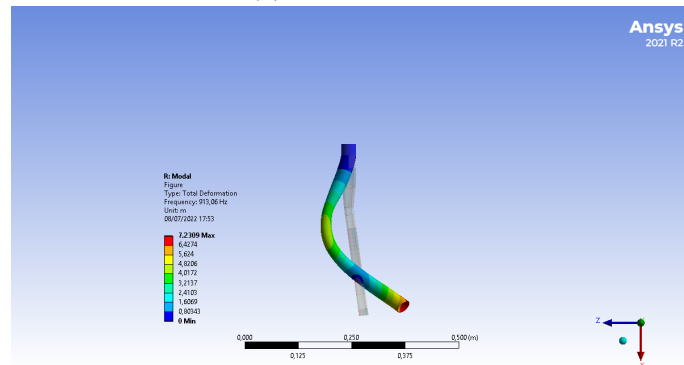
Table 4.43: Natural frequencies (Hz) obtained in Ansys for a flax and carbon composite fiber handlebar

Mode 1	Mode 2	Mode 3	Mode 4
242.0	913.0	1866.3	3118.9

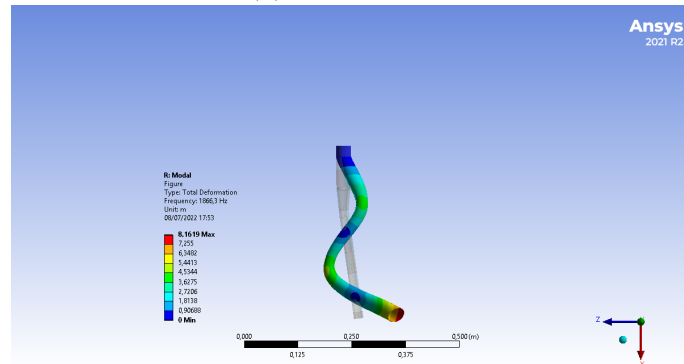
As expected, the natural frequencies are lower than OneUp's handlebar because this handlebar is more flexible. Comparing this flax and carbon handlebar with the carbon handlebar, the natural frequencies are lower, except for the first one. As this handlebar is more flexible, it was expected the same for all natural frequencies. Figure 4.29 presents the first four mode shapes.



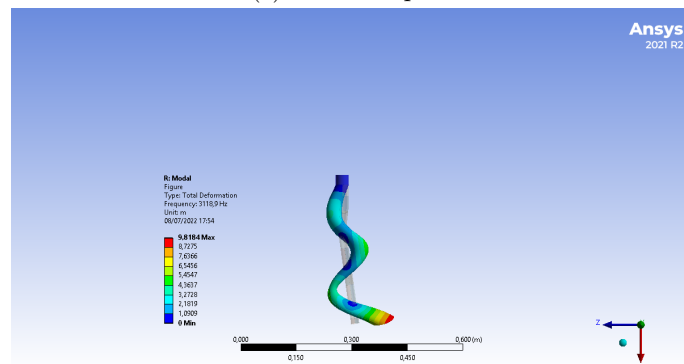
(a) Mode shape 1



(b) Mode shape 2



(c) Mode shape 3



(d) Mode shape 4

Figure 4.29: Mode shapes obtained in FEM for the flax and carbon fiber composite handlebar

4.9.3 Flax Fiber Composite Handlebar

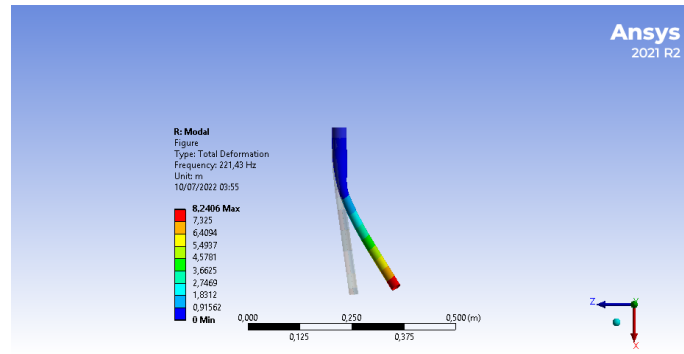
Finally, the best solution presented before for the handlebar only made of flax fiber composite is also analyzed. In this case, the FRF could not be obtained in Ansys. However, the natural frequencies and the mode shapes were obtained and presented. Table 4.44 shows the natural frequencies calculated by the software Ansys.

Table 4.44: Natural frequencies (Hz) obtained in Ansys for a flax fiber composite handlebar

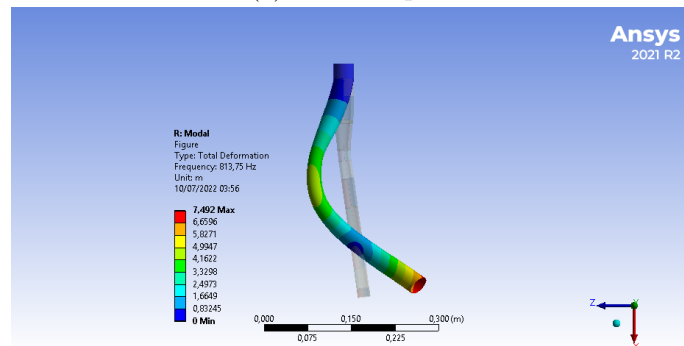
Mode 1	Mode 2	Mode 3	Mode 4
221.43	813.75	1630.5	2696.3

As expected, the natural frequencies of this handlebar are lower than the flax and carbon fiber composite handlebar and the carbon fiber composite handlebar. The reason for this is that this handlebar is less stiff than all the others.

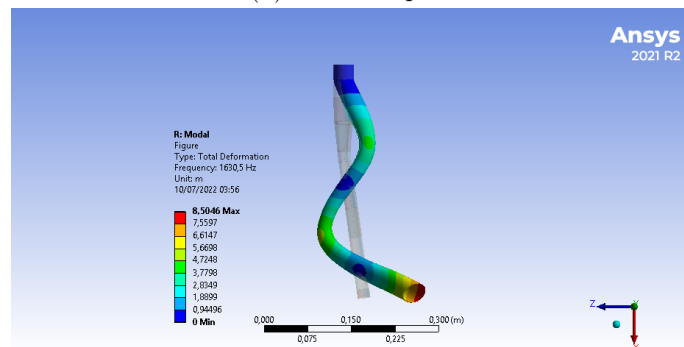
Figure 4.30 presents the first four mode shapes.



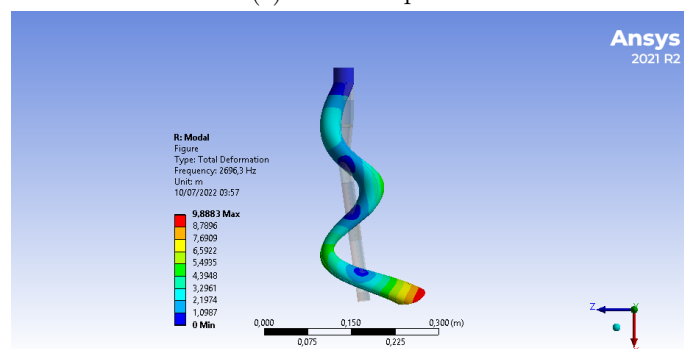
(a) Mode shape 1



(b) Mode shape 2



(c) Mode shape 3



(d) Mode shape 4

Figure 4.30: Mode shapes obtained in FEM for the flax fiber composite handlebar

Conclusion

5.1 Conclusions

This section is dedicated to reporting the conclusions of this work developing the flax and carbon fiber composites handlebar as:

- There is a relative difference of about 20% between the experimental setup used for the flexural stiffness tests and FEM analysis;
- The damping in carbon fiber composite handlebars is better than in aluminum handlebars;
- It is not possible to have a mountain bike's handlebar only made of flax fiber composites with the geometry that was considered in this work;
- It is possible to have a city bike's handlebar only made of flax fiber composites with the geometry that was considered in this work;
- The solution presented in this work is a good candidate because the comfort and environmental impact were the most important, even without discarding performance.

5.2 Future Work

Since the time allotted to do this work is short, there were many topics regarding this theme that could not be studied in detail. In this section, the goal is to point out some topics that can be studied in the future to improve the work presented here. The suggestions for future work are:

- Study different geometries from the considered one to find the best geometry to achieve even better results for the handlebar;
- Study the influence of the fiber orientation of unidirectional plies on the damping capacity;
- Study the damping in carbon and flax fiber reinforced composites and introduce it in the FEM model;
- Manufacture a handlebar prototype with flax and carbon fiber composites. Perform the stiffness and dynamic tests to check if the results would be as expected;
- Develop a flax fiber composite with a thermoplastic matrix to reduce the environmental impact of the handlebar.

References

- Steel Vs Aluminum Bike Frame: Pros and Cons, 2022. URL <https://wheretheroadforks.com/steel-vs-aluminum-bike-frame-pros-and-cons/>.
- Alltricks. How to choose your MTB handlebar, 2022. URL <https://www.alltricks.com/surl/mtb-handlebars>.
- Amazon. EC90 MTB Bicycle Handlebar Carbon Fiber High Strength Super Light Riser Steering Wheel Mountain Bike Parts 660/700/720/740/760 Bike Accessories, 2022. URL <https://www.amazon.de/EC90-Fahrradlenker-Festigkeit-Lenkrad-Mountainbike/dp/B07GB4V3HM?th=1>.
- Ali Amiri, Taylor Krosbakken, William Schoen, Dennis Theisen, and Chad A. Ulven. Design and manufacturing of a hybrid flax/carbon fiber composite bicycle frame. *Proceedings of the Institution of Mechanical Engineers, Part P: Journal of Sports Engineering and Technology*, 232(1):28–38, 2018. ISSN 1754338X. doi: 10.1177/1754337117716237.
- Christophe Baley, Alain Bourmaud, and Peter Davies. Eighty years of composites reinforced by flax fibres: A historical review. *Composites Part A: Applied Science and Manufacturing*, 144:106333, 2021. ISSN 1359835X. doi: 10.1016/j.compositesa.2021.106333. URL <https://doi.org/10.1016/j.compositesa.2021.106333>.
- Bcomp. McLaren Goes Racing With Bcomp, 2022. URL <https://www.bcomp.ch/news/mclaren-goes-racing-with-bcomp/>.
- Flow Mountain Bike. Yeti 160E First Look | Flow weighs in on Yeti’s long awaited e-MTB, 2022. URL <https://flowmountainbike.com/post-all/new-gear-bikes/yeti-160e-first-look/>.
- Bike-Components. OneUp Components 20 mm 35 Carbon Riser Handlebars, 2022. URL <https://www.bike-components.de/en/OneUp-Components/20-mm-35-Carbon-Riser-Handlebars-p70949/>.
- Bike24. Renthal Fatbar V2 Riser Handlebar - 800mm - black, 2022. URL <https://www.bike24.com/p2272792.html>.
- P. Camanho. FAILURE CRITERIA FOR FIBRE-REINFORCED POLYMER COMPOSITES. *Failure Criteria in Fibre-Reinforced-Polymer Composites*, (Figure 1):1–1255, 2002. doi: 10.1016/B978-0-080-44475-8.X5000-8. URL [https://web.fe.up.pt/\\$sim\\$stpinho/teaching/feup/y0506/fcriteria.pdf](https://web.fe.up.pt/simstpinho/teaching/feup/y0506/fcriteria.pdf).
- Y. Champoux, S. Richard, and J. M. Drouet. Bicycle structural dynamics. *Sound and Vibration*, 41(7):16–24, 2007. ISSN 15410161.

REFERENCES

- R. Chandra, S. P. Singh, and K. Gupta. Damping studies in fiber-reinforced composites - a review. *Composite Structures*, 46(1):41–51, 1999. ISSN 02638223. doi: 10.1016/S0263-8223(99)00041-0.
- Khouloud Cheour, Mustapha Assarar, Daniel Scida, Rezak Ayad, and Xiao Lu Gong. Effect of water ageing on the mechanical and damping properties of flax-fibre reinforced composite materials. *Composite Structures*, 152:259–266, 2016. ISSN 02638223. doi: 10.1016/j.compstruct.2016.05.045. URL <http://dx.doi.org/10.1016/j.compstruct.2016.05.045>.
- OneUp Components. The Most Compliant E-Bike Rated Bar On the Market, 2022. URL <https://www.oneupcomponents.com/collections/handlebars/products/e-carbon-handlebar>.
- Composites Construction UK. Carbon Fibre Reinforced Polymer: Pros & Cons, 2022. URL <https://www.fibrwrap-ccuk.com/blog/carbon-fibre-reinforced-polymer-pros-cons/>.
- Hajer Daoud, Abderrahim El Mahi, Jean Luc Rebière, Mohamed Taktak, and Mohamed Haddar. Characterization of the vibrational behaviour of flax fibre reinforced composites with an interleaved natural viscoelastic layer. *Applied Acoustics*, 128:23–31, 2017. ISSN 1872910X. doi: 10.1016/j.apacoust.2016.12.005. URL <http://dx.doi.org/10.1016/j.apacoust.2016.12.005>.
- Jonathan Dorey and Catherine Guastavino. Moving forward: Conceptualizing comfort in information sources for enthusiast cyclists. *Proceedings of the ASIST Annual Meeting*, 48, 2011. ISSN 15508390. doi: 10.1002/meet.2011.14504801187.
- F. Duc, P. E. Bourban, C. J.G. Plummer, and J. A.E. Månson. Damping of thermoset and thermoplastic flax fibre composites. *Composites Part A: Applied Science and Manufacturing*, 64:115–123, 2014. ISSN 1359835X. doi: 10.1016/j.compositesa.2014.04.016. URL <http://dx.doi.org/10.1016/j.compositesa.2014.04.016>.
- Engineering Learn. 15 Types of Handlebars for Bikes and Motorcycles, 2022. URL <https://engineeringlearn.com/types-of-handlebars-for-bikes-motorcycles/>.
- A. Etaati, S. Abdanan Mehdizadeh, H. Wang, and S. Pather. Vibration damping characteristics of short hemp fibre thermoplastic composites. *Journal of Reinforced Plastics and Composites*, 33(4):330–341, 2014. ISSN 07316844. doi: 10.1177/0731684413512228.
- V. Fiore, A. Valenza, and G. Di Bella. Mechanical behavior of carbon/flax hybrid composites for structural applications. *Journal of Composite Materials*, 46(17):2089–2096, 2012. ISSN 00219983. doi: 10.1177/0021998311429884.
- International Organization for Standardization. ISO 4210-5:2014 Cycles — Safety requirements for bicycles — Part 5: Steering test methods. URL <https://www.iso.org/standard/59912.html>.
- Ying Gao, Yibin Li, Yi Hong, Hongming Zhang, and Xiaodong He. Modeling of the damping properties of unidirectional carbon fibre composites. *Polymers and Polymer Composites*, 19(2-3):119–122, 2011. ISSN 14782391. doi: 10.1177/0967391111019002-311.
- Mayank Gautam. Hybrid composite wires for tensile armour in flexible risers. (September), 2001. URL <http://search.ebscohost.com/login.aspx?point=true&db=ddu&AN=0BCAEC5B4A3F5096&site=ehost-live>.

- R. F. Gibson, S. K. Chaturvedi, and C. T. Sun. Complex moduli of aligned discontinuous fibre-reinforced polymer composites. *Journal of Materials Science*, 17(12):3499–3509, 1982. ISSN 00222461. doi: 10.1007/BF00752195.
- Olgun Güven, Sergio N. Monteiro, Esperidiana A.B. Moura, and Jaroslaw W. Drelich. Re-Emerging Field of Lignocellulosic Fiber – Polymer Composites and Ionizing Radiation Technology in their Formulation. *Polymer Reviews*, 56(4):702–736, 2016. ISSN 15583716. doi: 10.1080/15583724.2016.1176037. URL <http://dx.doi.org/10.1080/15583724.2016.1176037>.
- A. S. Hadi and J. N. Ashton. Measurement and theoretical modelling of the damping properties of a uni-directional glass/epoxy composite. *Composite Structures*, 34(4):381–385, 1996. ISSN 02638223. doi: 10.1016/0263-8223(96)00005-0.
- K Hay. Dynamic Properties of Hybrid Composite Hollow Cylinders: Application for Mountain Bicycle Handlebars. Master’s thesis, McGill University, Montreal, 2015.
- Hopetech. Hope Technology: Making of Carbon Handlebars, 2022. URL <https://www.youtube.com/watch?v=0bKgD1ECXE8>.
- Zhenhua Hou, Ruiying Luo, Wei Yang, Huaizhe Xu, and Tao Han. Effect of interface type on the static and dynamic mechanical properties of 3D braided SiCf/SiC composites. *Materials Science and Engineering A*, 669:66–74, 2016. ISSN 09215093. doi: 10.1016/j.msea.2016.05.080. URL <http://dx.doi.org/10.1016/j.msea.2016.05.080>.
- Innovative Composite Engineering. What Is Carbon Fiber?, 2022. URL <https://www.innovativecomposite.com/what-is-carbon-fiber/>.
- Shuguang Li. The maximum stress failure criterion and the maximum strain failure criterion: Their unification and rationalization. *Journal of Composites Science*, 4(4), 2020. ISSN 2504477X. doi: 10.3390/jcs4040157.
- S. Mahmoudi, A. Kervoelen, G. Robin, L. Duigou, E. M. Daya, and J. M. Cadou. Experimental and numerical investigation of the damping of flax–epoxy composite plates. *Composite Structures*, 208(October 2018):426–433, 2019. ISSN 02638223. doi: 10.1016/j.compstruct.2018.10.030. URL <https://doi.org/10.1016/j.compstruct.2018.10.030>.
- Paul Norman. Bike frame materials explained: carbon vs aluminium vs steel vs titanium, 2022. URL <https://www.bikeradar.com/advice/buyers-guides/bike-frame-materials/>.
- Soo Jin Park. History and structure of carbon fibers. *Springer Series in Materials Science*, 210:1–30, 2018. ISSN 0933033X. doi: 10.1007/978-981-13-0538-2_1.
- Eustathios Petinakis, Long Yu, George Simon, and Katherine Dean. *Natural Fibre Bio-Composites Incorporating Poly(Lactic Acid)*, pages 41–58. 01 2013. ISBN 978-953-51-0938-9. doi: 10.5772/52253.
- Lut Pil, Farida Bensadoun, Julie Pariset, and Ignaas Verpoest. Why are designers fascinated by flax and hemp fibre composites? *Composites Part A: Applied Science and Manufacturing*, 83:193–205, 2016. ISSN 1359835X. doi: 10.1016/j.compositesa.2015.11.004. URL <http://dx.doi.org/10.1016/j.compositesa.2015.11.004>.

REFERENCES

- Claude Pineau. The psychological meaning of comfort. *Applied Psychology*, 31(2):271–282, 1982. ISSN 14640597. doi: 10.1111/j.1464-0597.1982.tb00097.x.
- Pinkbike. How Bike Handlebars Are Made, 2022. URL <https://www.youtube.com/watch?v=EICpmw1avR4>.
- R2-bike. RENTHAL Bar Fatbar Riser V2 31,8 x 800 mm | 7° | black 20 mm Rise, 2022. URL <https://r2-bike.com/RENTHAL-Bar-Fatbar-Riser-V2-318-x-800-mm-7-black-20-mm-Rise>.
- Md Zillur Rahman. Mechanical and damping performances of flax fibre composites – A review. *Composites Part C: Open Access*, 4(October 2020):100081, 2021. ISSN 26666820. doi: 10.1016/j.jcomc.2020.100081. URL <https://doi.org/10.1016/j.jcomc.2020.100081>.
- Md Zillur Rahman, Krishnan Jayaraman, and Brian Richard Mace. Vibration damping of flax fibre-reinforced polypropylene composites. *Fibers and Polymers*, 18(11):2187–2195, 2017. ISSN 12299197. doi: 10.1007/s12221-017-7418-y.
- José Dias Rodrigues. Identificação do amortecimento: Circular curve fitting. Technical report, FEUP, 2015.
- José Dias Rodrigues. *Apontamentos de Vibrações de Sistemas Mecânicos*. Faculdade de Engenharia da Universidade do Porto, PORTO, 2020 edition, 2020.
- Ping Seng Chua. Dynamic Mechanical Analysis Studies of the Interphase. *Polymer Composites*, 8(5), 1987.
- Keith Slater. *Human comfort*. Springfield, Ill., USA: CC Thomas, 1985.
- S. A. Suarez, R. F. Gibson, C. T. Sun, and S. K. Chaturvedi. The influence of fiber length and fiber orientation on damping and stiffness of polymer composite materials. *Experimental Mechanics*, 26(2):175–184, 1986. ISSN 00144851. doi: 10.1007/BF02320012.
- L. Torres. Estudo e Fabrico de Estrutura de Veículo Automóvel em compósito. Master’s thesis, Faculdade de Engenharia da Universidade do Porto, 2016.
- Erol Türkeş and Süleyman Neşeli. A simple approach to analyze process damping in chatter vibration. *International Journal of Advanced Manufacturing Technology*, 70(5-8):775–786, 2014. ISSN 02683768. doi: 10.1007/s00170-013-5307-0.
- Joachim Vanwalleghem. Study of the damping and vibration behaviour of flax-carbon composite bicycle racing frames. Master’s thesis, Ghent University, 2009. URL http://lib.ugent.be/fulltxt/RUG01/001/418/457/RUG01-001418457_2010_0001_AC.pdf.
- Joachim Vanwalleghem, Frederik Mortier, Ives De Baere, Mia Loccufier, and Wim Van Paepegem. Design of an instrumented bicycle for the evaluation of bicycle dynamics and its relation with the cyclist’s comfort. *Procedia Engineering*, 34:485–490, 2012. ISSN 18777058. doi: 10.1016/j.proeng.2012.04.083. URL <http://dx.doi.org/10.1016/j.proeng.2012.04.083>.
- F. Vilhena. Development of FSW for composite materials. Master’s thesis, Faculdade de Engenharia da Universidade do Porto, 2020.

Libo Yan, Nawawi Chouw, and Krishnan Jayaraman. Flax fibre and its composites - A review. *Composites Part B: Engineering*, 56:296–317, 2014. ISSN 13598368. doi: 10.1016/j.compositesb.2013.08.014. URL <http://dx.doi.org/10.1016/j.compositesb.2013.08.014>.

Experimental Equipment List

Impact Hammer

Trademark / Model	DYTRAN Instruments/ 5800SL
Sensitivity	23,7 mV/N

Accelerometer 27A11

Trademark / Model	ENDEVCO / 27A11
Sensitivity	0.9859 mV/ms ⁻²
Mass	1 g

Portable Data Acquisition System


Trademark / Model	Brüel&Kjær / 2827-002
Sensitivity	-

Dial Indicator

Trademark / Model	Mitutoyo / No. 2046F
Resolution	0,01 mm

Appendix B

XC110 210g 2x2 Twill 3k Prepreg Carbon Fibre - Catalog



XC110 | OUT-OF-AUTOCCLAVE COMPONENT PREPREG

SUITABLE MOULDS/TOOLING

Moulds/tools should be epoxy-based composite moulds, epoxy tooling board or metal. In all cases, moulds must be temperature stable to a minimum of 85°C but ideally to 120°C.

Although it is possible to use Vinylester tools (such as Uni-Mould™) they are not recommended due to the increased possibility of surface imperfections (pin holes) which can occur when XPREG® XC110 is cured in the presence of vinylester.

Polyurethane tooling board should never be used with any XPREG® prepreg due to the cure inhibition of polyurethane on epoxy on elevated temperature.

Fully Compatible

- Carbon or glass fibre prepreg moulds (e.g. XPREG® XT135)
- Epoxy tooling board (e.g. EP700 with S120 Board Sealer)
- High temp epoxy hand-layup moulds (e.g. EG160 / EMP160)
- Aluminium / stainless steel moulds
- Toughened glass (for flat sheet/panels)

NOT Recommended

- Vinylester composite moulds (e.g. Uni-Mould™)

NOT Compatible

- Polyester composite moulds
- Polyurethane model/tooling board

For detailed information on mould suitability and preparation, see the *XC110 Processing Handbook*.

STANDARD REINFORCEMENTS

XPREG® XC110 is available off-the-shelf using standard reinforcements of 210g 3k and 416g 6k carbon fibre.

SKU	Fibre	Weight (gsm)	Weave	Width (mm)
XC110-C331T2-210(1250)	Pyrofil TR30S High Strength Carbon 3k	210	2x2	1250
XC110-1232T2-416(1250)	Pyrofil TR50S High Strength Carbon 6k	416	2x2	1250

A range of alternative reinforcements including multiaxial and unidirectional can be produced on request, subject to MOQ.

TECHNICAL SPECIFICATION

GENERAL PROPERTIES

Cure temperature range	85°C to 120°C
Maximum service temperature	115°C (after post cure)
Out-life (at 20°C)	30 days
Freezer-life (at -18 °C)	12 months
VOC content	Very low (solvent free)

CURED MECHANICAL PROPERTIES

Tests performed on XC110-C331T2-210(1250) laminate cured out-of-autoclave

Property	Test Standard	Units	Result
Compressive strength	BS EN ISO 14126 : 1999	MPa	483
Tensile strength	BS EN ISO 527-4 : 1997	MPa	521
Tensile modulus	BS EN ISO 527-4 : 1997	GPa	55.1
Flexural strength	BS EN ISO 14125 : 1998	MPa	777
Flexural modulus	BS EN ISO 14125 : 1998	GPa	46.7
Interlaminar shear strength	BS EN 2563 : 1997	MPa	64.7
Tg Onset (DMA)	ASTM 1-0003 Issue 3	°C	121
Tg Peak (DMA)	ASTM 1-0003 Issue 3	°C	135

STORAGE & HANDLING

When not in use, XPREG® prepregs should be kept frozen at -18°C (0°F) in sealed plastic packaging. When ready to use, the material should be removed from the freezer and allowed to thaw fully to room temperature before being removed from the packaging.

Remaining material should be re-sealed before returning to the freezer to avoid the risk of moisture uptake.

PROCESSING GUIDE

XPREG® XC110 is supported by a highly detailed processing guide to help users achieve the best results from this advanced material.

The guide includes information on recommended laminating and vacuum bagging procedures, tooling and mould preparation, process specific cure cycles, working with core materials and adhesive films, and troubleshooting tips.

SAFETY INFORMATION

This material contains uncured epoxy resin which can cause allergic reactions with skin contact. Repeated and prolonged skin contact much be avoided.

Please refer to the product safety data sheet before working with this material.

XC110 Out-of-Autoclave Component Prepreg - Technical Datasheet - 17/08/2017

Distributed by **Easy Composites Ltd** | Tel +44 (0)1782 454499 | www.easycarboncomposites.co.uk | sales@easycarboncomposites.co.uk

Page 2 of 3

Figure B.1: Page 2 of the catalog of the woven carbon fiber used